A Robust Control Approach to Understanding Nonlinear Mechanisms in Shear Flow Turbulence

Thesis by

Dennice Gayme

In Partial Fulfillment of the Requirements

for the Degree of

Doctor of Philosophy
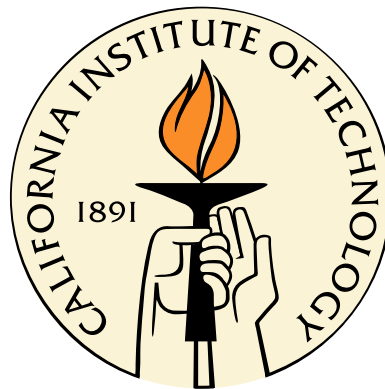
California Institute of Technology

Pasadena, California

2010

(Defended May 19, 2010)

To Christophe and my family,

especially Grace, Matthew and Colin,

with love.

Acknowledgments

When I think about this long journey, an old expression about it taking a village comes to mind. There are so many people who contributed to getting me to this point, and I cannot adequately express my deep appreciation for your help, support and encouragement.

First, and foremost I would like to thank my advisor John Doyle, for allowing me the freedom to explore many interesting ideas. I am grateful for his guidance, support and encouragement both personal and professional. I am also deeply grateful to my co-advisor Beverley McKeon, for her endless patience in explaining basic fluids concepts as well as for reeling me in when I wanted to explore too many directions at once. She taught me many important lessons about research and professional development. I also feel fortunate to have interacted with the other members of my committee: Bassam Bamieh who introduced me to distributed systems theory and who was a constant source of inspirational ideas and discussions; and Jerrold Marsden who provided me with the dynamical systems point of view and gave me the opportunity to develop my skills as an instructor. Finally, I want to thank Antonis Papachristodoulou, who has been a mentor to me throughout my time at Caltech. I have learned many things from him, and benefited greatly through working with him, both at Caltech and at Oxford, where he was a wonderful host.

I would also like to acknowledge my undergraduate advisor. Dr. Mo Elbestawi has had a profound influence on my academic life. He introduced me to both scholarly research and control theory. He continues to be source of inspiration, encouragement and good advice.

This research would not be possible without the generous support of The James Irvine Foundation Graduate Fellowship and a grant from The Boeing Corporation. The P.E.O. Scholar Award helped to finance travel to Oxford as well as other research related activities. A special thanks to H. Kawamura and T. Tsukahara for providing us with their DNS data.

CDS is a unique environment for learning and scholarship. I am deeply appreciative to have had the pleasure of interacting with all of the CDS students, faculty and staff.

Abstract

A robust control framework is used to investigate a streamwise constant projection of the Navier Stokes equations for plane Couette flow. Study of this streamwise constant model is motivated by both numerical and experimental observations that suggest the prevalence and importance of streamwise and quasi-streamwise elongated structures. Small-amplitude Gaussian noise forcing is applied to a two-dimensional, three-velocity component $(2D/3C)$ model to describe its response in the presence of disturbances, uncertainty and modeling errors. A comparison of the results with Direct Numerical Simulation (DNS) data demonstrates that the simulations capture salient features of fully developed turbulence. In particular, the change in mean velocity profile from the nominal laminar to the characteristic "S" shaped turbulent profile. The application of Taylor's hypothesis shows that the model can also reproduce downstream information in the form of large-scale coherence resembling numerically and experimentally observed flow features. The $2D/3C$ model is able to generate "turbulent-like" behavior under small-amplitude stochastic noise. The laminar flow solution is globally stable, therefore transition to turbulence in this model is likely a consequence of the laminar flow solution's lack of robustness in the presence of disturbances and uncertainty. In fact, large disturbance amplification is common in both this model and the linearized Navier Stokes equations.

Periodic spanwise/wall-normal $(z–y)$ plane stream functions are used as input to develop a forced $2D/3C$ streamwise velocity equation. The resulting steady-state solution is qualitatively similar to a fully turbulent spatial field of DNS data. Both numerical methods and a perturbation analysis confirm that the momentum transfer that produces a "turbulent-like" mean profile requires a nonlinear streamwise velocity equation.

A system theoretic approach is used to study the amplification mechanisms that develop through the $2D/3C$ nonlinear coupling in the streamwise velocity equation. The spanwise/wall-normal plane forcing required to produce each stream function is computed

and used to define an induced norm from this forcing input to the streamwise velocity. This input-output response is used to determine the energy optimal spanwise wavelength (i.e., the preferential spacing) over a range of Reynolds numbers and forcing amplitudes. This analysis serves to augment the well-developed linear theory through the addition of the nonlinear coupling in the streamwise velocity equation.

Contents

List of Figures

List of Tables

Chapter 1

Introduction

Turbulence is often referred to as one of the last unsolved problems in physics. Analytically, its study is limited because turbulence is mathematically governed by a system of nonlinear partial differential equations (the Navier Stokes equations) for which even basic properties like existence and uniqueness of solutions are not understood. Turbulence operates at a variety of scales and the separation between the largest and smallest scales increases polynomially with Reynolds number (R). Therefore, from a computational perspective, it is impossible to carry out simulations that resolve all of these scales of dynamic activity at very high Reynolds numbers. Experiments have their own set of challenges, particularly in the development of sensors and techniques that can simultaneously capture all of the behavior at different flow scales while not interfering with the flow.

Traditional hydrodynamic stability theory has enabled significant progress toward understanding transition to turbulence [16]. It has been successfully used to predict transition for many well-studied flows such as Rayleigh-Bénard convection and Taylor-Couette flow. However, this process of linearizing the Navier Stokes (NS) equations about the laminar flow solution and identifying the so-called critical Reynolds number at which instabilities appear, fails to accurately predict transition for wall-bounded shear flows. For example, plane Couette flow is linearly stable for all Reynolds numbers [78], however transition has been experimentally observed at Reynolds numbers as low as 350 [86]. Channel flows have exponentially growing linear modes starting at $R = 5772$. However, experiments also show significantly different behavior than this linear prediction with transition commonly occurring at Reynolds numbers of 1000 [12, 70].

Non-normality of the underlying linear operator is the basis for some of the prevalent theories regarding hydrodynamic stability theory's failure to accurately predict wall-bounded

shear flow transition. A normal operator $\mathcal{A}$ is one for which $\mathcal{A}\mathcal{A}^* = \mathcal{A}^*\mathcal{A}$. In finite-dimensional systems, normality is equivalent to a matrix possessing a full set of orthogonal eigenvectors. A non-normal operator is one that is not normal. Stable linear systems governed by non-normal linear operators can experience substantial transient growth before they eventually decay [79, 89, 90]. This type of behavior is also supported by results from linear algebra which indicate that small perturbations of such linear operators can push the operator from stable to unstable [89, 90]. Certain growth scenarios, the so-called transient growth theories, are based on studies that consider growth of the *worst case* initial flow disturbances [10, 33, 73]. The resulting large temporal growth exceeds the size of the initial disturbance by large factors, e.g., $O(R^2)$, even in the linearly stable Reynolds number regimes. Another approach to the problem considers input-output *energy amplification*, as apposed to *growth*, by regarding background noise or some sort of forcing as "input" and the resulting sustained energy as "output" [2, 25, 26]. This type of input-output amplification is also related to non-normality of the underlying operator and gives rise to similar large disturbance amplification, e.g., $O(R^{\frac{3}{2}})$ or $O(R^3)$ depending on the nature of the input. Growth of the linear operator is of particular importance because the nonlinear terms are thought to be energy conserving. Therefore, it is believed that only the linearized Navier Stokes (LNS) can provide the necessary growth to allow the system to transition to turbulence.

The control theoretic interpretation of both the transient growth and input-output energy amplification theories is that transition is not a stability problem but rather a robustness issue. Large growth/amplification leads to correspondingly large system norms or "high gains". The small gain theorem provides a relationship between a system's potential size (in a normed sense) and the amount of permissible "uncertainty", such as modeling errors or external disturbances, before a system is unable to maintain stability. Essentially the bound on the uncertainty is inversely proportional to the maximal response of the system. The LNS equations are known to be so-called "high gain operators". As the upper bound on their amplification increases, the amount of uncertainty at the frequencies corresponding to the maximal response must be reduced. As the Reynolds number rises the "uncertainty set" must continually be made smaller in order to compensate for the increasingly large disturbance amplification. In practice, reducing the system uncertainty to "almost zero" is impossible. In these terms, the main driving factor in the transition to turbulence can be viewed as a robustness issue in which the stability of the NS equations is not robust

to disturbances (uncertain parameters). The observation that transition can be delayed in experiments with extremely carefully controlled conditions (and equivalently numerical accuracy in simulations) comes directly from the fact that the magnitude of the system norm (and the associated transient energy growth and/or input-output amplification) increases with Reynolds number.

Certain preferentially aligned inputs/initial conditions produce significantly greater increases in energy. In particular, initial conditions representing disturbances in the form of streamwise vortices produce the largest energy growth. The resulting flow is dominated by streaks of streamwise velocity [10, 24]. In fact, streamwise constant features emerge as the LNS' dominant mode shapes for wall-bounded shear flows. They produce the largest input-output response under various perturbations about both laminar [2, 25, 44] and turbulent velocity [13] profiles. This streamwise alignment of structures is also consistent with the features that are most amplified under random disturbances of the LNS (with a laminar base flow) [25, 27]. Bamieh and Dahleh derived an explicit relationship showing that streamwise constant disturbances produce energy growth on the order of R^3 whereas streamwise varying disturbances grow as a function of $R^{\frac{3}{2}}$ [2]. In addition, studies of supercritical plane Poiseuille flow indicate that the spectral energy of streamwise constant structures continues to be larger than that of the linearly unstable modes well into the supercritical Reynolds number regime [33, 45]. In fact, it took 20 years and very carefully controlled conditions to experimentally recreate the theoretically predicted Tollmien-Schlichting waves associated with the Poiseuille flow unstable modes [81].

Dominance of streamwise infinitely elongated modes is supported by a growing body of work that points to characterization of wall-bounded shear flow in terms of dynamically significant coherent structures. The most common of these features being those with streamwise and quasi-streamwise alignment. Large, channel-spanning, streamwise coherent "roll cells" were first observed in Direct Numerical Simulations (DNS) of Couette flow [57]. High Reynolds number boundary layer and pipe flow experiments identified similar phenomena in other flow configurations [28, 32, 39, 48, 53, 65]. These very large-scale motions consist of long but narrow coherent regions of low and high momentum, relative to the mean. They are of great interest because they carry a substantial portion of the flow energy [39, 40, 65]. Furthermore, in turbulent boundary layers they appear to modulate the activity near the wall, see for example [40, 61]. These large structures, in addition to the streamwise struc-

tures involved in the well-studied near-wall cycle [35, 43, 93, 95], underscore the importance of streamwise coherence in the flow field.

In fact, the ubiquity of streamwise elongated structures is one of the two most well accepted facts about fully developed turbulence in wall-bounded shear flows. The other is that the average turbulent velocity profile is repeatable (i.e., turbulence is an ergodic process). Linear models enable one to generate flows that consist of the same types of streamwise elongated structures observed in simulations and experiments. The linearized equations cannot, however, capture the change in the mean velocity profile as the flow transitions from laminar to turbulent. Only a nonlinear model can generate the characteristic "S" shape of the so-called "blunted" turbulent velocity profile. The question then becomes, which nonlinearities are needed to reproduce this important flow feature. The previously discussed experimental and analytical studies affirming the importance of streamwise homogenous motions suggest that the nonlinearities that persist in a streamwise constant model of the flow may be a natural place to begin investigation.

In this dissertation, we employ a streamwise constant projection of the NS equations, which results in a so-called two-dimensional, three (velocity) component, henceforth $2D/3C$, model for plane Couette flow. This nonlinear model is an attempt to merge the benefits of studying a physics-based model, such as NS, with the analytical tractability of a simplified model, such as the LNS. We describe how tools from robust control theory [15, 17] can be combined with this streamwise constant model to provide a framework for understanding some of the salient features of fully developed turbulence in plane Couette flow. The $2D/3C$ nominal model includes nonlinear effects that are stressed by some researchers, while maintaining the mathematical properties associated with linear disturbance amplification. The robust control ideas provide the mathematical framework necessary to incorporate the effects of the unmodeled dynamics, modeling errors and external disturbances to the flow field.

1.1   Objectives, Outline and Contributions

The main objective of this dissertation is to determine the extent to which a $2D/3C$ model in a robust control setting can be used to describe the features of a fully developed turbulent plane Couette flow. We pursue this objective through both simulations and an analytical

study examining the effect of $2D/3C$ nonlinear coupling on the development of a "turbulent-like" velocity profile. The simulation is used as a "proof of concept" to determine whether or not the $2D/3C$ model can produce a flow field consistent with fully developed turbulence. Reproduction of a "turbulent-like" mean velocity profile is of most interest. The goals of the steady-state analysis are: (1) to isolate the mathematical mechanisms that are involved in generating an appropriately shaped turbulent velocity profile; (2) to identify the dominant spanwise mode shapes involved in the blunting; and (3) to illustrate the analytical tractability of the model.

The organization and main contributions of this dissertation are described in the following chapter summaries. Chapter 2 provides the control theoretic preliminaries. It begins with the background material necessary for the analysis of spatially distributed systems. Wherever possible we provide analogies to dynamical systems governed by ordinary differential equations. The relevant stability notions for both linear and nonlinear systems are introduced. The chapter concludes with an exposition on the use of robust control ideas as a means of characterizing uncertain systems.

Chapter 3 begins with a description of the flow problem setting. It concludes by connecting the robust control notions described in Chapter 2 to analytical studies of wall-bounded shear flows as well as to commonly observed features of these flow configurations.

Chapters 4–6 are devoted to the simulation and analysis of streamwise constant plane Couette flow. Chapter 4 details the motivation for studying such a model. Then we step through the derivation of the $2D/3C$ model. A proof of global stability of the $2D/3C$ laminar flow solution and a description of the model's input-output energy response are provided. The potential for disturbance amplification in this model is tied to the robust control notions of Chapter 2.

In Chapter 5 we describe simulations of the $2D/3C$ model under low amplitude Gaussian noise forcing of the cross-stream components. The results of the simulations demonstrate that our robust control modeling paradigm allows us to capture important flow features. In particular, we make the following observations.

- A stochastically forced $2D/3C$ model reproduces the appropriate turbulent mean velocity and Reynolds number trends.

- The inclusion of the nonlinear terms in the $2D/3C$ streamwise velocity equation cap-

tures the momentum redistribution involved in creating the characteristic "blunted" appearance of the turbulent velocity profile. The other equations can be linearized.

- Very little forcing is necessary to develop features consistent with the turbulent velocity profile. This indicates that the globally stable laminar profile is not robust to small disturbances.

- Finally, the important linear input-output amplification mechanisms that have been connected to both subcritical transition to and maintenance of turbulence are not lost in a streamwise constant approximation of the flow field.

Then, we take a further step toward understanding the full impact of streamwise constant features on the flow by examining the extent to which the application of Taylor's hypothesis at the centerline can be used to reconstruct information about the upstream velocity field. We determine that this $2D/3C$ model can be convected at the centerline to yield streamwise information associated with the large-scale streaky structures that have been observed in experiments and numerical studies.

In Chapter 6 we take a closer look at the streamwise velocity component of the $2D/3C$ model. We first evaluate the extent to which $2D/3C$ nonlinear coupling (in the streamwise velocity equation) can create features consistent with the mean characteristics of fully developed turbulence. We use a steady-state periodic spanwise/wall-normal (z–y) plane stream function to create an idealized model of the streamwise and quasi-streamwise very large-scale motions. We use these stream functions as an input to generate forced solutions of the time-independent streamwise velocity equation. These solutions are shown to have the same qualitative features as both a spatial field of DNS data and the results of the full stochastic simulation of Chapter 5. We are able to generate a "turbulent-like" flow field using simple inputs consistent with experimental observations of cross-stream flow features. These results provide evidence that the nonlinear terms in the $2D/3C$ streamwise velocity equation are responsible for the momentum transfer associated with the change in profile from the nominal laminar to the turbulent state.

We then use a system theoretic approach to study the amplification mechanisms that develop through this nonlinear coupling. We compute the spanwise/wall-normal (z–y) plane forcing required to produce the stream functions described above. An L_2–to–L_2 induced norm from the forcing input to the streamwise velocity is used to define an amplification

factor. This factor is used to determine the wave number that produces the maximum amplification over a range of Reynolds numbers and forcing amplitudes. These maxima correspond to an estimate of the spanwise preferential spacing. The optimal spanwise wavelengths we computed in this manner match prior studies at low Reynolds numbers. Reynolds number scaling of the amplification factor was also consistent with previous parallel flow investigations.

Finally, we attempt to isolate the nonlinear mechanisms involved in creating the characteristic "S" shape of the turbulent velocity profile. In Section 6.5 we use a perturbation technique (weakly nonlinear analysis) to analytically investigate new nominal streamwise velocity solutions $U(y, z)$. These fixed points arise through assuming that the flow has cross-stream velocities $V(y, z)$ and $W(y, z)$ which correspond to streamwise elongated large-scale streaks and vortices. Then, we evaluate the role of each of the nonlinear terms in contributing to the shape of the solution. The results of this study underscore the important function that the $2D/3C$ nonlinear coupling (in the streamwise velocity equation) serves in facilitating the momentum transfer required to generate the turbulent mean velocity. The fact that we were able to obtain closed form solutions for certain stream function inputs encourages the pursuit of further analytical study of this model.

The concluding chapter of the dissertation discusses these results in light of the robust control modeling paradigm. Directions for future study are also outlined.

Chapter 2

Control Theoretic Preliminaries

This chapter introduces the control theoretic concepts used in the study of spatially distributed systems. For ease of exposition we begin by describing the relevant ideas in a linear setting and then introduce only the most relevant analogous concepts for nonlinear systems. The chapter concludes with a discussion of input and model uncertainty in dynamical systems.

Spatially distributed systems can be mathematically modeled using partial differential equations. In general, analysis of a partial differential equation (PDE) is a difficult problem because, unlike their finite-dimensional counterparts (ordinary differential equations), there is no systematic procedure for determining their solution. Most nonlinear PDEs are solved on a case-by-case basis. It is sometimes possible, however to make analogies between the well-developed theory of ordinary differential equations (ODEs) and particular spatially distributed systems, although this generally requires some additional technical assumptions. In the sequel, we present the relevant concepts.

2.1   Notation

Given a function $\varphi(x_1, x_2, \ldots, x_n, t)$ a *partial differential equation* (PDE) relates any of the partial derivatives of φ to one another along with any of the variables, $x_1, x_2, \ldots, x_n$ and φ. Each $\varphi(x_1, x_2, \ldots, x_n, t)$ is an n-dimensional field that evolves in time. A one-dimensional example of the evolution of such a system $(\varphi(x_1, t))$ is depicted in Figure 2.1. We sometimes denote $\varphi(x_1, x_2, \ldots, x_n, t)$ by $\varphi(\mathbf{x}, t)$.

The basic notation is as follows:

We denote the entire state of the spatial distribution at time t as $\boldsymbol{\Phi}(t)$. So $(\boldsymbol{\Phi}(t))(\mathbf{x}) :=$
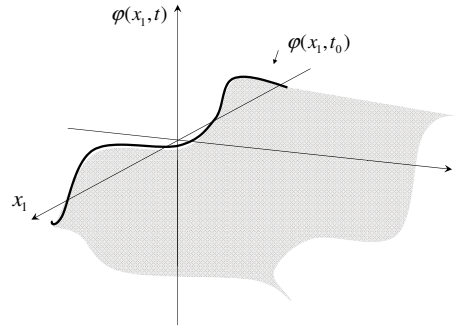
Figure 2.1: Schematic of a one-dimensional spatially distributed dynamical system. The initial condition ($\varphi(x, t_0)$ at $t = t_0$) is a one-dimensional spatially distributed field in x.

$\varphi(\mathbf{x}, t)$ is the value of the spatially distributed function at the spatial location $\mathbf{x}$ at time t.

A Hilbert[1] (Banach[2]) space is denoted $\mathbb{H}$ ($\mathbb{B}$). For the shear flow problem that is the topic of this dissertation the analysis assumes that we are operating on a Hilbert space $\mathbb{H}$.

Definition 2.1.1. *L_2 denotes the Hilbert space of Lebesgue integral functions $g : \mathbb{R} \to \mathbb{R}$ such that*

$$\|\mathbf{g}(t)\|_{L_2} := \left\{ \int_{-\infty}^{\infty} |\mathbf{g}|^2 dt \right\}^{\frac{1}{2}} < \infty.$$

This is the typical Hilbert space employed for plane Couette and channel flow.

The set of bounded linear operators on a Hilbert space $\mathbb{H}$ (Banach space $\mathbb{B}$) is denoted $\mathcal{L}(\mathbb{H})$ ($\mathcal{L}(\mathbb{B})$).

The set of closed linear operators on a Hilbert space $\mathbb{H}$ (Banach space $\mathbb{B}$) is denoted $\mathcal{C}(\mathbb{H})$ ($\mathcal{C}(\mathbb{B})$).

For and operator $\mathcal{A}$, $\mathcal{D}(\mathcal{A})$ denotes its domain.

---

[1]A Hilbert space is a complete inner product space
[2]A Banach space is a complete normed space

2.2 Spatially Distributed Linear Systems

The state space representation, *evolution form*, of a spatially distributed linear system with state $\varphi(\mathbf{x}, t)$, input $\mathbf{d}(\mathbf{x}, t)$ and output $\phi(\mathbf{x}, t)$ is

$$\frac{\partial \varphi(\mathbf{x}, t)}{\partial t} = \mathcal{A}\varphi(\mathbf{x}, t) + \mathcal{B}\mathbf{d}(\mathbf{x}, t) \tag{2.1a}$$

$$\phi(\mathbf{x}, t) = \mathcal{C}\varphi(\mathbf{x}, t), \tag{2.1b}$$

where $\mathbf{x}$ is the set of spatial variables (the vector field), $\varphi(\mathbf{x}, t)$, $\phi(\mathbf{x}, t)$, and $\mathbf{d}(\mathbf{x}, t)$ are elements of a Banach space $\mathbb{B}$ or Hilbert space $\mathbb{H}$ and $\mathcal{A}$, $\mathcal{B}$ and $\mathcal{C}$ are operators (generally partial differential or integral). The domain, $\mathcal{D}(\mathcal{A})$, of the operator $\mathcal{A}$ and the spatial boundary conditions must be explicitly included in the definition of $\mathcal{A}$. For example, if $\varphi \in L_2(0, 1)$, then conditions on $\varphi(0, t)$ and $\varphi(1, t)$ comprise the boundary conditions and $\mathcal{D}(\mathcal{A}) = \{\varphi \in L_2(0, 1) | \varphi(0, t) = b_1, \ \varphi(1, t) = b_2)\}$.

We cast spatially distributed system equations in the form of (2.1) in order to illustrate the parallels between them and their finite-dimensional counterparts (ordinary differential equations). There are certainly cases for which this is not possible. For example, the concept of continuity does not have a unified definition across all infinite-dimensional systems. In the next section we describe a class of infinite-dimensional systems that allow us to develop results on stability, growth and asymptotic behavior that are similar to those from the finite-dimensional theory.

2.2.1 Continuity and Regularity of Solutions: Semigroup Theory

The mathematical theory that defines the existence, uniqueness and regularity of solutions of infinite-dimensional systems is semigroup theory [1, 4, 11]. In this section we describe some basic elements of this theory that allows us to define the so-called C_0 semigroup, which is the most natural abstraction of a linear dynamical system.

Consider a simplified expression of the evolution equation (2.1a) with no input (i.e., $\mathbf{d} \equiv 0$):

$$\frac{d}{dt}\mathbf{\Psi}(t) = \mathcal{A}\mathbf{\Psi}(t). \tag{2.2}$$

As in (2.1a), the specification of system (2.2) requires careful specification of the properties of the operator $\mathcal{A}$. The domain of $\mathcal{A}$ must be explicitly defined such that the trajectories

of the state remain in the appropriate Hilbert space $\mathbb{H}$, (e.g., $\mathcal{A} : \mathcal{D}(\mathcal{A}) \to \mathbb{H}$). Its definition must also include specification of all necessary boundary conditions.

Definition 2.2.1. *The system (2.2) is well-posed if the state of the system is unique and it varies continuously with the initial state. This implies for any $t \geq 0$, there exists a solution $\mathbf{\Psi}(t)$ for each initial condition $\mathbf{\Psi}(0)$.*

Let the mapping $T(t)$ be defined as

$$T(t) : \mathbf{\Psi}(0) \to \mathbf{\Psi}(t).$$

Then, solutions of (2.2) can be completely specified by a family of linear operators $\{T(t)\}_{t \geq 0}$ such that

$$\mathbf{\Psi}(t) = T(t)\mathbf{\Psi}(0). \tag{2.3}$$

$\{T(t)\}_{t \geq 0}$ *is referred to as the **evolution semigroup**. This is analogous to the "fundamental solution" or "state transition" matrix in finite-dimensional systems.*

Definition 2.2.2. *Suppose that $\mathbb{H}$ is a Hilbert space and that $z_0 \in \mathbb{H}$ is the state of the dynamical system at $t = 0$. A **strongly continuous semigroup** (C_0-semigroup) is a parameterized family $\{T(t)\}_{t \geq 0} \in \mathcal{L}(\mathbb{H})$, i.e., for each t, the bounded linear operator $T(t) : \mathbb{H} \to \mathbb{H}$, has the following properties:*

$$T(t + s) = T(t)T(s) \text{ for } t, s \geq 0; \tag{2.4a}$$

$$T(0) = I; \tag{2.4b}$$

$$\|T(t)z_0 - z_0\| \to 0 \text{ as } t \to 0^+ \text{ for any } z_0 \in \mathbb{H}. \tag{2.4c}$$

Equations (2.4a) and (2.4b) define a general semigroup. Equation (2.4c) is particular to C_0 semigroups. It enforces the additional condition that state trajectories form a continuous curve in $\mathbb{H}$.

Definition 2.2.3. *[60] Let $\{T(t)\}_{t \geq 0}$ be a semigroup on the Hilbert space $\mathbb{H}$. The operator $\mathcal{A}$ defined through*

$$\mathcal{A}v := \lim_{t \to 0} \frac{T(t)v - v}{t}$$

*for $v \in \mathcal{D}(\mathcal{A}) := \left\{ v \in \mathbb{H}; \lim_{t \to 0} \frac{T(t)v - v}{t} \text{ exists} \right\}$ is called the **infinitesimal generator** (or **generator**) of the semigroup $\{T(t)\}_{t \geq 0}$.*

If $\mathcal{A}$ is the generator of a semigroup $\{T(t)\}_{t\geq 0}$, we denote

$$e^{\mathcal{A}t} := T(t).$$

In this case the solution of (2.2) reduces to the familiar form from the ordinary differential equation (ODE) theory (i.e., $\mathbf{\Psi}(t) := e^{\mathcal{A}t}\mathbf{\Psi}(0)$).

Definition 2.2.4. *Let $\mathcal{A}$ in (2.2) generate a C_0 semigroup ($e^{\mathcal{A}t}$) on the Hilbert space $\mathbb{H}$, then the resolvent set of $\mathcal{A} : \mathcal{D}(\mathcal{A}) \to \mathbb{H}$ is*

$$\rho(\mathcal{A}) = \{z \in \mathbb{C} : (zI - \mathcal{A})^{-1} \text{ exists, is bounded, and defined on a dense set in } \mathbb{H}\}.$$

$\mathcal{R}_z(\mathcal{A}) := (zI - \mathcal{A})^{-1}$ *is referred to as the resolvent of $\mathcal{A}$ at $z \in \mathbb{C}$ [55]. The points in the set $z \in \rho(\mathcal{A})$ are called the **regular values**. The **spectrum** of $\mathcal{A}$, denoted $\sigma(\mathcal{A})$, is the complement (in $\mathbb{C}$) of the resolvent set.*

2.2.2 Linear Stability Notions

In this section, various stability notions for (2.2) are discussed.

Definition 2.2.5. *[1, 11] Consider a C_0-semigroup $\{T(t)\}_{t\geq 0}$ of bounded linear operators on a Hilbert space $\mathbb{H}$ (i.e., the space $\mathcal{L}(\mathbb{H})$). The semigroup $\{T(t)\}_{t\geq 0}$ is called*

    1. ***weakly asymptotically stable** if*

$$\forall u, v \in \mathbb{H}, \quad \langle u, T(t)v \rangle \to 0 \ \text{as } t \to 0;$$

    2. ***strongly asymptotically stable** if*

$$\forall v \in \mathbb{H}, \quad T(t)v \to 0 \ \text{as } t \to 0;$$

    3. ***uniformly asymptotically stable** if*

$$\|T(t)\| \to 0 \ \text{as } t \to \infty;$$

4. ***strongly exponentially stable*** *if*

$$\text{for each } v \in \mathbb{H}, \ \exists\, M, \ \alpha > 0 \text{ such that } \forall t \geq 0, \ \|T(t)v\| \leq Me^{-\alpha t} \text{ and;}$$

5. ***exponentially stable*** *if*

$$\exists\, M, \ \alpha > 0 \text{ such that } \|T(t)\| \leq Me^{-\alpha t} \ \forall t \geq 0.$$

Remarks 2.2.1.

1. *In items 4 and 5 of Definition 2.2.5 α is called the* decay rate *and the supremum over all possible values of α is the* stability margin *of $T(t)$.*

2. *In the finite-dimensional case all of the stability notions enumerated in Definition 2.2.5 are equivalent.*

In the finite-dimensional case, exponential stability is directly related to the spectrum $\sigma(A)$ of the matrix A. In particular, stability requires $\sup_{\lambda \in \sigma(A)} Re(\lambda) < 0$. This is not true for general C_0-semigroups $\{T(t)\}_{t \geq 0}$, but an analogous statement can be made by enforcing a special condition on $\sigma(\mathcal{A})$.

Definition 2.2.6. *The growth rate, ω_0, of $T(t)$ is defined as*

$$\omega_0 := \inf_{t>0} \frac{\log \|T(t)\|}{t}. \tag{2.5}$$

This implies that $\forall t \geq 0$ there exists $M > 0$ such that $\|T(t)\| \leq Me^{(\omega_0 + \varepsilon)t}$ for any $\varepsilon > 0$.

If

$$\omega_0 = \sup\{Re\lambda | \lambda \in \sigma(\mathcal{A})\} \tag{2.6}$$

*then we say that $T(t)$ satisfies **the spectrum determined growth condition**.*

Remarks 2.2.2. *The spectrum determined growth condition has been shown to be satisfied when*

- $\mathcal{A}$ *is bounded,*

- $\{T(t)\}_{t \geq 0}$ *is an analytic semigroup, or*

- $\{T(t)\}_{t\geq 0}$ is compact for some $t_1 > 0$ (i.e., for all $t \geq t_1$).

Theorem 2.2.1. *A C_0-semigroup $\{T(t)\}_{t\geq 0}$ of bounded linear operators on a Hilbert space $\mathbb{H}$ is exponentially stable if the following two statements hold.*

   i. The spectrum of $\mathcal{A}$ lies in the open left-half plane.

   ii. $T(t)$ satisfies the spectrum determined growth condition.

Some other useful characterizations of exponential stability are provided in Lemma 2.2.1 and Theorem 2.2.2.

Lemma 2.2.1. *[11] The C_0 evolution semigroup $\{T(t)\}_{t\geq 0}$ on the Hilbert space $\mathbb{H}$ is exponentially stable if and only if for every $z \in \mathbb{H}$ there exists a positive constant $\gamma_z < \infty$ such that*

$$\int_0^\infty \|T(t)z\|^2 dt \leq \gamma_z.$$

Theorem 2.2.2. *Suppose that $\mathcal{A}$ is a densely defined generator of the C_0-semigroup $\{T(t)\}_{t\geq 0}$ on the Hilbert space $\mathbb{H}$. Then, $\{T(t)\}_{t\geq 0}$ is exponentially stable if and only if there exists a positive bounded operator $\mathcal{P}$ such that*

$$\forall \boldsymbol{\Psi} \in \mathcal{D}(\mathcal{A}), \quad \langle \mathcal{A}\boldsymbol{\Psi}, \mathcal{P}\boldsymbol{\Psi} \rangle + \langle \mathcal{P}\boldsymbol{\Psi}, \mathcal{A}\boldsymbol{\Psi} \rangle = -\langle \boldsymbol{\Psi}, \boldsymbol{\Psi} \rangle. \tag{2.7}$$

We refer to (2.7) as an operator Lyapunov equation. In an abuse of notation, we often write the operator Lyapunov equation (2.7) as

$$\mathcal{A}\mathcal{P} + \mathcal{P}\mathcal{A} = -\mathcal{I},$$

where $\mathcal{I} : \mathbb{H} \to \mathbb{H}$ is the identity operator.

2.2.3 Nonlinear Semigroups and Their Stability

We now introduce a general semigroup suitable for the study of nonlinear dynamical systems [4, 84]. Then, we briefly describe the nonlinear stability notions [34, 37, 60] that will be used in the analysis of Chapter 4.

A general nonlinear system with state $\gamma(\mathbf{x}, t)$ (and no input) is given by

$$\frac{\partial \gamma}{\partial t} = F(\gamma(\mathbf{x}, t)), \quad \gamma(\mathbf{x}, 0) = \gamma_0, \tag{2.8}$$

where γ is an element of a complete metric space $\mathbb{M}$, generally a Hilbert space. As in (2.2) we write $\mathbf{\Gamma}(t)$ to abstract the spatio-temporal state $\gamma(\mathbf{x}, t)$, and assume that (2.8) is well-posed.

Definition 2.2.7. *A **nonlinear dynamical system (semigroup)** on a complete metric space $\mathbb{M}$ is a family of mappings $\{S(t) : \mathbb{M} \to \mathbb{M}\}_{t \geq 0}$ with the semigroup properties (2.4a) and (2.4b), i.e;*

$$S(t + s) = S(s)S(t) \quad \forall t, s \geq 0, \tag{2.9a}$$

$$S(0) = I \ \ on \ \mathbb{M}. \tag{2.9b}$$

If ξ is the state of (2.8) at time s then $S(t)\xi$ is the state of the system at time $t + s$, and

$$\mathbf{\Gamma}(t) = S(t)\mathbf{\Gamma}(0),$$

$$\mathbf{\Gamma}(t + s) = S(t)\mathbf{\Gamma}(s) = S(s)\mathbf{\Gamma}(t), \quad s, t \geq 0.$$

Finally we assume that $S(t) : \mathbb{M} \to \mathbb{M}$, $\forall t \geq 0$ is a continuous nonlinear operator such that, for each $\xi \in \mathbb{M}$, $\quad t \mapsto S(t)\xi$ is continuous.

We say that $\{S(t)\}_{t \geq 0}$ defines the evolution semigroup of the dynamical systems (2.8) and the set $\gamma(\xi) = \{S(t)\xi, t \geq 0\}$ is the positive-semi orbit through ξ.

Definition 2.2.8. *Suppose $\{S(t)\}_{t \geq 0}$ is a semigroup on a Banach space $\mathbb{B}$. A set $Z \subset \mathbb{H}$ is a functional invariant set for $\{S(t)\}_{t \geq 0}$ if*

$$S(t)Z = Z.$$

This set may be a fixed point (i.e., $Z = \{\xi_*\}$, for some $\xi_* \in \mathbb{H}$). A time-periodic orbit may also be represented by this Z when it exists, i.e., for some $\gamma_0 \in \mathbb{H}$ and $T > 0$, $S(T)\gamma_0 = \gamma_0$ then $S(T)\gamma_0$ exists for all $t \in \mathbb{R}$ and $Z = \{S(T)\gamma_0, t \in \mathbb{R}\}$ is invariant.

Stability is defined in the same way as for an ODE system:

Definition 2.2.9. *[37] An orbit $\gamma(\xi)$ is **stable** if for any $\varepsilon > 0$ there exists $\delta(\varepsilon) > 0$ such*

that for $\alpha \in \mathbb{M}$ and all $t > 0$, $dist(S(t)\alpha, S(t)\xi) < \varepsilon$, whenever $dist(\alpha, \xi) < \delta(\varepsilon)$. An orbit is unstable if it is not stable.

An orbit is uniformly stable if in addition to the above there exists a neighborhood $\mathcal{B}_r\{\alpha \in \mathbb{M} : dist(\alpha, \xi) < r\}$ such that

$$dist(S(t)\alpha, S(t)\xi) \rightarrow 0 \ as \ t \rightarrow 0$$

uniformly for $\alpha \in \mathcal{B}_r$.

Definition 2.2.10. *[60] Let F be a closed subset of $\mathbb{M}$ and $\mathcal{V} : F \rightarrow \mathbb{R}$ be a (continuous) function, where the time derivative of $\mathcal{V}$ is defined*

$$\dot{\mathcal{V}} := \lim_{t \rightarrow 0^+} \frac{1}{t}\{\mathcal{V}(S(t)\xi) - \mathcal{V}(\xi)\} \leq 0 \tag{2.10}$$

for all $\xi \in F$, where it is allowable that $\dot{\mathcal{V}} = -\infty$. Then $\mathcal{V}$ is called a (continuous) Lyapunov function on F.

In Theorem 2.2.3 we assume the induced topology of some Banach space $\mathbb{B} \subset \mathbb{M}$, so for the metric "$dist$" associated with $\mathbb{M}$ there is an induced norm $\|\xi - \alpha\| = dist(\xi, \alpha)$, for ξ, $\alpha \in \mathbb{B}$.

Theorem 2.2.3. *Let $\{S(t)\}_{t \geq 0}$ be a dynamical system on a complete metric space $\mathbb{M}$ and let $\xi^* = 0$ be an equilibrium point in $\mathbb{M}$.*

Suppose that $\mathcal{V}$ is a Lyapunov function on $\mathbb{M}$ such that $\mathcal{V}(0) = 0$ and $\mathcal{V}(\xi) \geq c(\|\xi\|)$ for $\xi \in \mathbb{M}$, with $\|\xi\| = dist(\xi, 0)$, where c is a continuously increasing function, with $c(0) = 0$ and $c(r) > 0$ for all $r > 0$. Then, 0 is stable.

If in addition $\dot{\mathcal{V}}(\xi) \leq -c_1(\|\xi\|)$, for $\xi \in \mathbb{M}$, with $\|\xi\| = dist(\xi, 0)$, where $c_1(\cdot)$ is also a continuous, increasing and positive function with $c_1(0) = 0$. Then, 0 is uniformly asymptotically stable.

2.3 Spatial Invariance

In this section, we consider systems of the form (2.1) that are spatially invariant in at least one direction. We develop all of the tools for linear systems but many of these ideas extend to nonlinear systems. For our purposes, spatial invariance is the spatial analog of

time invariance, i.e., the dynamics are translation invariant in some spatial coordinate [3]. General spatial invariance can be defined whenever the spatial coordinates can be acted on by a *group* of symmetries where the dynamics commute with the group action [1].

The spatial Fourier transform is

$$\hat{\varphi}(\kappa, t) := \int_{\mathbb{R}^n} \varphi(\mathbf{x}, t) e^{-j\kappa \mathbf{x}} \, d\mathbf{x}, \tag{2.11}$$

where $d\mathbf{x} = dx_1 \, dx_2 \ldots dx_n$ is the differential volume element in $\mathbb{R}^n$ and $\kappa = [\kappa_1, \ldots, \kappa_n] \in \mathbb{R}^n$ is the vector of spatial frequencies (wave numbers). Applying this transformation to (2.1) reduces the problem to a parameterized family of ODEs, where each κ_i includes all values in $\mathbb{R}$.

Applying the Fourier transform to the spatially invariant coordinates of (2.1) results in the following parameterized family of evolution equations:

$$\frac{\partial \hat{\varphi}(\kappa, t)}{\partial t}(y) = \hat{A}_\kappa \hat{\varphi}(\kappa, t)(y) + \hat{B}_\kappa \hat{\mathbf{d}}(\kappa, t)(y) \tag{2.12a}$$

$$\hat{\phi}(\kappa, t) = \hat{C}_\kappa \hat{\varphi}(\kappa, t)(y), \tag{2.12b}$$

where the Fourier transform has been applied in the spatially invariant directions (i.e., $\kappa = [\kappa_1, \ldots, \kappa_r]$ is the vector of frequencies corresponding to the spatially invariant coordinates $\eta = [x_1, \ldots, x_r]$) and $y = [y_1, \ldots, y_{n-r}]$ represents the remaining spatial coordinate(s) (i.e., the set $\mathbb{P} \subseteq \mathbb{H}$ that is not translation invariant). The operators $\hat{A}_k$, $\hat{B}_k$ and $\hat{C}_k$ are the Fourier symbols of $\mathcal{A}$, $\mathcal{B}$ and $\mathcal{C}$ respectively.

This transformation makes a number of systems properties easier to compute. The following theorem [1] makes this statement precise in terms of exponential stability.

Theorem 2.3.1. *The following two statements about a spatially invariant system of the form (2.2) and the parameterized set of state space models (2.12) are equivalent.*

1. *The system $(\mathcal{A})$ is exponentially stable.*

2. *(a) For each $\kappa \in \mathbb{R}$, $\hat{A}_\kappa$ is stable, and*

   (b) the solution of the family of Lyapunov equations

$$\hat{A}_\kappa^* P_\kappa + P_\kappa \hat{A}_\kappa = -\mathcal{I}$$

is bounded, i.e.,

$$\sup_{\kappa \in \mathbb{R}} \| P_\kappa \| < \infty.$$

A similar result holds for the spectrum $\sigma(\mathcal{A})$ of $\mathcal{A}$ in (2.1), specifically

$$\sigma(\mathcal{A}) = \overline{\bigcup_{\kappa \in \mathbb{R}} \sigma\left(\hat{A}_\kappa\right)},$$

where $\sigma\left(\hat{A}_\kappa\right)$ is the spectrum of $\hat{A}_\kappa$.

The relationship between the spectra of $\mathcal{A}$ and the corresponding parameterized family of operators $\hat{A}_\kappa$ as well as Theorem 2.3.1 imply that one can determine the stability properties of (2.1) by studying the more computationally amenable transformed equations (2.12). This idea of using the parameterized family of (possibly ODE) models to determine properties of the full spatially distributed system (2.1) is exploited in the tools discussed in Section 2.4. Applying a Fourier transform to simplify a spatially distributed system model is a common technique employed in linear analysis of wall-bounded shear flows, discussed in Chapter 3.

2.4 Input-Output Models

2.4.1 Spatio-Temporal Impulse and Frequency Responses

Given a stable generator $\mathcal{A}$, a general input-output model of (2.1) is given by

$$\phi(\mathbf{x}, t) = \int_{-\infty}^{\infty} \int_{\mathbb{R}^n} H(\mathbf{x}, \zeta, t - \tau) \mathbf{d}(\zeta, \tau) \, d\zeta \, d\tau, \tag{2.13}$$

where $H(\mathbf{x}, \zeta, t - \tau)$, is the Green's function (or operator kernel) of the PDE. For a system that is spatially invariant in coordinates $\eta = [x_1, \ldots, x_r]$ this can be simplified such that

$$y(\mathbf{x}, t) = \int_{-\infty}^{\infty} \int_{\mathbb{R}^{n-r}} \int_{\mathbb{R}^r} H(y, \chi, \eta - \xi, t - \tau) \mathbf{d}(\chi, \xi, \tau) \, d\xi \, d\chi \, d\tau, \tag{2.14}$$

where $y = [y_1, \ldots, y_{n-r}]$ are the coordinates that are not spatially invariant. *The spatio-temporal impulse response* is the kernel (which by abuse of notation we also refer to as $H(y, \eta, t)$) when the input in (2.14) is an impulsive delta function $\delta(y - y_0, \eta, t)$. The term spatio-temporal impulse response is used because $H(y, \eta, t)$ is the solution of the PDE in (2.12) with input $\delta(y - y_0, \eta, t)$.

In practice, it is often easier to compute $H(y, \eta, t)$ in the frequency domain. The combined spatial and temporal Fourier transform of an input $\mathbf{d}(\eta, y, t)$ to the system (2.1) is given by

$$\hat{\mathbf{d}}(y, \kappa, \omega) = \int_{-\infty}^{\infty} \int_{\mathbb{G}} e^{-j\omega t} e^{-j\kappa \cdot \eta} \mathbf{d}(y, \eta, t) \, d\mathbf{x} \, dt, \tag{2.15}$$

where $\mathbb{G}$ is the spatial group, $\kappa \in \mathbb{G}$ and $\kappa \cdot \eta := \kappa^T \eta$. Since convolution in (2.14) corresponds to multiplication in the frequency domain, it follows that

$$\hat{y}(y, \kappa, \omega) = \hat{H}(y, \kappa, \omega) \hat{\mathbf{d}}(y, \kappa, \omega). \tag{2.16}$$

This $\hat{H}(y, \kappa, \omega)$, which corresponds to the Fourier transform of $H(y, \eta, t)$, is called the spatio-temporal frequency response of (2.1). It can easily be computed by taking the temporal Fourier transform of (2.12) and solving for $\hat{\varphi}(y, \kappa, \omega)$. Then

$$\hat{H}(y, \kappa, \omega) = \hat{C}_\kappa \left(j\omega \mathcal{I} - \hat{A}_k \right)^{-1} \hat{B}_\kappa. \tag{2.17}$$

Equation (2.17) is also referred to as the transfer function of (2.1). Clearly one can use this spatio-temporal frequency response to compute the spatio-temporal impulse response $H(y, \eta, t)$, so both quantities contain the same information about the system's dynamics. However, one particular form may provide more insight into a specific system property. In the sequel, we often write the respective spatio-temporal impulse and frequency responses as $H(\kappa, \omega)(y)$ and $H(\eta, t)(y)$ to indicate that they are in fact operator valued functions of the spatial variables y. In Section 2.4.3 we illustrate the use of both time and frequency domain responses in the computation of system gains. In general, we focus on the frequency response because it is computationally easier. In order to facilitate the gain discussion, we introduce the concept of singular values in the next section.

2.4.2 Singular Values

In this section we discuss the *singular value (Schmidt) decomposition* of the spatio-temporal frequency response. The discussion is limited to stable systems because the maximal amplification for an unstable system is always infinite and thus does not provide meaningful information. The *singular value (Schmidt) decomposition* of the spatio-temporal frequency

response is

$$\left[\hat{H}(\kappa,\omega)\mathbf{d}(\kappa,\omega)\right](y) = \sum_{m=1}^{\infty} \sigma_m(\kappa,\omega) \langle \mathbf{d}, \mathbf{p}_m \rangle \mathbf{q}_m, \tag{2.18}$$

where $\{\sigma_m \geq 0\}_{m \in \mathbb{N}}$ are the singular values of $H(\kappa,\omega)(y)$ arranged in descending order, and $\{\mathbf{p}_m\}_{m \in \mathbb{N}}$ and $\{\mathbf{q}_m\}_{m \in \mathbb{N}}$ are respectively its right and left singular functions. This arrangement means that $\sigma_1(\kappa,\omega)$ determines the worst case amplification for any input.

The singular functions can be interpreted as follows. Let $\mathbf{d} := \mathbf{p}_n$ for some $n \in \mathbb{N}$ in (2.18). Then,

$$[H(\kappa,\omega)\mathbf{p}_n(\kappa,\omega)](y) = \sigma_n(\kappa,\omega)\mathbf{q}_n(y,\kappa,\omega).$$

So, an input in the $\mathbf{p}_n(\kappa,\omega,y)$ direction produces an output in the $\mathbf{q}_n(\kappa,\omega,y)$ direction, while $\sigma_n(\kappa,\omega)$ represents the input-output gain for a system excited in the $\mathbf{p}_n$ direction. In light of this relationship, $\mathbf{p}_n(\kappa,\omega,y)$ and $\mathbf{q}_n(\kappa,\omega,y)$ are often referred to as the respective input and output directions. For the maximal singular value, $\sigma_1(\kappa,\omega)$, the corresponding $\mathbf{p}_1(y,\kappa,\omega)$ represents the most amplified input direction. The corresponding $\mathbf{q}_1(y,\kappa,\omega)$ is then the output direction that has the most potential for input growth, i.e., the pair $(\mathbf{p}_1, \mathbf{q}_1)$ correspond to the worst case input and output directions at a given (κ,ω). The notion of worst case amplification is discussed in the following system in terms of the $\mathcal{H}_\infty$ norm.

2.4.3   System Norms and Input-Output Gain

It is not always easy to understand the dynamics of (2.1) by looking at the spatio-temporal responses derived in Section 2.4.1. In general (2.17) may be an operator valued function in both space and time. In this section we introduce the $\mathcal{H}_2$ and $\mathcal{H}_\infty$ system norms [99] as a way of quantifying behavior of (2.1) in terms of its input-output amplification or "gain". We begin by defining the norms and then discuss how to compute the $\mathcal{H}_2$ norm.

Definition 2.4.1. *The $\mathcal{H}_\infty$ norm of $H(y,\kappa,\omega)$ is*

$$[\|H\|_\infty](\kappa) := \sup_\omega \sigma_{max}(H(\kappa,\omega)), \tag{2.19}$$

i.e., the maximum singular value (σ_{max}) of H over all frequencies.

Definition 2.4.2. *The $\mathcal{H}_2$ norm is defined as*

$$[\|H\|_2^2](\kappa) := \frac{1}{2\pi} \int_{-\infty}^{\infty} \|H(\kappa,\omega)\|_{HS}^2 \, d\omega = \int_{-\infty}^{\infty} \|H(\kappa,t)\|_{HS}^2 \, dt, \tag{2.20}$$

where

$$\|H\|_{HS}^2 := trace(HH^*) = \sum_{n=1}^{\infty} \sigma_n^2(H).$$

In the finite-dimensional (matrix) case, this is the Frobenius norm.

Definition 2.4.3. *In the time domain the induced L_2–to–L_2 norm of $H(\kappa,t)$ is*

$$\|H\|_{L_2} := \sup_{\|\mathbf{d}(\kappa,t)\|_2 \leq 1} \frac{\|\phi(\kappa,t)\|_2}{\|\mathbf{d}(\kappa,t)\|_2}. \tag{2.21}$$

In the transformed space (frequency domain) this is equivalent to the $\mathcal{H}_\infty$ norm.

Both the $\mathcal{H}_2$ and $\mathcal{H}_\infty$ norms are finite for stable systems. These norms are of interest because they have a convenient physical interpretation. As discussed in Section 2.4.2, the $\mathcal{H}_\infty$ norm can be interpreted as the worst case amplification of a deterministic input [46]. In a stochastic setting, the $\mathcal{H}_2$ norm represents the amplification of for inputs $\mathbf{d}(y,\eta,t)$ that are stochastic in y and t and harmonic in η. In the fluid mechanics literature, this is commonly referred to as the *ensemble average energy density* of the statistical steady-state [25].

The $\mathcal{H}_2$ norm of (2.1) can be computed from the solutions of the operator Lyapunov equations for the controllability and observability gramians, $\mathfrak{X}$ and $\mathcal{Y}$ [99],

$$A_\kappa \mathfrak{X}_\kappa + \mathfrak{X}_\kappa A_\kappa^* = B_\kappa B_\kappa^* \tag{2.22a}$$

$$A_\kappa \mathcal{Y}_\kappa + \mathcal{Y}_\kappa A_\kappa^* = C_\kappa C_\kappa^* \tag{2.22b}$$

where A_κ^*, B_κ and C_κ^* are respectively the adjoint of A_κ, B_κ and C_κ from (2.12). Then,

$$[\|H\|_{HS}^2](\kappa) := trace(\mathfrak{X}_\kappa C_\kappa^* C_\kappa) = trace(\mathcal{Y}_\kappa B_\kappa B_\kappa^*)$$

2.5 Robustness

In this section we discuss robust stability and performance. We relate robust stability to the input-output properties of the system using the small gain theorem. We then intro-
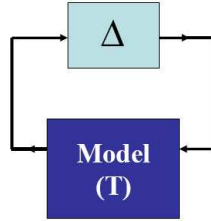
Figure 2.2: The standard robust control block diagram for a model subject to uncertainty. Generally a norm bound on Δ specifies the amount of uncertainty that a model can have before a desired property is lost (e.g., if the model is stable for $\|\Delta\| \leq 1$, this implies robust stability).

duce the concepts of non-normal linear operators and pseudospectra. Finally we relate the pseudospectra of an operator to robust stability of that operator.

In order to study a physical system, usually one constructs a simple model that describes the evolution of the system as accurately as possible. Models are by definition idealized versions of the actual physical process and as such there is some uncertainty inherent in any model. These uncertainties may represent physical phenomena that are difficult to characterize, errors in model parameters, conditions that can be characterized by adding additional complexity to the model, or any other unmodeled conditions that tend to be present in experiments or numerical simulations.

In order to understand how an uncertainty or modeling errors affect the behavior of a model one can study its "robustness" [15, 17]. A model/property is said to be robust to a particular uncertainty/disturbance if it maintains that property in the face of the uncertainty/disturbance. Two common characteristics that are often discussed in terms of robustness are stability and performance. One generally illustrates this idea through the diagram shown in Figure 2.2 [15] where the block labeled model may represent, for example, the transfer function H and the Δ represents any uncertainties/disturbances that influence the system.

2.5.1 Robust Input-Output Response

In order to make the concept of robust stability concrete it is useful to study system (2.2) in terms of its resolvent. If a system satisfies the spectrum determined growth condition

(2.6), then exponential stability of the generator of $\mathcal{A}$ is equivalent to

$$\sup_{Re(z)>0} \|\mathcal{R}_z(\mathcal{A})\| < \infty.$$

For a system of the form (2.1a) with $\mathcal{C} = \mathcal{I}$, $\mathcal{B} = \mathcal{I}$ and input $\mathbf{d}$, the resolvent can be determined as the transfer function from $\mathbf{d}$ to the state φ, (we denote this by T to distinguish it from the more general case where $\mathcal{B}, \mathcal{C} \neq \mathcal{I}$). Then in the transformed space the maximum modulus principle [15] means that exponential stability reduces to a condition on the infinity norm $\mathcal{H}_\infty$ of this special case of the system (2.1a).

Using this idea, the problem of robust stability can be precisely formulated as stability of a system

$$\frac{\partial \varphi}{\partial t} = (\mathcal{A} + \Delta) \varphi \tag{2.23}$$

with Δ accounting for model uncertainty. With this simple "unstructured uncertainty", the small gain theorem provides a test for robust stability.

Theorem 2.5.1. *[15] If both Δ and T are stable, then the feedback interconnection shown in Figure 2.2 is stable if $\|\Delta T\|_{L_2} < 1$.*

The small gain theorem provides a characterization of robust stability in terms of the system gain, which is closely related to the resolvent of the operator $\mathcal{A}$ in (2.1). In the next section we take a closer look at $\mathcal{R}_z(\mathcal{A})$ for particular regular values $z \in \mathbb{C}$, the so-called pseudospectra. We use this idea to illustrate a slightly different version of the small gain theorem.

2.5.2 Relationship with Pseudospectra

The pseudospectra of $\mathcal{A}$ are closely related to its spectra. Recall that the spectrum of $\mathcal{A}$ consists of the points $\lambda \in \mathbb{C}$ such that $(\lambda I - \mathcal{A})^{-1}$ does not exist (as a bounded linear operator). This definition can also be interpreted to mean that perturbations with a frequency λ can have unbounded amplification [88, 90], which can roughly be stated as $\|(\lambda I - A)^{-1}\| = \infty$.

In many applications one might also be interested in regular points z that produce large or small resolvent.

Definition 2.5.1. *[89] Let $\mathcal{A}$ be a closed linear operator on a Banach space $\mathbb{B}$ and $\varepsilon > 0$ be arbitrary. The ε-**pseudospectrum** of $\mathcal{A}$ is the set $\lambda_\varepsilon \in \mathbb{C}$ defined by either of the following*
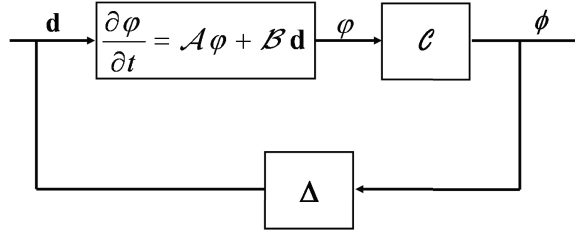
Figure 2.3: Block diagram of the system (2.25) that can be represented by (2.1) for application of a small gain theorem.

equivalent conditions:

$$\Lambda_\varepsilon(\mathcal{A}) = \left\{ \lambda_\varepsilon \in \mathbb{C} : \left\| (\lambda_\varepsilon \mathcal{I} - \mathcal{A})^{-1} \right\| \geq \varepsilon^{-1} \right\}, \tag{2.24a}$$

$$\lambda_\varepsilon \in \sigma(\mathcal{A}) \ \text{or} \ \| (\lambda_\varepsilon \mathcal{I} - \mathcal{A}) u \| < \varepsilon \ \text{for some} \ u \in \mathcal{D}(\mathcal{A}) \ \text{with} \ \|u\| = 1, \tag{2.24b}$$

where $\mathcal{D}(\mathcal{A})$ is the domain of $\mathcal{A}$. If $\| (\lambda_\varepsilon \mathcal{I} - \mathcal{A}) u \| < \varepsilon$ as in (2.24b), then λ_ε is an ε- ***pseudoeigenvalue*** *of $\mathcal{A}$ and u is the corresponding ε-* ***pseudoeigenfunction (or pseudomode)****.*

Clearly $\Lambda_\varepsilon(\mathcal{A})$ is a superset of the eigenvalues of A, which can be thought of as the 0-pseudospectra $\Lambda_0(\mathcal{A})$. An equivalent definition of the ε-pseudospectra that is also useful in the context of robust control theory is the following.

Definition 2.5.2. *[89] The ε-pseudospectrum of $\mathcal{A}$ is the set of complex numbers $\lambda_\varepsilon \in \mathbb{C}$ such that $\lambda_\varepsilon \in \lambda(\mathcal{A} + E)$ for some bounded linear operator E with $\|E\| < \varepsilon$ and $\varepsilon > 0$. i.e., the eigenvalues of some nearby linear system defined by $\mathcal{A} + E$.*

This is directly related to determining the stability of (2.23) and Theorem 2.5.1 with E representing Δ. In order to emphasize the connection we look at a more structured dynamical system:

$$\frac{\partial \varphi}{\partial t} = (\mathcal{A} + \mathcal{B}\Delta\mathcal{C}) \varphi. \tag{2.25}$$

This can be represented by the system (2.1) if we define $\mathbf{d} := \Delta\phi$ as shown in Figure 2.3.

Then robust stability of (2.25) means that

$$\sup_{Re(z)} \| \mathcal{R}_z(\mathcal{A} + \mathcal{B}\Delta\mathcal{C}) \| < \infty, \quad \forall \|\Delta\|_{L_2} \leq \varepsilon, \tag{2.26}$$

where $\mathcal{R}_z(\mathcal{A} + \mathcal{B}\Delta\mathcal{C})$ is the resolvent of $\mathcal{A} + \mathcal{B}\Delta\mathcal{C}$. The expression (2.26) precisely defines $E = \Delta$ in Definition 2.5.2 when $\mathcal{B} = \mathcal{C} = \mathcal{I}$. The small gain theorem for the system (2.25) can then be stated.

Theorem 2.5.2. *The system in Figure 2.3 is robustly stable for all* $\|\Delta\|_{L_2}$ *if and only if its spatio-temporal response,* H *satisfies* $\|H\|_{L_2} < \frac{1}{\varepsilon}$.

Equation 2.24a in Definition 2.24 shows that the points that do not satisfy Theorem 2.5.2 (i.e., $\mu \in \mathbb{C}$ such that $\|H\|_{L_2} \geq \frac{1}{\varepsilon}$) are essentially the ones inside the ε-pseudospectrum of $\mathcal{A}$.

The final point that we discuss in this chapter has to do with the pseudospectra of non-normal linear operators.

Definition 2.5.3. *A linear operator* $\mathcal{A}$ *on a Hilbert space* $\mathbb{H}$ *is said to be* ***normal*** *if* $\mathcal{A}\mathcal{A}^* = \mathcal{A}^*\mathcal{A}$, *where* $\mathcal{A}^*$ *is an appropriately defined adjoint.*

A ***non-normal*** *linear operator is one that is not normal.*

For the finite-dimensional matrix case, normality is equivalent to the matrix A having a complete set of orthogonal eigenvectors.

The ε-pseudospectra of a normal linear operator are the points $z \in \mathbb{C}$ that measure a distance (in the appropriate metric) of at most ε from the spectra. This is not the case for a non-normal operator, in which case the ε-pseudospectra may be much further away. This means that systems governed by non-normal operators can experience large amplification (*pseudoresonance*) at frequencies that are far from the resonant points (i.e., the spectra) [88].

The properties of non-normal linear operators are of interest because wall-bounded shear flows are generally governed by such operators. In the next chapter, we will discuss these flows in more detail and specifically discuss how non-normality is related to important flow phenomena.

2.6 Summary

In this chapter, we described some of the control theoretic concepts that are relevant to the study of wall-bounded shear flows. In particular:

- We discussed the evolution form of the dynamical equation for these systems and how it relates to concepts from finite-dimensional dynamical systems theory.

- We introduced linear and nonlinear stability notions for infinite-dimensional systems. We discussed how these notions collapse in the finite-dimensional case and provided a technical condition required to use the spectra to define stability. We described how Lyapunov functions could be used to show both linear and nonlinear stability.

- We discussed the use of the Fourier Transform to reduce a spatially invariant infinite-dimensional system into a parameterized finite-dimensional system.

- We introduced the spatio-temporal impulse and frequency response of these systems. We related the $\mathcal{H}_2$ norm of the response to disturbance energy of the system. This concept will be discussed in more detail in Chapter 3 when we review previous work on the linearized flow equations.

- We introduced the concept of forced equations to represent the addition of disturbances to a nominal model. We then used the input-output metrics to develop a means of analyzing these systems in the face of these disturbances.

- Finally, we introduced the small gain theorem as a method of guaranteeing that a system is robust to disturbances.

We focused on the theory of linear spatially distributed systems because most of the analytic results on these flows stem from the linearized flow equations. We only presented the nonlinear concepts that are necessary to analyze the streamwise constant model for plane Couette flow discussed in chapters 4–6.

In the next chapter we provide an overview of shear flows. We begin by introducing the flow equations. Then we discuss previous work analyzing these equations in terms of the control theoretic concepts from this chapter.

Chapter 3

Wall-Bounded Shear Flows

In this chapter we describe wall-bounded shear flow related preliminaries. We confine our discussion to incompressible flow between infinite parallel plates, particularly flows that have one-dimensional nominal velocities. First, we present the continuity constrained Navier Stokes (NS) equations and use them to derive the linear evolution equations. Then, we provide an overview of previous research on the linearized equations that is relevant to the results in this thesis. Finally, we use these results to describe the system properties in terms of the control theoretic notions introduced in Chapter 2.

3.1 The Navier Stokes Equations

Given a coordinate system (x, y, z) representing the streamwise, wall-normal and spanwise directions respectively, the NS equations and continuity constraint governing incompressible flow of a viscous Newtonian fluid are

$$\frac{\partial \mathbf{u}}{\partial t} = -\mathbf{u} \cdot \nabla \mathbf{u} - \nabla p + \frac{1}{R} \Delta \mathbf{u}$$

$$\nabla \cdot \mathbf{u} = 0. \tag{3.1}$$

Here $\mathbf{u} = (u, v, w)$ represents the velocity vector and $p(x, y, z)$ is the pressure. The symbol ∇ represents the gradient and $\Delta = \nabla \cdot \nabla = \nabla^2$ is the Laplacian. Equation (3.1) depends on the parameter $R := \frac{UL}{\nu}$, the Reynolds number associated with the characteristic length scale L and velocity scale U as well as the kinematic viscosity of the fluid (ν).

The dynamics of the fluctuations around a nominal flow condition $(\mathbf{U}, P)$ are determined
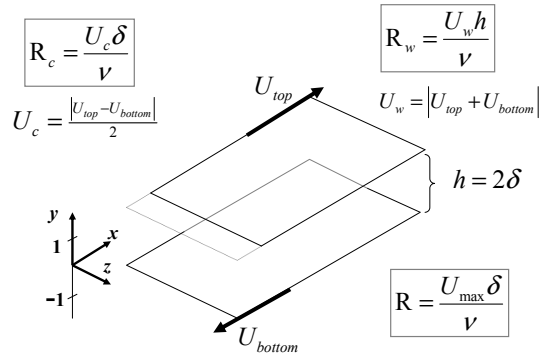
Figure 3.1: Flow between parallel plates. Generally the plates are assumed to be infinite in x and z and vary between $[-1, 1]$ in y. Couette flow is driven by relative motion between the plates (U_{top} versus U_{bottom}) and the Reynolds number is generally $R_c := \frac{U_c \delta}{\nu}$ based on the channel half-height δ and the centerline velocity (half the velocity differential). $R_w := \frac{U_w h}{\nu}$ based on the full channel height h and the full velocity differential is also used for Couette flow. Poiseuille (channel) flow is pressure driven flow between stationary plates, i.e., it corresponds to $U_{top} = U_{bottom} = 0$ in the figure. The Reynolds number for channel flow $R := \frac{U_{max} \delta}{\nu}$ is based on the maximum (centerline) velocity and the half-height of the channel.

by expressing the fields as a sum of nominal (base) and fluctuating terms, i.e.,

$$\mathbf{u} = \mathbf{u}' + \mathbf{U} \quad \text{and} \quad p = p' + P.$$

Filling these expressions into (3.1) yields

$$\frac{\partial \mathbf{u}'}{\partial t} = -\mathbf{u}' \cdot \nabla \mathbf{u}' - \mathbf{u}' \cdot \nabla \mathbf{U} - \nabla \mathbf{p}' + \frac{1}{\mathbf{R}} \boldsymbol{\Delta} \mathbf{u}' - \mathbf{U} \cdot \nabla \mathbf{u}'$$
$$- \left\{ \frac{\partial \mathbf{U}}{\partial t} + \mathbf{U} \cdot \nabla \mathbf{U} + \nabla P - \frac{1}{R} \Delta \mathbf{U} \right\}, \tag{3.2}$$
$$\nabla \cdot \mathbf{u}' = -\nabla \cdot \mathbf{U}.$$

If the nominal state satisfies the constrained NS equations (3.1), then both the term in the curly brackets and $\nabla \cdot \mathbf{U}$ are zero. The remaining terms define the nonlinear evolution equations for the perturbations $\mathbf{u}'$.

3.2   The Linearized Equations

In this section we develop the evolution form of the linearized Navier Stokes (LNS) equations. We linearize the perturbation equations (3.2) about a laminar (nominal) flow. We assume a one-dimensional laminar flow made up of a streamwise component varying along the wall-normal direction, i.e., $\mathbf{U} = (U(y), 0, 0)$. This is consistent with both plane Couette and plane Poiseuille (channel) flow. The typical geometry for these two common examples of flow between parallel plates is pictured in Figure 3.1 along with the common characteristic length and velocity scales used for defining their Reynolds numbers. The typical coordinate frame is a wall-normal extent of $y \in [-1, 1]$ with the plates infinitely extending in the streamwise (x) and spanwise (z) directions. Plane Couette flow is driven by relative motion between the upper and lower plates. It has a linear laminar profile. The Reynolds number for Couette flow is generally $R_c := \frac{U_c \delta}{\nu}$ based on the channel half-height δ and the centerline velocity (or half of the velocity differential, i.e., $\frac{|U_{top} - U_{bottom}|}{2}$). However, $R_w := \frac{U_w h}{\nu}$ based on the full channel height h and the full velocity differential is also used for Couette flow. We will primarily use R_w in describing the results in Chapter 5 and sections 6.1–6.4. Plane Poiseuille flow, which is also known as plane channel flow, has fixed walls, is pressure driven and has a parabolic laminar profile. The typical Reynolds number for channel flow $R := \frac{U_{max} \delta}{\nu}$ is based on the maximum (centerline) velocity and the half-height of the channel (δ).

The linearized equations for infinitesimal disturbances about the laminar profile described above are

$$\frac{\partial u'}{\partial t} = -U \frac{\partial u'}{\partial x} - v' \frac{dU}{dy} - \frac{\partial p}{\partial x} + \frac{1}{R} \Delta u' \tag{3.3a}$$

$$\frac{\partial v'}{\partial t} = -U \frac{\partial v'}{\partial x} - \frac{\partial p}{\partial y} + \frac{1}{R} \Delta v' \tag{3.3b}$$

$$\frac{\partial w'}{\partial t} = -U \frac{\partial w'}{\partial x} - \frac{\partial p}{\partial z} + \frac{1}{R} \Delta w', \tag{3.3c}$$

with

$$\frac{\partial u'}{\partial x} + \frac{\partial v'}{\partial y} + \frac{\partial w'}{\partial z} = 0. \tag{3.4}$$

If we take the divergence of (3.3) and then use the continuity equation (3.4) we obtain

the following condition on the pressure:

$$\Delta p = -2 \frac{dU}{dy} \frac{\partial v'}{\partial x}.$$

If we fill this into the wall-normal velocity evolution equation (3.3b) we obtain a pressure independent evolution equation for v. If we then apply the transformation

$$\begin{bmatrix} \frac{\partial}{\partial z} & 0 & -\frac{\partial}{\partial x} \end{bmatrix}$$

to (3.3) we end up with evolution equations in terms of the wall-normal velocity v and wall-normal vorticity $\omega_y = \frac{\partial w}{\partial x} - \frac{\partial u}{\partial z}$. These are

$$
\frac{\partial}{\partial t} \begin{bmatrix} v \\ \omega_y \end{bmatrix} = \begin{bmatrix} \Delta^{-1} \left(U_{yy} \frac{\partial}{\partial x} - U \frac{\partial}{\partial x} \Delta + \frac{1}{R} \Delta \Delta \right) & 0 \\ -U_y \frac{\partial}{\partial z} & \left(-U \frac{\partial}{\partial x} + \frac{1}{R} \Delta \right) \end{bmatrix} \begin{bmatrix} v \\ \omega_y \end{bmatrix}
$$
$$
= \begin{bmatrix} \mathcal{L} & 0 \\ \mathfrak{C} & \mathcal{S} \end{bmatrix} \begin{bmatrix} v \\ \omega_y \end{bmatrix},
$$
(3.5)

where $U_y = \frac{dU}{dy}$, and again $\Delta = \frac{\partial^2}{\partial x^2} + \frac{\partial^2}{\partial y^2} + \frac{\partial^2}{\partial z^2}$ is the Laplacian operator. The symbols $\mathcal{L}$, $\mathcal{S}$ and $\mathfrak{C}$ are respectively the Orr-Sommerfeld, Squire, and coupling operators. This form of the LNS is generally referred to as the Orr-Sommerfeld Squire (OSS) equations [79].

3.3 Linear Analysis

3.3.1 Hydrodynamic Stability

The linearized equations, particularly (3.5), are often studied in the context of hydrodynamic stability theory, which addresses the response of a laminar flow to small perturbations [16, 79]. Unstable eigenvalues (i.e., elements of the point spectra with non-negative real parts) in the LNS are identified as a precursor to turbulence [16]. The spectrum is typically Reynolds number dependent and the Reynolds number where the operator becomes unstable is called the critical Reynolds number (R_{crit}).

Hydrodynamic stability theory has been very effective in determining R_{crit} for a number of different flow geometries (configurations). For example, in both Rayleigh-Bénard convec-

tion and Taylor Couette flow the experimentally observed critical Reynolds numbers tend to agree well with linear stability theory [16]. However, for other flows, in particular wall-bounded shear flows, linear stability theory has had much less success. Some flows, such as plane Couette flow and pipe (Hagen-Poiseuille) flow are predicted to be linearly stable for all Reynolds numbers [38, 78]. However, transition to turbulence typically occurs at Reynolds numbers on the order of 1000. In Couette flow, transition has been experimentally observed to occur at Reynolds numbers as low as 350 [86]. Similarly for channel flows (Poiseuille flow), the value predicted from linear analysis is $R_{crit} = 5772$ whereas experiments have observed transition at $R = 1000$ [12, 70].

This discrepancy in theory versus experiments has been studied for many years. The majority of researchers focus on one of the two aspects in traditional analysis: (1) the linearization about the laminar flow solution or (2) analysis of the resulting linear operator. The former group asserts that the failure in the analysis method is either due to the fact that the nonlinearities dominate [35, 94] or that the laminar solution is not the correct one to linearize about. One of the resulting research directions from this line of thinking is the search for additional solutions of the equations, i.e., some sort of "secondary instability" [6, 68]. Others argue the presence of a finite amplitude instability [54, 96] or chaotic behavior, e.g., [18, 20, 63].

The second group of theories focuses on linear amplification or transient growth of disturbances, see for example [10, 23, 72, 90]. Transition to turbulence is then accomplished through a so-called "bypass scenario", i.e., one that bypasses the traditional instability theory and happens in the absence of nonlinear affects. Large amplification in the LNS is related to the non-normality of the associated linear operator. Stable linear systems governed by non-normal linear operators can experience substantial transient growth before they eventually decay [79, 89, 90].

3.3.2 Disturbance Energy Growth

Studies [10, 27, 33, 73] have shown that wall-bounded shear flows do in fact amplify small perturbations by large factors even in the linearly stable Reynolds number regimes. This can be partially explained by the existence of points in ε-pseudospectra that are far from the eigenvalues of the non-normal OSS operator. To determine the extent to which a system is non-normal, Reddy et al. [73] introduced the concept of a condition number, κ, that

indicates how far the system is from having a full set of linearly independent eigenfunctions. The magnitude of κ is related to how sensitive the system is to perturbations. Using this concept they showed that the linear operators governing both Couette and Poiseuille flow are in a sense exponentially far from normal [90], (specifically, $\kappa \approx e^{\gamma R^{0.5}}$). Under this metric both plane Couette and Poiseuille flow are very far from normal and as such large transient growth is not unexpected.

Energy growth in the LNS is of primary importance because the linearized system is thought to capture the energy production of the full nonlinear system. It is widely believed that energy amplification is due to coupling terms that remain in linearized models [90]. Henningson and Reddy [36] showed that non-normality and linear mechanisms are necessary conditions for subcritical transition to turbulence. Kim and Lim [47] discovered that the associated linear coupling ($\mathfrak{C}$ in the OSS equations (3.5) linearized about the mean flow) is also required for the generation of the wall-layer streaks that are necessary to maintain turbulence in smooth wall-bounded shear flows. Streaks are the "strong spanwise variation in the downstream velocity" that Waleffe [93] associated with a "well-defined elongated region of spanwise alternating bands of low- and high-speed fluid" [97]. The metric for the maintenance of turbulence was the formation and continuing presence of the wall-layer streaks as well as near-wall streamwise vortices.

Early studies of disturbance amplification focused on finding initial conditions and disturbances to maximize the system's energy, $\mathcal{H}_2$ norm [10, 23, 24, 33, 72]. In these studies an orthogonal set of disturbances was ordered based on the potential for energy amplification over a fixed time interval. The conditions corresponding to the maximum were then called the optimal perturbations. These studies showed that with the optimally configured initial flow disturbance, transient energy growth can be on the order of R^2 in time scales on the order of R.

3.3.3 Input-Output Amplification

Energy growth of the forced LNS equations has also been considered [2, 25, 44, 45]. The evolution equations for the forced OSS model can then be written in the form (2.1), i.e.,

$$\frac{\partial \varphi(\mathbf{x}, t)}{\partial t} = \mathcal{A}\varphi(\mathbf{x}, t) + \mathcal{B}\mathbf{d}(\mathbf{x}, t)$$
$$\phi(\mathbf{x}, t) = \mathcal{C}\varphi(\mathbf{x}, t),$$

(3.6)

with state $\varphi = [v; \omega_y]$, $\mathcal{A} = \begin{bmatrix} \mathcal{L} & 0 \\ \mathfrak{C} & \mathcal{S} \end{bmatrix}$, forcing $\mathbf{d}(x, y, z, t)$ and $\mathcal{B}$ suitably defined to transform $\mathbf{d} = [d_x; d_y; d_z]$ into $\tilde{\mathbf{d}} = [d_v; d_{\omega_y}]$.

For parallel flows, $\mathcal{A}$, $\mathcal{B}$ and $\mathcal{C}$ are spatially invariant in the streamwise x and spanwise z directions. This allows one to Fourier transform the equations as described in Section 2.3 so that the transformed velocity and vorticity fields can be written

$$\hat{\varphi}(k_x, y, k_z, t) := \int_{-\infty}^{\infty} \int_{-\infty}^{\infty} \varphi(x, y, z, t) e^{-j(xk_x + zk_z)} \, dx \, dz,$$

where k_x and k_z are respectively the streamwise and the spanwise wave numbers. The transformed $\hat{\mathcal{A}}$, $\hat{\mathcal{B}}$ and $\hat{\mathcal{C}}$ operators are then one-dimensional PDEs (in y) parameterized by k_x and k_z. The corresponding transformed Orr-Sommerfeld, Squire and Coupling operators are

$$\hat{\mathcal{L}} = \hat{\Delta}^{-1} \left(-jk_x U \hat{\Delta} + jk_x \hat{U}_{yy} + \frac{1}{R} \hat{\Delta}\hat{\Delta} \right),$$

$$\hat{\mathcal{S}} = -jk_x \hat{U} + \frac{1}{R}\hat{\Delta},$$

$$\hat{\mathfrak{C}} = -jk_z \hat{U}_y,$$

where $K^2 = k_x^2 + k_z^2$ and $\Delta = \frac{d^2}{dy^2} - K^2$. The velocities $\hat{u}$ and $\hat{w}$ can be computed in terms of the wall-normal velocity $\hat{v}$ and vorticity ω_y:

$$\hat{u} = -\frac{1}{K^2} j \left(k_z \hat{\omega}_y - k_x \frac{d\hat{v}}{dy} \right)$$

$$\hat{w} = \frac{1}{K^2} j \left(k_x \hat{\omega}_y + k_z \frac{d\hat{v}}{dy} \right).$$

Generally the output (ϕ) of interest is the *kinetic energy density* of the perturbation

$$\begin{aligned} E(k_x, k_z) &= \frac{k_x k_z}{16\pi^2} \int_{-1}^{1} \int_{0}^{\frac{2\pi}{k_x}} \int_{0}^{\frac{2\pi}{k_z}} \left(u^2 + v^2 + w^2 \right) dy \, dx \, dz \\ &= \frac{1}{8K^2} \int_{-1}^{1} \hat{\omega}_y{}^* \hat{\omega}_y + (K^2)\hat{v}^*\hat{v} - \hat{v}^* \frac{d^2}{dy^2}\hat{v} \, dy. \end{aligned} \tag{3.7}$$

The first expression is a mean-square integral averaged over a "box" with sides that are 1 wavelength long. The wavelength λ_x for the wave number k_x is $\lambda_x = \frac{2\pi}{k_x}$. Based on (3.7)

one can define the following energy metric,

$$\mathcal{M} := \begin{bmatrix} -\Delta & 0 \\ 0 & I \end{bmatrix}. \tag{3.8}$$

Then the kinetic energy density can be expressed in terms of the transformed state, $\hat{\varphi} = [\hat{v}; \hat{\omega}_y]$, as

$$E(k_x, k_z) = \frac{1}{8K^2} \int_{-1}^{1} \psi^\dagger \mathcal{M} \psi \, dy := < \hat{\varphi}, \, \mathcal{M}\hat{\varphi} >_e . \tag{3.9}$$

This defines an energy inner product on the Hilbert space $L_2[-1, 1]$.

The kinetic energy density has an interesting interpretation when the forcing is stochastic, as in [2, 25]. Given a harmonic in x and z input $\mathbf{d}(x, y, z, t)$ in (3.6), that is also a Gaussian temporally stationary (δ-correlated), unit variance, second-order random field, the covariance of the stochastic process is given by

$$\mathfrak{U} = \int_{0}^{\infty} e^{t\mathcal{A}} e^{t\mathcal{A}^*} \, dt.$$

This is simply the controllability gramian for $\mathcal{B} = \mathcal{I}$. As discussed in Chapter 2, it can be computed using the operator Lyapunov equation (2.22a), i.e.,

$$\mathcal{A}\mathfrak{U} + \mathfrak{U}\mathcal{A}^* = -\mathcal{I}.$$

The trace of $\mathfrak{U}$ is then the $\mathcal{H}_2$ norm of the impulse response of the stochastically forced system (3.6) with $\mathcal{C} = \mathcal{I}$. If we use the energy inner product above and transform the state such that $\zeta = \mathcal{M}^{1/2}\varphi$, then $\tilde{\mathcal{A}} = \mathcal{M}^{1/2}\mathcal{A}\mathcal{M}^{-1/2}$. The corresponding covariance can be used to find the *ensemble average energy density* or the $3D$ sustained variance of the statistical steady-state.

In both the stochastic [2] and deterministic [44, 46] settings the coupling operator , $\mathfrak{C}$ in (3.5), was identified as the amplification mechanism. Stochastic studies showed that non-normality of the linear operator leads to sustenance of high levels of variance despite linear stability [25].

3.3.4   Dominant Mode Shapes

One of the common features of energy amplification and transient growth analysis is the identification of important flow features. In fact, all of the analysis discussed so far identified streamwise and quasi-streamwise phenomena as dominant modes. For example, Butler and Farrell [10] found that streaks of streamwise velocity naturally arise from the set of initial conditions that produce the largest energy growth in wall-bounded shear flows. The disturbances they associated with this maximum amplification are streamwise vortices. This is not surprising because the most amplified points in the pseudospectra correspond to purely streamwise structures, i.e., those with zero streamwise wave number $k_x = 0$. Streamwise streaks and vortices are pseudomodes of both the linearized Couette and Poiseuille flow problems [90].

The input-output response of the LNS also shows that streamwise constant features are the dominant mode shapes that develop under various perturbations about both the laminar [2, 25, 44, 46] and turbulent mean velocity [13] profiles. Bamieh and Dahleh [2] explicitly showed that streamwise constant perturbations produce energy growth on the order of R^3 whereas disturbances with streamwise variations produce growth on the order of $R^{\frac{3}{2}}$. This relationship was further refined by Jovanović and Bamieh [46] who were able to isolate a number of different amplification mechanisms by looking at componentwise spatio-temporal frequency responses. In this way they were able to order the influence of each velocity component on its own evolution and on that of the other two components. They also determined the overall energy growth and characterized the associated mode shapes. They determined that the energy amplification of perturbations (forcing) from the wall-normal and spanwise directions scale as R^3 whereas all others scale at most with R. Figure 3.2 shows $3D$ sustained variance or ensemble average energy density $E(k_x, k_z)$ for Couette and Poiseuille flow respectively at $R_c = 750$ and $R = 3000$. It confirms that for both flow configurations the maximum energy (sustained variance) corresponds to $k_x = 0$.

Figure 3.2 corresponds to linearly stable flow regimes for both Couette and channel flow. At $R \geq 5772$ Poiseuille flow has unstable eigenvalues corresponding to Tollmien-Schlichting (TS) waves (modes). In this so-called supercritical region one might expect the TS waves to dominate the energy. However, this is not the case; in fact the streamwise constant structures continue to have more energy than the unstable modes well into the

(a) Couette Flow at $R_c = 750$

(b) Channel Flow at $R = 2000$
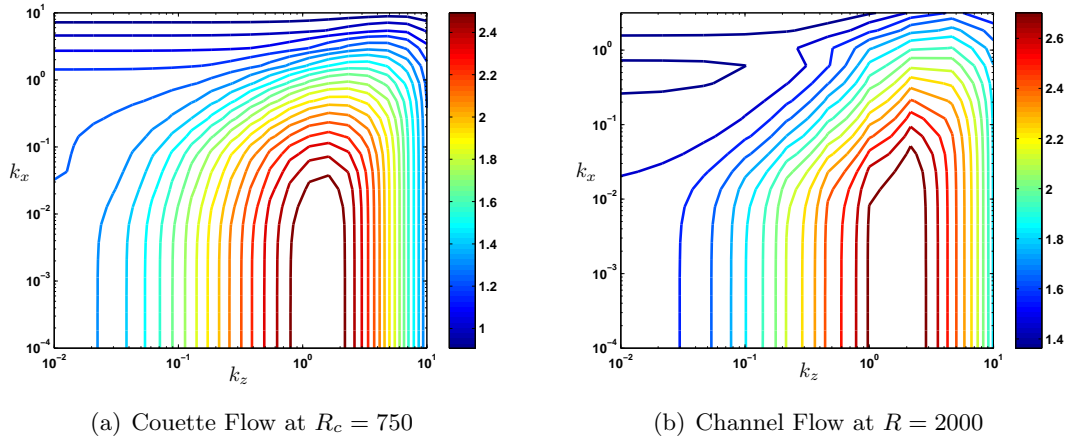
Figure 3.2: Contour plots of $\log_{10} \|H(k_x, k_z)\|_2 = \log_{10}(\sqrt{E(k_x, k_z)})$ for (a) Couette flow at $R_c = 750$ (b) Poiseuille (channel) flow at $R = 2000$. The Reynolds numbers considered here are in the linearly stable regimes but above the Reynolds number where turbulence has been numerically and experimentally observed.

supercritical Reynolds number range [45]. The importance of streamwise constant modes will be discussed further in Chapter 4, where we develop a streamwise constant ($k_x = 0$) model for Couette flow. In the following section we connect the results discussed above to the problem of robust stability (see Section 2.5).

3.4   Transition to Turbulence as a Robustness Issue

The inputs $\mathbf{d}(x, y, z)$ to the forced LNS equations can be used to describe uncertainty or unmodeled effects in parallel shear flows. These sources of modeling errors/uncertainities can arise from assumptions on the boundary conditions or unmodeled dynamics. Distributed wall roughness (i.e., surface imperfections present in any real surface), imperfect alignment of the walls or parameter estimates may be captured through either stochastic or other forcing. Similarly, the inputs may represent unmodeled effects such as the nonlinear terms from NS, thermal fluctuations or acoustic noise. See [8] for a full characterization of the types of uncertainties present in shear flow problems. One can discuss large amplification of these disturbances through the dynamics of the LNS in terms of the robust control concepts introduced in Section 2.5.

Large energy growth/amplification leads to correspondingly large norms $\|H\|$ (where H is the spatio-temporal frequency response of the LNS). The small gain theorem (theorems

2.5.1 and 2.5.2) provides a mathematical measure of the extent to which these sizeable norms are associated with a lack of robustness. As the upper bound on input-output response of the LNS (γ in Theorem 2.5.2) gets large, the amount of permissible uncertainty $\|\Delta\|$ at the spatio-temporal frequencies corresponding to maximum response must be reduced. In the limit as the Reynolds number is increased $\|\Delta\|$ must be sufficiently small throughout the transient phase of the dynamics. Generally the types of disturbances common to shear flow experiments as well as numerical errors in flow simulations tend to be fairly constant throughout the frequency range. In an experiment it impossible to eliminate modeling errors or physical imperfections only at particular frequencies. Thus, it is reasonable to discuss this in terms of the more conservative requirement $\|\Delta\| < \frac{1}{\gamma}$ over the entire frequency spectrum.

Lack of robust stability and/or performance can also be understood in terms of the ε-pseudospectra. The fact that the operators governing linearized Couette and Poiseuille flow are highly non-normal means that they may have a large ε-pseudospectrum that may include points far from the spectrum. This implies that there may be a number of places where the bound γ can get very large. The ε-pseudospectra by definition (particularly Definition 2.5.2 in Chapter 2) indicate that arbitrarily small perturbations can alter eigenvalues that may lead to qualitatively different solutions with different stability properties. Thus, numerical and experimentally observed transitions to turbulence may not be strongly related to the behavior of the solutions of the LNS. Instead, transition may be better understood by thinking of small perturbations of the LNS arising from numerical errors and modeling errors inherent in the study of any physical system. Based on the analysis techniques currently available it is not possible to tell the difference between a nonlaminar solution of the NS equations or a new flow state based on a change in the system's spectrum.

Whether transition is due to large disturbance amplification or a change in the spectra based on the idea of the ε-pseudospectra one can think of transition as a robustness problem rather than a stability problem. The key point in transition is not that the NS equations become unstable as the Reynolds number increases, but instead that they become less accurate in predicting the behavior. This explains why a carefully controlled experiment can maintain laminar behavior at much higher Reynolds numbers. In this way transition may be explained by both secondary (nonlinear) instability and transient growth (disturbance amplification) theories. If one only observes the output of an experiment it is hard to distinguish whether the mechanism involves an additional solution of the NS equations, excitation

of a pseudomode or amplification of disturbances caused by less than ideal experimental or numerical conditions. Either scenario results in the system moving away from the laminar solution. Presently there is no general method to separate behavior caused by perturbations due to nonlinear effects from linear amplification of physical disturbances caused by imperfections inherent to all experiments. Furthermore, although these large norms are present in the absence of any nonlinear affects, the conditions leading to flow disturbance are not well-studied and it is unclear whether nonlinear effects play a role. Existing experimental techniques are not designed to distinguish between the influence of each factor that may lead to the system's energy growth.

3.5   Summary

In this chapter we introduced the Navier Stokes (NS) equations for incompressible flows. Then we developed the linearization of these equations around a nominal flow for the special case of wall-bounded shear flows. We focused on flow between two parallel plates, particularly Couette flow and Poiseuille flow.

We discussed the use of the linearized Navier Stokes (LNS) equations in predicting the Reynolds number at which laminar flows transition to turbulence. We presented various theories regarding the failure of linear analysis to accurately predict this critical Reynolds number. We concentrated on arguments that focus on characteristics of the linear operator, particularly its potential for large transient growth and disturbance amplification. A number of results suggest that large disturbance amplification in the LNS is responsible for transition to turbulence. The main reason energy amplification of the linearized equations is studied is because the LNS are thought to capture the energy growth of the full nonlinear system. Non-normality of the underlying linear operator was identified as the main mechanism of this amplification. Non-normality and the associated linear coupling have been shown to be necessary conditions for both subcritical transition and maintenance of turbulence in smooth wall-bounded shear flows.

The aforementioned failure of the linear analysis was attributed to the fact that transition is not a stability problem but rather a "robustness" problem. We used the robust control concepts detailed in Chapter 2 to illustrate the relationship between non-normality of the underlying operator and the inability of the system to maintain the nominal (lam-

inar) behavior. We then described how the results of the LNS studies can be viewed in a robust control framework. We ended the chapter by showing that both linear and nonlinear transition theories can be interpreted using the paradigm of robust control.

Another important concept introduced in this chapter was the fact that streamwise elongated structures represent the dominant modes of the LNS. In the next chapter we explore this idea further and then develop a model for streamwise constant (i.e., $k_x = 0$) plane Couette flow.

Chapter 4

Streamwise Constant Couette Flow

4.1 Why Streamwise Constant Couette Flow?

There are many existing models for wall-bounded shear flow turbulence. The Navier Stokes (NS) equations are the most comprehensive model for any canonical flow. They provide a complete dynamical system description for each of the three velocity components and the three-dimensional pressure. Unfortunately, these infinite-dimensional, algebraically constrained equations are analytically intractable. They have, however, been extensively studied computationally and numerical solutions do exist. For plane Couette flow, the first numerical solution was computed by Nagata [66]. A detailed discussion of other work related to a full range of numerical plane Couette flow solutions is provided in Gibson et al. [31]. Ever increasing computing power will continue to allow progress toward understanding these local properties. However, a full mathematical understanding of NS even in simple parallel flow configurations remains elusive. For the general equations, there is no mathematical theory that has proven capable of answering basic questions regarding the existence and uniqueness of smooth solutions.

In contrast, the LNS equations (for parallel flows) can be analyzed using well-developed tools from linear systems theory. As previously described, the OSS equations have been extensively used in hydrodynamic stability theory [16]. They have been successfully used to identify the types of disturbances that have the largest effect (energy amplification) on various flow configurations, as well as in identifying the dominant mode shapes in turbulent pipes, channels and Couette flow; see for example [2, 10, 13, 25]. The LNS have also been used to predict certain second-order statistics of turbulent channel flow [44]. These results and a host of others illustrate the power of the LNS as a model for wall-bounded shear flows.

There is however, one fundamental flow feature that linear models are unable to capture; the change in the mean velocity profile as the flow transitions from laminar to turbulent. In addition, linear analysis can only give local information regarding the full (nonlinear) system.

Empirical models can also be quite useful in capturing many aspects of the flow. For example, Proper Orthogonal Decomposition (POD) has been successfully used to construct accurate low-dimensional ordinary differential equation models, e.g. [58, 82]. Since POD requires existing experimental or numerical data, it is not generally used to predict flow behavior but rather to create low-dimensional models to explain observed phenomena. Mean flow and eddy viscosity models are similarly constructed from fitting parameters with data. While all of these data or heuristic models can provide important insight, they also suffer from a lack of connection to the physics of the problem.

The model studied herein is an attempt to merge the benefits of studying a physics-based equation, such as NS, with the analytical tractability of a simplified model, such as the LNS. It is developed based on the assumption that certain aspects of fully developed turbulent flow can be reasonably modeled as homogeneous in the streamwise direction, here denoted *streamwise constant*. The idea that a streamwise constant model is sufficient to capture mean profile changes from laminar to turbulent is strongly supported through input-output analysis of the LNS, as described in Section 3.3.4. Other work by Reddy and Ioannou [74] showed that nonlinear interaction between the $(k_x, k_z) = (0, \pm K)$ modes, where k_x and k_z are respectively the streamwise and spanwise wave numbers, is the primary factor in determining the turbulent mean velocity profile in Couette flow. Further, as was discussed in [67], this type of model may be adequate to capture many of the effects associated with the generation of turbulent wall friction. A $2\frac{1}{2}$D model along similar lines was used to numerically study the mean flow of laminar-turbulent patterns in plane Couette flow [5]. Another type of so-called $2\frac{1}{2}$D model has also been developed for the viscous wall-layer; Tullis and Pollard [92], for example, use such a model to study flow over riblets in this region. The experimental and numerical studies providing the physical basis for assuming homogeneity in the streamwise direction for turbulent Couette is discussed in the following two subsections.

4.1.1 Streamwise Coherence

A growing body of work supports the notion that turbulence in wall-bounded shear flows is characterized by dynamically significant coherent structures, particularly features with streamwise and quasi-streamwise alignment. Near wall streaks [51], for example, have been shown to play a key role in energy production through the "near-wall autonomous cycle" discussed by [35,43,93,95]. This cycle is generally agreed to be a very important mechanism in determining the low-order statistics of turbulent flows in the buffer region and viscous sublayer, i.e., $y^+ \leq 30$ [80]. In addition to the near-wall features, larger streamwise motions, with wavelengths on the order of 10δ, have been known to exist for several decades (see, e.g., [28,53]). More recent high Reynolds number studies have focused on the identification and characterization of this larger-scale streamwise coherence in the core, i.e., [32,39,48,65]. These motions have been called large and very-large-scale motions (respectively LSM and VLSMs). They have a similar signature to the near-wall streaks, but tend to be longer in extent, from one to ten times the outer length scale, δ. There is experimental evidence to suggest that at high Reynolds numbers (for example $R_\tau > 7300$), VLSMs contain more energy than the near-wall structures [39, 40, 65]. In turbulent boundary layers they have also been shown to modulate the near-wall, see for example [40, 61]. This indicates that they may play an important role in both energy production and the flow dynamics across a range of scales.

4.1.2 Couette Flow

In Couette flow, structures reminiscent of VLSMs have long been observed in the core through Direct Numerical Simulation (DNS) of turbulent plane Couette flow [7, 57]. Although some studies raised the concern that the structures were numerical artifacts, recent DNS at higher resolution and with longer box sizes [52,91] have confirmed the existence of long, streamwise, alternating high- and low-speed streaky structures at the centerline. In experiments, VLSMs were first identified through observations of a noticeable peak in the Fourier energy spectrum of the turbulence intensity at low frequencies [50,52]. The Couette flow experiments of Tillmark and Alfredsson [87] found further evidence of these structures in the form of long autocorrelations $R_{uu}(\tau)$ or two-point correlations $R_{uu}(\Delta x)$ as well as periodic variation of spanwise correlations $R_{uu}(\Delta z)$ in the core. The streamwise extent of

these correlations was longer than those generally seen in other wall-bounded flows. Komminaho et al. [52] also found that in contrast to other flows, the streamwise correlations for Couette flow are larger at the center than near the wall. At channel center the zero-cross distances of $R_{uu}(\tau)$ and $R_{uu}(\Delta x)$ have been observed to be three times that of the corresponding structure in Poiseuille flow [49]. This makes Couette flow an ideal candidate to test the applicability of a streamwise constant model.

The analysis in this thesis is limited to Couette flow because it is a well-studied canonical example of wall-bounded shear flow. It also has the desirable feature of being linearly stable for all Reynolds numbers. This feature allows us to study turbulence at only subcritical Reynolds numbers. This separates the issues of instability based transition from those due to transient growth or linear amplification of disturbances. Pipe flow is also linearly stable, but it is much harder to simulate. We do not study boundary layers because a closed form model of a boundary layer is difficult to obtain. Boundary layers are inherently spatially inhomogeneous, which makes it difficult to clearly define the flow boundary.

Along with these desirable properties, Couette flow brings with it some additional challenges in characterizing streamwise constant structures, the first being the fact that it is driven by wall motion and therefore the notion of an outer scale for Couette flow is not well defined. So, although there may be a region that can be scaled in logarithmic units, there is no free stream or wake region. This makes it more challenging to define the part of the channel that can be prudently compared to the overlap layer discussed in much of the literature related to boundary layer flows. Wall-driven motion also means that the shear stress cannot be computed from the pressure. Even with these issues we felt that Couette flow was the best choice to begin exploring the use of a streamwise constant model.

4.2   The $2D/3C$ Model

One way to model streamwise constant flow is a two-dimensional representation. However, in two-dimensional models the full three-dimensional nature of turbulence cannot be captured. In order to mitigate the loss of the third dimension one can instead study a projection of the NS into a streamwise constant cross-section of the flow [75]. This so-called $2D/3C$ model was shown to be the simplest PDE model one can derive from NS [8]. It describes the variation of all three velocity components $\mathbf{u} = (u,\, v,\, w)$ ($3C$) and pressure (p) in the

two-dimensional ($2D$) wall-normal/spanwise (y–z) cross-section.

The model is obtained by setting streamwise (x direction) velocity derivatives in Equation (3.1) to zero (i.e., $\frac{\partial}{\partial x} = 0$). One can explicitly show that for Couette flow this $2D/3C$ formulation also results in a system with zero streamwise pressure gradient. This leaves the following evolution equations for the two-dimensional velocity $\mathbf{u}(y, z, t) = (u, v, w)$,

$$\frac{\partial u}{\partial t} + v\frac{\partial u}{\partial y} + w\frac{\partial u}{\partial z} = \frac{1}{R}\Delta u \tag{4.1a}$$

$$\frac{\partial v}{\partial t} + v\frac{\partial v}{\partial y} + w\frac{\partial v}{\partial z} + \frac{\partial p}{\partial y} = \frac{1}{R}\Delta v \tag{4.1b}$$

$$\frac{\partial w}{\partial t} + v\frac{\partial w}{\partial y} + w\frac{\partial w}{\partial z} + \frac{\partial p}{\partial z} = \frac{1}{R}\Delta w \tag{4.1c}$$

along with the $2D$ continuity constraint

$$\frac{\partial v}{\partial y} + \frac{\partial w}{\partial z} = 0.$$

The velocity field is then decomposed into components $\mathbf{u} = [U + u'_{sw}, V + v'_{sw}, W + w'_{sw}]$, where the linear laminar Couette flow is defined by $U = U(y)$, $V = W = 0$ and $(u'_{sw}, v'_{sw}, w'_{sw})$ are the corresponding time-dependent deviations from laminar in the streamwise constant sense. We assume that the laminar flow satisfies NS, which implies that $\frac{1}{R}\Delta U = 0$.

The equations in (4.1) can be cast in the nonlinear evolution form by defining a stream function

$$v'_{sw} = \frac{\partial \psi}{\partial z}; \quad w'_{sw} = -\frac{\partial \psi}{\partial y},$$

which enforces the appropriate $2D$ continuity equation. Finally, taking $\frac{\partial}{\partial z}$ of (4.1b) $- \frac{\partial}{\partial y}$ of (4.1c) yields the $2D/3C$ evolution equations

$$\frac{\partial u'_{sw}}{\partial t} = -\frac{\partial \psi}{\partial z}\frac{\partial u'_{sw}}{\partial y} - \frac{\partial \psi}{\partial z}\frac{\partial U}{\partial y} + \frac{\partial \psi}{\partial y}\frac{\partial u'_{sw}}{\partial z} + \frac{1}{R}\Delta u'_{sw} \tag{4.2a}$$

$$\frac{\partial \Delta \psi}{\partial t} = -\frac{\partial \psi}{\partial z}\frac{\partial \Delta \psi}{\partial y} + \frac{\partial \psi}{\partial y}\frac{\partial \Delta \psi}{\partial z} + \frac{1}{R}\Delta^2 \psi. \tag{4.2b}$$

We impose no-slip boundary conditions at the wall (i.e., $u'_{sw}(\text{walls}, z, t) = v'_{sw}(\text{walls}, z, t) =$

$w'_{sw}(\text{walls}, z, t) = 0)$. The spanwise extent is infinite.

This model for plane Couette flow is more tractable than the full NS equations yet it captures many of the important flow features lost in a purely $2D$ model by maintaining all three velocity components. Equations (4.2) are an improvement over linear models because it is hypothesized that it is the nonlinearity in the $u'_{sw}(y, z, t)$ equation that provides the mathematical mechanism for the redistribution of the fluid momentum. This redistribution creates larger streamwise velocity gradients in the wall-normal direction and changes the plane Couette velocity profile from linear to its characteristic turbulent "S" shape. Meanwhile, the important features of the LNS are maintained. The underlying linear operator retains the non-normality associated with the potential for large amplification of disturbances in the input-output sense discussed in [46]. There is also an analog of the linear coupling term that is necessary for subcritical transition [36] and maintenance of turbulence [47]. This can be seen by linearizing the evolution equations, which results in the linear system

$$\frac{\partial}{\partial t} \begin{bmatrix} \psi \\ u'_{sw} \end{bmatrix} = \begin{bmatrix} \Delta^{-1}\left(\frac{1}{R_w}\Delta\Delta\right) & 0 \\ -\frac{\partial U}{\partial y}\frac{\partial}{\partial z} & \frac{1}{R}\Delta \end{bmatrix} \begin{bmatrix} \psi \\ u'_{sw} \end{bmatrix}. \tag{4.3}$$

The coupling term is $\frac{dU}{dy}\frac{\partial}{\partial z}\psi = \frac{dU}{dy}v'_{sw}$, which is similar to $\mathfrak{C}$ in the OSS equations (3.5). In fact, applying $\frac{\partial}{\partial z}$ to the u'_{sw} linear evolution equation results in a streamwise constant version of the ω_y equation in the OSS. Therefore, in both equations the coupling term $\mathfrak{C}$ is responsible for transferring energy from the mean shear $\frac{dU}{dy}$. The mechanism involves vortex tilting (or lift up) of the wall-normal vorticity [56]. The mean shear $\frac{dU}{dy}$, which is also the spanwise z vorticity of the nominal (mean) flow, is tilted in the y direction at the rate of $\frac{\partial v}{\partial z}$. The interaction gives rise to an increase in wall-normal y vorticity at the expense of spanwise z vorticity. This lift-up mechanism provides a physical interpretation of the nonmodal or algebraic growth that plays a role in disturbance energy growth.

As with any model, there are assumptions built into the $2D/3C$ model, and it is important to understand how these relate to the physical phenomena associated with turbulent flows. Most obviously, small-scale turbulent activity, including the specifics of structures that are known to exist in the full flow, is lost. While this makes appropriate scaling relationships more difficult to determine, it does not diminish the potential of the model for predicting and understanding key aspects of turbulence in plane Couette flow. The chal-

lenge lies in extending the $2D/3C$ model to incorporate aspects of the streamwise variation that is associated with three-dimensional turbulent flow.

4.3 Global Stability of $2D/3C$ Couette Flow

In this section we present a proof showing global stability of the $2D/3C$ laminar flow solution for all Reynolds numbers. Our development follows the proofs in [9, 69]. In order to establish stability at all Reynolds numbers it is convenient to transform the equations into an R independent form. We apply the change of variables

$$\tau = \frac{t}{R}, \qquad \Psi = R\psi$$

to (4.2) and get

$$\frac{1}{R}\left\{\frac{\partial u'_{sw}}{\partial \tau} = -\frac{\partial \Psi}{\partial z}\frac{\partial u'_{sw}}{\partial y} - \frac{\partial \Psi}{\partial z}\frac{\partial U}{\partial y} + \frac{\partial \Psi}{\partial y}\frac{\partial u'_{sw}}{\partial z} + \Delta u'_{sw}\right\} \tag{4.4a}$$

$$\frac{1}{R^2}\left\{\frac{\partial \Delta\Psi}{\partial \tau} = -\frac{\partial \Psi}{\partial z}\frac{\partial \Delta\Psi}{\partial y} + \frac{\partial \Psi}{\partial y}\frac{\partial \Delta\Psi}{\partial z} + \Delta^2\Psi\right\}. \tag{4.4b}$$

The energy of the $2D$ system (4.4b) is

$$E_\Psi(\tau) := \frac{1}{2}\int_\Omega \left(\tilde{v}^2 + \tilde{w}^2\right)\, dy\, dz,$$

where $\tilde{v} = Rv'_{sw}$ and $\tilde{w} = Rw'_{sw}$ are respectively the scaled wall-normal and spanwise velocity fluctuations and Ω is the domain of the two-dimensional cross-section in the y–z plane. If we apply the stream function definitions (4.2) the energy becomes

$$E_\Psi(\tau) = \frac{1}{2}\int_\Omega \left(\Psi_z^2 + (-\Psi_y)^2\right) dy\, dz = -\frac{1}{2}\left\langle \Psi, \Delta\Psi\right\rangle, \tag{4.5}$$

where $\Psi_z = \frac{\partial \Psi}{\partial z}$, $\Psi_y = \frac{\partial \Psi}{\partial y}$ and the inner product is given by

$$\langle f, g\rangle := \int_\Omega f(y,z)g(y,z)\, dy\, dz. \tag{4.6}$$

The second equality in (4.5) follows from Green's theorem in the plane (or integration by parts) and application of the boundary conditions.

Taking the derivative of (4.5) with respect to time (τ) and noting that Δ is self adjoint

allows us to compute

$$\frac{d}{d\tau} E_\Psi(\tau) = -\frac{1}{2} \langle \Delta\Psi_\tau, \Psi \rangle - \frac{1}{2} \langle \Delta\Psi, \Psi_\tau \rangle$$

$$= - \langle \Delta\Psi_\tau, \Psi \rangle$$

$$= - \langle -\Psi_z \Delta\Psi_y + \Psi_y \Delta\Psi_z + \Delta^2\Psi, \Psi \rangle$$

$$= - \langle \Delta\Psi, \Delta\Psi \rangle.$$

The last equality follows from

$$\langle -\Psi_z \Delta\Psi_y + \Psi_y \Delta\Psi_z, \Psi \rangle = \langle \Delta\Psi, (\Psi_z \Psi)_y \rangle - \langle \Delta\Psi, (\Psi_y \Psi)_z \rangle \equiv 0,$$

which makes use of Green's theorem in the plane and the boundary conditions. This implies that $E_\Psi(\tau)$ is a Lyapunov function for (4.4b), and by Theorem 2.2.3 (the Lyapunov stability theorem for nonlinear semigroups), $\Psi = 0$ is asymptotically stable. In fact it is globally stable since $E_\Psi(\tau)$ is radially unbounded in Ω.

The energy of streamwise evolution (4.4a) is

$$E_u(\tau) := \frac{1}{2} \int_\Omega \left(u'_{sw} \right)^2 \, dy \, dz = \frac{1}{2} \langle u'_{sw}, u'_{sw} \rangle, \tag{4.7}$$

where the inner product is defined by (4.6). The time derivative of $E_u(\tau)$ is

$$\frac{d}{d\tau} E_u(\tau) = \left\langle \frac{d u'_{sw}}{d\tau}, u'_{sw} \right\rangle$$

$$= \left\langle -\Psi_z \frac{\partial u'_{sw}}{\partial y} - \Psi_z \frac{\partial U}{\partial y} + \Psi_y \frac{\partial u'_{sw}}{\partial z}, u'_{sw} \right\rangle + \langle \Delta u'_{sw}, u'_{sw} \rangle \tag{4.8}$$

$$= \left\langle -\Psi_z \frac{\partial U}{\partial y}, u'_{sw} \right\rangle + \langle \Delta u'_{sw}, u'_{sw} \rangle.$$

The last equality follows by applying integration by parts (or Green's theorem in the plane) and the boundary conditions to show that

$$\left\langle -\Psi_z \frac{\partial u'_{sw}}{\partial y} + \Psi_y \frac{\partial u'_{sw}}{\partial z}, u'_{sw} \right\rangle \equiv 0.$$

For Couette flow $\frac{\partial U}{\partial y} = C\mathcal{I}$, where C is a constant that depends on the wall-normal

height h. It is a well-known fact that Δ is a negative definite operator, so

$$
\begin{aligned}
\frac{d}{d\tau}E_u(\tau) &= \left\langle -\Psi_z\frac{\partial U}{\partial y}, u'_{sw}\right\rangle + \left\langle \Delta u'_{sw}, u'_{sw}\right\rangle \\
&\leq \lambda_{max}(\Delta)\|u'_{sw}\|^2 + C\,\|\Psi_z\|\,\left\|u'_{sw}\right\|,
\end{aligned}
\tag{4.9}
$$

where $\lambda_{max}(\Delta)$ is the maximum eigenvalue of Δ. The energy E_u is therefore decreasing along the flow of (4.4a) whenever

$$
\left\|u'_{sw}\right\| \geq -\frac{C\,\|\Psi_z\|}{\lambda_{\max}(\Delta)} = K\|\Psi_z\|,
$$

where K is a constant.

The energy E_u does not monotonically decrease with time so $E_\Psi + E_u$ is not a Lyapunov function for the system (4.4). We instead consider

$$
V_\alpha(\Psi, u'_{sw}) := \alpha^2 E_\Psi + E_u = -\alpha^2\frac{1}{2}\langle \Psi, \Delta\Psi\rangle + \frac{1}{2}\langle u'_{sw}, u'_{sw}\rangle
\tag{4.10}
$$

as a potential Lyapunov function. The derivative of this V_α with respect to time τ along the flow of (4.4) can be derived using the previous computations. This yields

$$
\begin{aligned}
\frac{dV}{d\tau} &= -\alpha^2\langle \Delta\Psi, \Delta\Psi\rangle + \left\langle -\Psi_z\frac{\partial U}{\partial y}, u'_{sw}\right\rangle + \langle \Delta u'_{sw}, u'_{sw}\rangle \\
&\leq \alpha^2\lambda_{max}(\Delta)\left(\|\Psi_y\|^2 + \|\Psi_z\|^2\right) + \lambda_{max}(\Delta)\|u'_{sw}\|^2 + C\|\Psi_z\|\,\|u'_{sw}\| \\
&\leq -\beta_1^2\left(\|\Psi_y\|^2 + \|\Psi_z\|^2\right) - \beta_2\|u'_{sw}\|^2 + C\|\Psi_z\|\,\|u'_{sw}\|,
\end{aligned}
\tag{4.11}
$$

where $\beta_1^2 := -\alpha^2\lambda_{max}(\Delta)$ and $\beta_2^2 := \lambda_{max}(\Delta)$ are positive scalars. We can then select α in order to make this equation negative. This is more obvious if we rewrite the last expression in (4.11) as

$$
-\beta_1^2\,\|\Psi_y\|^2 - \left(\beta_1\,\|\Psi_z\| - \beta_2\,\left\|u'_{sw}\right\|\right)^2 + (C - 2\beta_1\beta_2)\,\|\Psi_z\|\,\left\|u'_{sw}\right\|,
\tag{4.12}
$$

which is strictly negative for any nonzero solution of (4.4) whenever $C < 2\beta_1\beta_2$. Then, whenever

$$
\alpha > -\frac{C}{2\lambda_{max}(\Delta)},
\tag{4.13}
$$

$V_\alpha = \alpha^2 E_\Psi + E_u$ is a Lyapunov function for (4.4) whenever α satisfies (4.13). Therefore

the laminar flow, i.e., $u'_{sw} = v'_{sw} = w'_{sw} = 0$, is globally asymptotically stable independent of the Reynolds number.

Global stability of these equations implies that without forcing, perturbations will eventually decay. This is consistent with results of [67], who found that after an initial perturbation, a $2D/3C$ model decays (back to laminar) with time. Global stability of the laminar flow also means that there are no other solutions of (4.2) and therefore any transition mechanisms associated with bifurcations, escape from the basin of attraction of the laminar solution or the like are not possible. So, any complications associated with these nonlinear phenomena can be eliminated from the analysis of these particular equations. We do not pursue complete analytical studies of the $2D/3C$ model in this thesis, but instead concern ourselves with showing the applicability of the model in describing important features of the flow field. We explore the flow features through a simulation in Chapter 5 and study of forced solutions of the $2D/3C$ model in Chapter 6. Analytical solutions for a certain class of ψ are presented in Section 6.5. The analytical properties of the linearized $2D/3C$ model are discussed in other work, see for example [2, 8, 46]. The fact that global statements about these equations can be made implies that future analytical studies of the full nonlinear model (4.2) are promising.

4.4 Energy Scaling and the Forced $2D/3C$ Model

In this section we consider the total transient energy growth of (4.2), again following the development in [9,69]. The total $2D/3C$ energy in evolution of the deviations from laminar flow is

$$\mathcal{E} := \mathcal{E}_\psi + \mathcal{E}_{\tilde{u}} = \int_0^\infty (E_\psi + E_{\tilde{u}}) \, dt,$$

where both E_ψ and $E_{\tilde{u}}$ are the R dependent energies, defined analogously to (4.5) and (4.7). We use the same change of variables as before:

$$E_\psi(0) = \frac{1}{R^2} E_\Psi(0) \quad \text{and} \quad \int_0^\infty E_\psi \, dt = \frac{1}{R} \int_0^\infty E_\Psi \, d\tau.$$

Similarly

$$\int_0^\infty E_{\tilde{u}} \, dt = R \int_0^\infty E_u \, d\tau.$$

For zero initial deviation from laminar (i.e., $u'_{sw}(y, z, 0) = 0$) with input Ψ and output u'_{sw} we have the following linear gain relationship,

$$g(\Psi) := \frac{\int_0^\infty E_u \, d\tau}{\int_0^\infty E_\Psi \, d\tau}. \tag{4.14}$$

This has been shown to have a finite upper bound for general parallel flows [9]. It is also nonzero for $\frac{dU}{dy} \neq 0$, i.e., in the presence of nominal shear. Since the $\Psi(t)$ evolution (4.4b), is independent of u'_{sw}, its state $\Psi(y, z, t)$ is completely determined by its initial conditions $\Psi(y, z, 0)$. To indicate this we abuse the notation and write $g(\Psi(0))$ for $g(\Psi)$.

Using the above relations and the fact that by definition the function $g(\Psi)$ is constant under scaling [9], i.e., $g(\Psi(0)) = g(\psi(0))$,

$$\mathcal{E}_{\tilde{u}} = R \int_0^\infty E_u \, d\tau = Rg(\Psi) \int_0^\infty E_\Psi \, d\tau = Rg(\psi(0)) \int_0^\infty E_\Psi \, d\tau.$$

The ratio of $\mathcal{E}$ to the initial energy $E(\psi(0))$, is

$$\begin{aligned}
\frac{\mathcal{E}_\psi + \mathcal{E}_{\tilde{u}}}{E_\psi(0)} &= \frac{\frac{1}{R} \int_0^\infty E_\Psi \, d\tau}{\frac{1}{R^2} E_\Psi(0)} + \frac{Rg(\psi(0)) \int_0^\infty E_\Psi \, d\tau}{\frac{1}{R^2} E_\Psi(0)} \\
\frac{\mathcal{E}}{E_\psi(0)} &= \left(R + g(\psi(0))R^3\right) \frac{\int_0^\infty E_\Psi \, d\tau}{E_\Psi(0)}
\end{aligned} \tag{4.15}$$

This shows that for initial states with $u'_{sw}(0) = 0$ and $\psi(0) \neq 0$ the energy growth scales as a function of R^3. The R^3 scaling comes from the growth in u'_{sw} based on coupling with ψ, i.e., the spanwise and wall-normal perturbations. This is similar to the transference of energy through interaction with the background shear that is responsible for energy amplification in the LNS.

This energy scaling relationship indicates that although the streamlined laminar flow is stable for all R, there is large amplification of background disturbances. This potential for R^3 energy growth is the same as that seen in the LNS [2] and as such the $2D/3C$ model (4.2) is also not robust for large R.

One can study a forced version of (4.2) in order to account for the uncertainties in a similar manner to that used in studies of the OSS equations. If we define the inputs

$\mathbf{d} = [d_u; \, d_\psi]$, then the nondimensionalized equations (4.4) become

$$\frac{\partial u'_{sw}}{\partial \tau} = -\frac{\partial \Psi}{\partial z}\frac{\partial u'_{sw}}{\partial y} - \frac{\partial \Psi}{\partial z}\frac{\partial U}{\partial y} + \frac{\partial \Psi}{\partial y}\frac{\partial u'_{sw}}{\partial z} + \Delta u'_{sw} + R\,d_u \qquad (4.16\text{a})$$

$$\frac{\partial \Delta \Psi}{\partial \tau} = -\frac{\partial \Psi}{\partial z}\frac{\partial \Delta \Psi}{\partial y} + \frac{\partial \Psi}{\partial y}\frac{\partial \Delta \Psi}{\partial z} + \Delta^2 \Psi + R^2 d_\psi. \qquad (4.16\text{b})$$

This indicates that the effect of noise on the streamwise equation scales with R whereas the effect on the Ψ evolution scales with R^2. In the following chapter we simulate a forced version of the $2D/3C$ model. The results of our simulation study underscores its "lack of robust stability" in that persistent zero-mean small-amplitude Gaussian forcing is shown to cause transition to a "turbulent-like" state.

4.5   Summary

In this chapter, we discussed both the numerical and experimental observations that indicate the use of a streamwise constant model. We then developed a streamwise constant projection of the Navier Stokes equations, which led to the $2D/3C$ (two-dimensional, three-velocity component) model that will be discussed in the remainder of this thesis. The laminar flow was shown to be the globally stable solution of this model. The potential for large disturbance amplification was shown through an energy scaling argument. We discussed how this large energy amplification (on the order of R^3) may push the flow away from laminar. This large input-output energy growth indicates that the $2D/3C$ model is sensitive to disturbances.

Chapter 5

Simulation

In this chapter we simulate a version of the $2D/3C$ model under small-amplitude zero-mean stochastic forcing. We first introduce the Couette flow geometry we are using. Then we describe some of the assumptions used in the simulation and briefly discuss the numerical approach. We compare the simulation results to DNS data from the Kawamura group [91]. We focus on the mean velocity profile because the ability of the $2D/3C$ model to generate an appropriately shaped "turbulent-like" mean velocity profile is the main improvement over earlier studies using linearized models. The change in mean profile from the nominal laminar under zero-mean forcing is a result of the $2D/3C$ nonlinear interactions. We do not discuss second-order statistics as they can be generated through a suitably forced linear model [44].

All of the numerical methods employed in this study are basic low-fidelity methods. The results are meant as a proof of concept, i.e., we are really interested in determining whether or not small-amplitude disturbances can produce a suitably shaped "turbulent-like" mean velocity profile.

The flow geometry used in this chapter and sections 6.1–6.4 is shown in Figure 5.1. In order to facilitate comparisons to the full-field DNS data we had available we elected to use this geometry where $y \in [0, 1]$ rather than the commonly used $y \in [-1, 1]$ (pictured in Figure 3.1 and used for all of the discussion of Chapter 3). In addition, the top wall is moving and the bottom wall is fixed. The Reynolds number employed is $R_w = \frac{U_w h}{\nu}$, where the U_w is the velocity of the top plate, h is the channel height (see Figure 5.1) and ν is the kinematic viscosity of the fluid. For the remainder of this chapter all distances and velocities are respectively normalized by h and U_w, unless otherwise indicated. In the sequel, we will
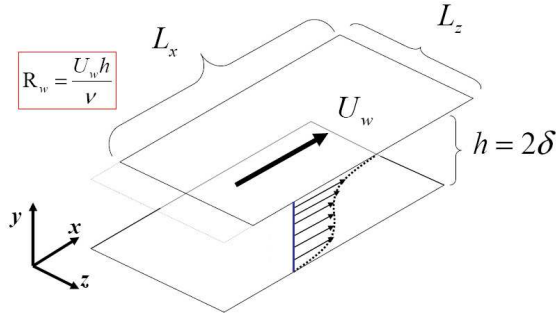
Figure 5.1: Flow geometry for the simulations. Streamwise and spanwise boundaries are periodic, bottom wall is stationary and top wall moves in the x direction with a velocity U_w. The channel half-height is denoted δ and the full channel height is denoted h.

use $(u'_{sw}, v'_{sw}, w'_{sw})$ to denote $\left(\frac{u'_{sw}}{U_w}, \frac{v'_{sw}}{U_w}, \frac{w'_{sw}}{U_w}\right)$, and explicitly indicate the scaling only in the figure labels.

The DNS data is a spatial field (u, v, w, p), at a particular snapshot in time. In order to make comparisons with streamwise constant data we look at a spatial average over the streamwise (x) box length. We denote this x-averaged DNS data (which is also normalized by h and U_w) by $\mathbf{u}_{x_{ave}} = (u'_{x_{ave}} + U(y), v'_{x_{ave}}, w'_{x_{ave}})$ to distinguish it from the streamwise constant velocities, $\mathbf{u}_{sw}$, arising from simulation of the $2D/3C$ model. All time averages are indicated by an overbar, $\overline{(\cdot)}$.

5.1 Modeling Framework

No model is a perfect representation of reality. In addition to modeling assumptions, parameter errors or external influences on the system in question are often ignored. Inaccurate parameter estimates or linearization of a nonlinear system may change the model's ability to predict behavior. Environmental conditions that affect (or disturb) the system may also play an important role in its dynamics. This role is not captured by a typical model. Robust control theory has historically been used to analyze models in the presence of such modeling errors ("uncertainty") [15, 99]. If all of the uncertainties are represented by an uncertainty operator Δ, then the block diagram of Figure 5.2(a) depicts a model subject to this uncertain set Δ. Section 2.5 provides an overview of basic robust control concepts.

We are interested in studying how "robust" the globally stable $2D/3C$ laminar flow is to small disturbances. In order to carry out this study we employ the framework of robust control in a nontraditional manner. Instead of providing a robustness guarantee such as an
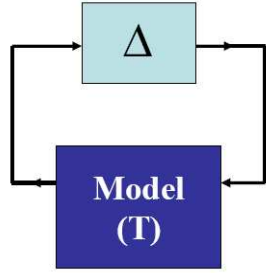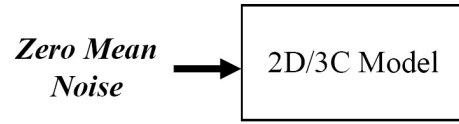
(a) Figure 2.2   (b) The Modeling Framework

Figure 5.2: (a) Reproduction of Figure 2.2, the robust control block diagram for a model subject to modeling errors (uncertainty). Generally a norm bound on Δ specifies the amount of uncertainty that a model can have before a desired property is lost (i.e., if the model is stable for $\|\Delta\| \leq \frac{1}{\gamma}$, this implies robust stability). This is discussed in detail in Section 2.5. (b) The approximation for illustrating the $2D/3C$ model's lack of robustness. Here we use the zero-mean noise as an approximation for the modeling errors and uncertainty (i.e., to represent the Δ block in Figure 5.2(a)). The noise acts as an additive "uncertainty" at each time step.

upper bound on the model uncertainty, (i.e., a norm bound on Δ from Figure 5.2(a)) we describe the extent to which the laminar flow state is "fragile" (i.e., unable to be maintained in the face of infinitesimal disturbances). We show that persistent (in time) small stochastic disturbances result in a new mean flow behavior. The underlying idea is similar to studies of the LNS that hypothesize that transition to turbulence in linearly stable flows is the result of large disturbance amplification. Many of these studies conclude that transition is a "robustness" rather than a "stability" problem. One can think of our approach as investigating the inverse robustness (or 'fragility') problem, i.e., we are really discussing a lack of robustness or the system's "sensitivity". We define **sensitivity** loosely as the inverse of robustness, i.e., if a system is not robust to disturbances we say it is "sensitive".

Wall-bounded shear flows are subject to many disturbances that can be modeled through the Δ block in Figure 5.2(a). These uncertainties may represent physical phenomena that are difficult to characterize such as wall roughness or wall vibration as well as conditions that can be characterized by adding additional complexity to the model such as thermal fluctuations, acoustic noise or any other unmodeled conditions that tend to be present in experiments or numerical simulations. A full characterization of the uncertainties found in models of wall-bounded parallel flows is provided in [8]. In DNS and Large Eddy Simulation (LES) the disturbances or uncertainties may arise from the build up of numerical error. For

the $2D/3C$ model in (4.2) the $k_x \neq 0$ modes would also be an example of unmodeled behavior. Similarly, for the LNS the nonlinearities would be included in the uncertainty set. Although some of these are internal to the flow and some are external, from the robust control point of view the origin of the disturbances does not matter.

In order to study the disturbance response of the $2D/3C$ model we abstract the diagram of Figure 5.2(a) into the simplified setting of Figure 5.2(b). It should be noted that for the $2D/3C$ model, the Δ block in Figure 5.2(a) would represent all aspects of the flow not captured in (4.2). This would include both the unmodeled $3D$ effects as well as the coupling from the streamwise components (u) back to the cross-stream components, i.e., the $\Delta\psi$ equation (4.2b). We assume that the relevant effects of unmodeled phenomena that are either internal to the flow or that arise from external sources can be captured in the simplified framework of Figure 5.2(b). This assumption is supported by the ability of the LNS equations (which also do not include two way coupling) to capture the dominant mode shapes in fully developed turbulent flows as well as by the results of the simulation studies described in [29, 30].

We further simplify the forced model by linearizing the $\Delta\psi(y, z, t)$ equation. This is equivalent to recognizing that advection terms in the stream function equation play a lesser role in redistributing momentum. Furthermore, the only input to the ψ evolution equation (4.2b) is the forcing term, so small forcing implies small ψ. Therefore, the nonlinear terms will be at least an order of magnitude smaller than the linear ones and can be neglected. For all of the numerical studies described in Chapter 5 we simulate

$$\frac{\partial u'_{sw}}{\partial t} = -\frac{\partial \psi}{\partial z}\frac{\partial u'_{sw}}{\partial y} - \frac{\partial \psi}{\partial z}\frac{\partial U}{\partial y} + \frac{\partial \psi}{\partial y}\frac{\partial u'_{sw}}{\partial z} + \frac{1}{R_w}\Delta u'_{sw} + d_u \qquad (5.1a)$$

$$\frac{\partial \Delta \psi}{\partial t} = \frac{1}{R_w}\Delta^2 \psi + d_\psi, \qquad (5.1b)$$

with the same boundary conditions as in Equation (4.2). A brief comparison of low-order streamwise velocity statistics obtained using linear versus nonlinear ψ evolution equations is discussed in Section 5.4.5. The results support the use of a linear ψ equation.

In order to capture the full $3D$ system the uncertainty model and its interconnection (as in Figure 5.2(a) or Figure 2.3 described in Chapter 2) would involve nonlinear mixing of modes. To approximate this effect we use noise forcing that includes information at all frequencies, as depicted in Figure 5.2(b). In particular, the inputs $d_u(y, z, t)$ and $d_\psi(y, z, t)$ in

(5.1) are small-amplitude and Gaussian, as in [30]. The input amplitudes are defined using the standard deviation, σ_{noise}. Obviously many of the disturbances/perturbations that comprise the noise sources described herein are intrinsically different than the turbulence field itself. In other words, d_u and d_ψ are not restricted to satisfy the NS equations.

Stochastic forcing of the LNS equations leads to flows that are dominated by streamwise elongated streaks and vortices that are strikingly similar to those observed in experiments [25]. This supports the plausibility of modeling the type of disturbances common to experimental conditions in this manner. The small-amplitude noise assumption is very important in the development of this work, both because we are interested in showing the effect of small-amplitude disturbances on a fragile system and because larger amplitude forcing can change the model's dynamics.

Robust control tools do not require a detailed model of the particular uncertainty. This makes them appealing in situations where there are unknown (or hard to model) environmental influences on the system or when one can only specify the range on a parameter, rather than an exact value. However, since the uncertainty is generally specified through a bound that includes the worst case scenario, the results of this type of analysis may be very conservative. One way to reduce this conservatism is to "structure" or shape the uncertainty. Structured uncertainties rely on some understanding of the modeling errors. We explore structured uncertainties in Section 5.4.4 by introducing a forcing distribution that is more concentrated at the walls. Increased error near the walls is a more physically relevant disturbance model for many of the types of uncertainties in parallel flows. This is true, for example, when the uncertainty source involves wall effects. Measurement errors can also be larger in the near-wall region because of basic physical limitations on the ability to locate measurement equipment. Most importantly, the error associated with the $2D/3C$ assumption is larger in the near-wall region due to the three-dimensional nature of the near-wall cycle [95].

5.2 Numerical Methods

Simulations of (5.1) were carried out using a basic second-order central difference scheme in both the spanwise (z) and wall-normal (y) directions. We applied periodic boundary conditions in z and no-slip boundary conditions in y for both u'_{sw} and ψ. Simulations using

the spectral methods of [98] were also performed for comparison. The pseudospectral simulations employ a Chebyshev interpolant for the wall-normal direction and a Fourier method for the spanwise derivatives. Time stepping is done using a basic forward Euler method. All simulations are initialized with $(u'_{sw}, v'_{sw}, w'_{sw}) \equiv 0$, i.e. a laminar flow condition.

The input d_ψ was zero-mean small-amplitude Gaussian noise evenly applied at each y–z plane grid point and $d_u = 0$. This corresponds to forcing the cross-stream velocity components, v'_{sw} and w'_{sw}, and studying the streamwise velocity response, u'_{sw}. The resulting u'_{sw} may have a nonzero mean because of the nonlinearity in the u equation. We choose not to apply forcing to the streamwise component, u'_{sw}, based on studies of the LNS, which showed that streamwise body forcing produces a much lesser energy response than spanwise or wall-normal forcing [46]. Spanwise and wall-normal forcing to streamwise velocity perturbations produced energy amplification that scaled with R^3. All other input-output pairs scaled with at most R. There was no amplification in the spanwise and wall-normal direction from streamwise forcing, (note this is because, as seen in Equation (3.3), there is no coupling from streamwise to either wall-normal or spanwise velocity in the LNS). Lesser amplification from streamwise forcing also agrees with the $2D/3C$ energy scaling results discussed in Section 4.4. There the R^3 amplification came from the cross-stream coupling from ψ to u'_{sw}. The corresponding growth from the initial condition $\psi(0)$ (where we view initial conditions as a type of forcing) to the orbit $\psi(t)$ is proportional to R. Furthermore, the physics of the problem indicate this it is energy redistribution by streamwise vorticity (i.e., $\Delta\Psi$) that is thought to be the primary effect governing the shape of the turbulent velocity profile [35]. Therefore, it is forcing in this plane that we are interested in for the purpose of demonstrating the ability of this model to capture blunting in the velocity profile.

The two different discretization techniques naturally provide a comparison of different noise forcing distributions. The finite difference methods use even grid spacing whereas the Chebyshev grid results in a higher concentration of noise forcing near the walls.

We assume that we are not introducing significant numerical errors by our methods of discretization, i.e., the introduction of significant noise arises only through the d terms of (5.1). The aspect ratio in all of the simulations was greater than 12 to 1 (spanwise to wall-normal) in order to eliminate box size effects; specifically the usual computational box size was $L_y \times L_z = h \times 12.8h$ with 75×100 grid points. The spanwise extent of $12.8h$ was selected to provide a direct comparison to the full-field DNS data from [91].

The time evolution of $\Delta\psi$ in Equation (5.1) is clearly just a stochastically forced heat equation, i.e., a linear stochastic partial differential equation that can be solved analytically (see for example [83] or [59] and the references therein). This is not pursued here because a simulation is a much simpler way to demonstrate the efficacy of the model. An exposition on Itô calculus and Wiener chaos expansions is beyond the scope of this thesis. Future work may involve pursuing analytical solutions to both the linear approximation to ψ and the full nonlinear system (4.2).

Our primary interest is in the steady-state statistics of u'_{sw}. The fact that u'_{sw} does not influence ψ in (5.1) means that from an implementation perspective the method of computing ψ does not have an effect on the computation of u'_{sw}. In our implementation we input $d_\psi(y, z, t)$ to (5.1b) at each t_i and then use this to compute $\psi(y, z, t_i)$. This $\psi(y, z, t_i)$ is then input to (5.1a) to compute the corresponding $u'_{sw}(y, z, t_i)$.

5.3   Comparing DNS Data to $2D/3C$ Assumptions

The Kawamura group provided us with a full spatial field (u, v, w, p) of DNS data at $R_w = 3000$ [91]. We also obtained statistical properties for their data at $R_w = 6000$ and $R = 12800$. Prior to presenting the results of the simulation we analyze this data in the light of the $2D/3C$ model to determine the extent to which the model's assumptions can be adduced through this data.

Throughout Chapter 5 and in sections 6.1–6.4 we approximate a streamwise constant projection of the DNS data through a streamwise (x) average over the box length. As previously mentioned, these x-averaged DNS velocities are denoted $\mathbf{u}_{x_{ave}} = (u'_{x_{ave}} + U, v'_{x_{ave}}, w'_{x_{ave}})$, where $(U(y), 0, 0)$ represents the laminar flow and $(u'_{x_{ave}}, v'_{x_{ave}}, w'_{x_{ave}})(y, z)$ represent the corresponding deviations from laminar in an x-averaged sense at a particular snapshot in time. We use streamwise averages (i.e., focus on motions that have streamwise coherence of the order of the box length) because it is a first-order approximation of the streamwise constant component of the DNS data.

Full details of the DNS data set can be found in [91]. A brief review of the key aspects is given here. Three Reynolds numbers were considered, $R_w = 3000, 8600$ and 12800, with respective computational domain sizes $L_x \times L_y \times L_z = 44.8h \times h \times 12.8h$, $1024 \times 96 \times 512$ grid points, and a sampling time $(\frac{tU_w}{L_x})$ of 91. A fourth-order finite difference scheme proposed

in [64] was employed for the x and z directions. A second-order finite difference method was used for the y direction.

The friction coefficient, $C_f = 9.59 \times 10^3$, is somewhat higher than in other studies, such as [77]. Filling this friction factor into the relationship developed by [76],

$$\sqrt{\frac{C_f}{2}} = \frac{G}{\log_{10}(1/4R_w)} \quad \text{where} \quad C_f = \frac{\tau_w}{1/2\,\rho\,(1/2 U_w)^2} \tag{5.2}$$

with τ_w used to denote shear stress at the wall, leads to an experimental constant $G = 0.199$. Other values reported in the literature include $G = 0.19$ and $G = 0.174$ both from [76] based on the data of Reichardt and Robertson respectively and $G = 0.182$ from the experimental study of [19].

The turbulent mean velocity profiles from this DNS compare well both with spectral DNS [52] and experimental studies [85]. Turbulence intensities, Reynolds stresses and budgets of $\overline{u_i' u_j'}$ also show good agreement with the experimental results of [85] and the DNS study of [52], which used a larger box. The two-point correlations in u indicate that the box lengths used in both the streamwise, $R_{uu}(\Delta x)$, and spanwise, $R_{uu}(\Delta z)$, directions are sufficient to eliminate any boundary-condition-related spurious effects.

The ratio of the energy contained in the x-averaged ('streamwise constant') DNS to that of the full field provides a quantitative measure of the extent to which the DNS data can be approximated as streamwise constant. For this comparison we use the squared 2-norm to approximate the energy in each two-dimensional x-averaged velocity component. This is given by

$$\begin{aligned}
\|\beta\|^2 &= \int_{z_1}^{z_{end}} \int_0^1 \beta(y,z)^2 \, dy \, dz \\
&\approx \frac{\Delta z}{2 L_y\, L_z} \sum_{k=1}^{N_z-1} \left(\sum_{j=1}^{N_y-1} \frac{\Delta y_{j+1}}{2} \left[\beta^2(y_{j+1}, z_{k+1}) + \beta^2(y_j, z_{k+1}) + \right. \right. \\
&\qquad\qquad\qquad\qquad\qquad\qquad\left.\left. + \beta^2(y_{j+1}, z_k) + \beta^2(y_j, z_k) \right] \right),
\end{aligned} \tag{5.3}$$

where $\Delta z = z_k - z_{k+1}$ is the space between z grid points and trapezoidal approximations are used for the uneven y-grid.

Table 5.1 shows the total energy (based on the full DNS box) and the percentage contained in each of the x-averaged velocity components (u, v, w) as well as in the deviation

Component	Total Energy Norm $\| \cdot \|$	Percent of Total Energy in x-averaged Norm
u	0.5334	99.1
$u - U$	0.1686	90.2
v	0.0279	19.0
w	0.0412	15.0

Table 5.1: Energy content in streamwise averaged DNS velocity components at $R_w = 3000$.

from laminar (denoted $u - U$), all at $R_w = 3000$. We are interested in the deviation from laminar because it is most representative of the energy associated with the differences in velocity profile for a turbulent versus a laminar flow. Our computations show that x-averaged streamwise velocity contains 99% of the (u) energy, whereas the corresponding deviation from laminar contains 90%. As expected, the x-averaging results in a larger loss of information in the spanwise and wall-normal velocity components.

The DNS field that we obtained is for one particular time step. So, before employing these data to validate the assumptions implicit in the $2D/3C$ model we check that a streamwise average of the data has similar statistics to the time-averaged data. Figures 5.3(a) and 5.3(b) respectively show the mean velocity profiles and turbulence intensities based on the temporal average (turbulent velocity profile), a spanwise average of the streamwise average, and spanwise averages at several x positions. In order to justify using a spanwise average we verified that both of the statistics converge over the spanwise extent. The streamwise and temporal averages for the mean velocity and the turbulence intensity match almost perfectly. This indicates that the spatial, (that is streamwise) first and second central moments computed over this particular box length do not change with time. The mean profiles computed at each of the spanwise locations also show good agreement with the time-averaged profile indicating that the mean flow is indeed approximately streamwise constant. The turbulence intensities show less agreement at the individual x positions, which is not unexpected because this statistic is more sensitive to small-scale turbulent behavior. The computational box length and grid size of these DNS data was visually determined to be large enough for the mean velocity profile to statistically converge in both the streamwise and spanwise directions.

An examination of the DNS streamwise velocity field at $y^+ = 29$, close to the outer edge of the region affected by the near-wall cycle, reveals the signature of streamwise elongated,

(a) Average Velocity

(b) Turbulence Intensities
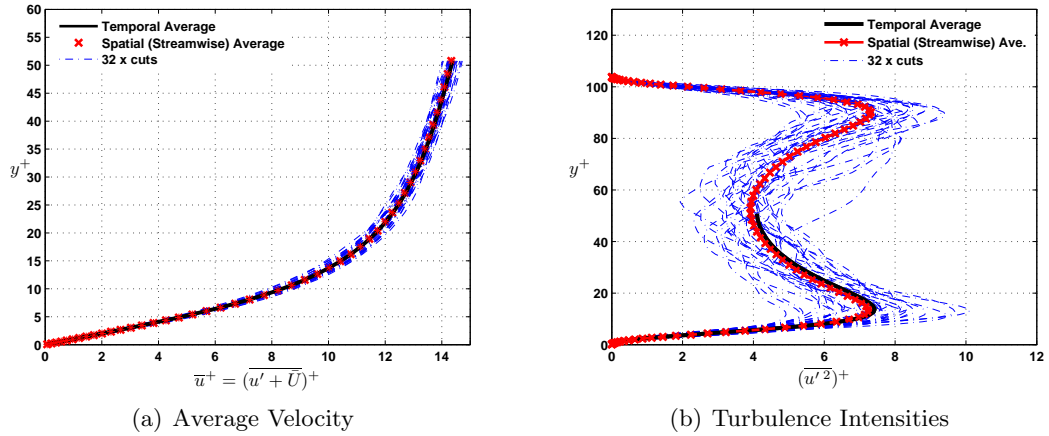
Figure 5.3: (a) Average velocity $\overline{u(x,y,z,t)}$ versus wall-normal location from the DNS field at 32 different x locations compared to both the spatial average (streamwise averaged) $u_{x_{ave}}(y,z)$ and the temporal average of the associated DNS data versus the wall-normal location. (b) Average velocity fluctuations $u'_{x_{ave}}(x,y,z)^2$ from the DNS field at 32 different x locations compared to both the spatial average (streamwise averaged) $u'_{x_{ave}}(y,z)^2$ and the temporal average $\overline{uu'(x,y,z,t)}$ of the associated DNS data.
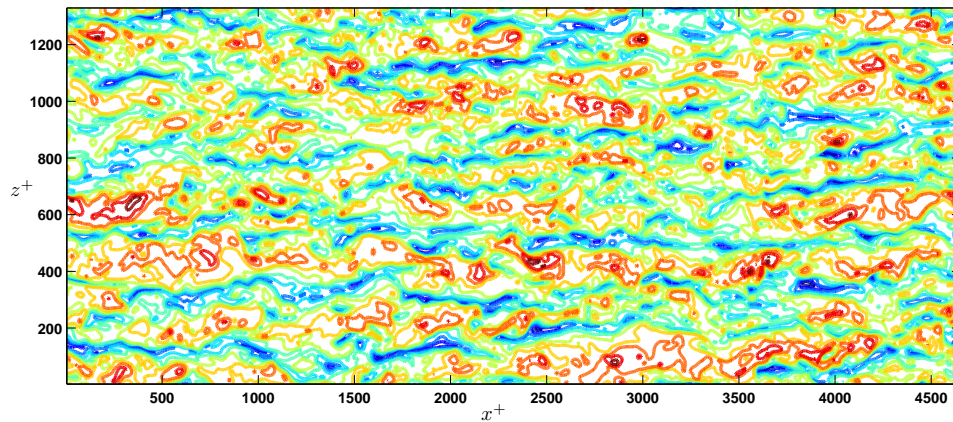
Figure 5.4: A z–x plane contour plot of the streamwise velocity, u, from the DNS field, (bottom up view) at $y^+ = 29$. Red contours denote regions of higher velocity (high-speed streaks) and blue contours indicate lower speed regions.

(a) Average over 25% of streamwise box   (b) Average over full streamwise box
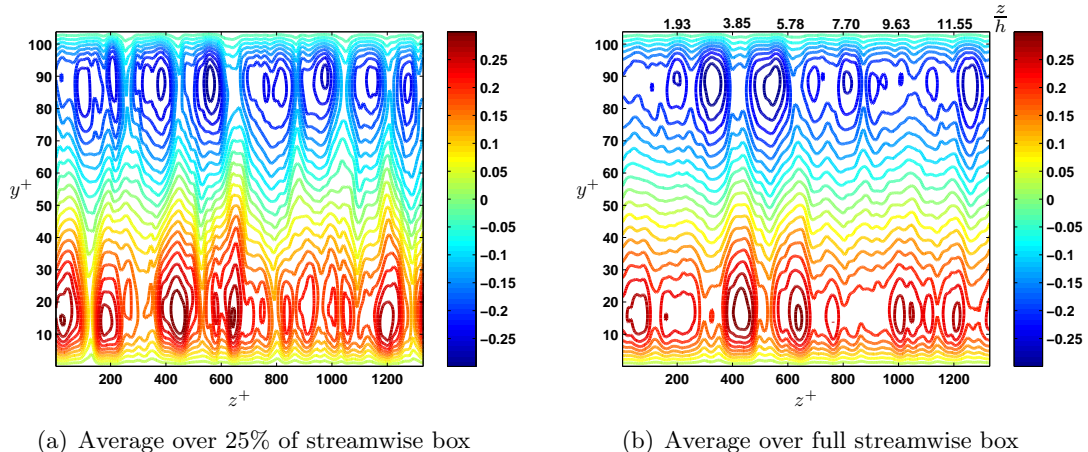
Figure 5.5: y–z plane contour plots of the x-averaged DNS deviations from laminar $(u'_{x_{ave}})$ (a) averaged over 25% and (b) the full streamwise box length.

large-scale streaks in the streamwise/wall-normal plane of the full field (Figure 5.4). These streaks are also visible in Figure 5.5(a) and 5.5(b), which depict contour plots of the deviation from laminar flow, $u'_{x_{ave}} = u_{x_{ave}} - U$, when averaged over 25% of the streamwise field and the full field respectively. Clearly, increasing the averaging length acts as a filter on structures of different streamwise extent. The average over the full box length retains strong evidence of structures across the entire spanwise/wall-normal plane. In particular, the strongest signature near the wall is in qualitative agreement with the near-wall model of energetic structures centered around $y^+ \approx 15$ with a statistical diameter of $y^+ \sim 30$. Another important feature of Figure 5.5(b) is that the peaks associated with the maximum deviations from laminar flow reach across the channel height and are out of spatial phase with one another, top to bottom.

The above analysis shows that there is good agreement between the DNS data and our assumptions.

5.4 Simulation Results

In this section we present the results for simulations at three Reynolds numbers, $R_w = \frac{U_w h}{\nu} = 3000$, $R_w = 6000$ and $R_w = 12800$. Table 5.2 shows all of the R_w-σ_{noise} combinations considered. Cases 1–6 use the finite difference approximations described earlier, while Spec 1 and 2 represent the pseudospectral simulations.

Case	Reynolds Number	σ_{noise}	$L_y \times L_z$	$N_y \times N_z$	Squared Norm of the Noise Input
1	3000	0.01	$h \times 12.8h$	75×100	0.0565
2	3000	0.0125	$h \times 12.8h$	75×100	0.0882
3	3000	0.004	$h \times 12.8h$	75×100	0.009
4	8600	0.004	$h \times 12.8h$	75×130	0.0092
5	12800	0.004	$h \times \sim 16.5h$	75×130	0.0092
6	12800	0.001	$h \times \sim 16.5h$	75×130	$5.77e - 04$
Spec 1	3000	0.001	$h \times \sim 14.5h$	40×81	–
Spec 2	3000	0.002	$h \times \sim 14.5h$	40×81	–

Table 5.2: Computation details.

The initial simulation (Case 1 in Table 5.2) was carried out at $R_w = 3000$. The forcing $d_\psi(x, y, t)$ was drawn from a zero-mean Gaussian distribution with standard deviation (noise amplitude) $\sigma_{noise} = 0.01$. It was applied at every point in the mesh. The window used for time-averaging was $\Delta t = 100,000 \frac{h}{U_w}$.

5.4.1 Flow Features

A contour plot of $\overline{u'_{sw}(x, y, t)}$ from the Case 1 2D/3C simulation is shown in Figure 5.6(a). For comparison the plot of $u'_{x_{ave}}(y, z)$ from the full-field DNS data at $R_w = 3000$, with the same contour levels is shown in Figure 5.6(b). The overall qualitative agreement is good. The signature of streamwise elongated, large-scale streaks are visible in both plots. In addition, the offset in spatial phase from top to bottom between $u'_{x_{ave}}$ (DNS) peaks and observed in experiments is also reproduced in $\overline{u'_{sw}(x, y, t)}$ from the 2D/3C simulation.

A Fast Fourier Transform (FFT) of $u'_{x_{ave}}$ over the span (z direction) estimates the z wave number of the DNS data to be roughly $\lambda_z \approx 1.8$. Linear analysis at $k_x = 0$ using the techniques described in Section 3.3.4, (corresponding to Figure 3.2) estimate $\lambda_z = 2.2$. It is clear in Figure 5.6(a) that the dominant wave number from the simulation data is somewhat longer than the DNS. Frequency analysis of $\overline{u'_{sw}}$ indicates that most of the energy resides in wavelengths between $4 \leq \lambda_z \leq 6.1$. Visual inspection of Figure 5.6(a) indicates that there is also a significant contribution from $\lambda_z \approx 2$. A higher fidelity simulation would allow a more precise estimate of the frequency content.

The DNS data is averaged over a much shorter box length than the equivalent of the $\Delta t = 100,000 \frac{h}{U_w}$ time-average used for the contour plot of Figure 5.6(a). In order to see if this makes a difference in the dominant wavelength of $\overline{u'_{sw}}$ we also took an average over

(a) $\overline{\frac{u'_{sw}}{U_w}}$ from Case 1

(b) $\frac{u'_{x_{ave}}}{U_w}$ from DNS Data

(c) $\overline{\frac{u'_{sw}}{U_w}}$ from Case 1
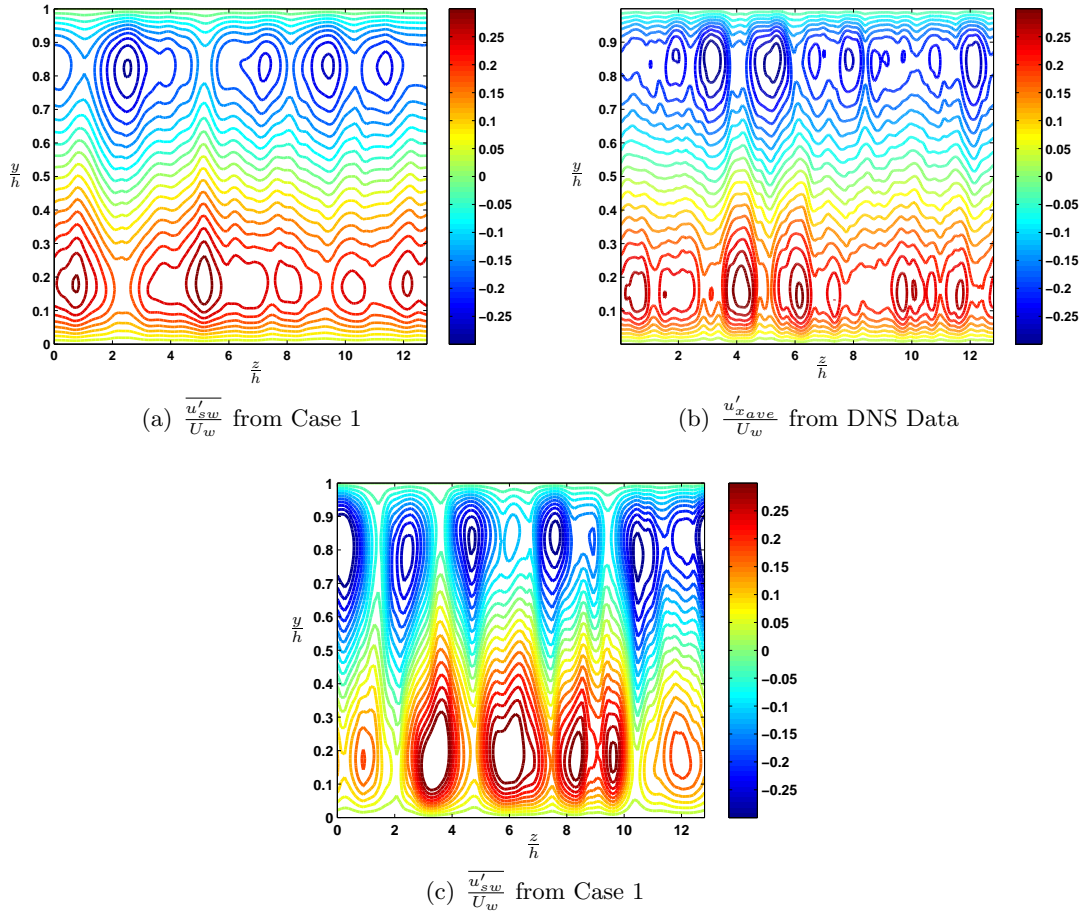
Figure 5.6: Contour plots of (a) $\overline{u'_{sw}(y,z,t)}$ obtained from the $2D/3C$ model for Case 1 and (b) x-averaged DNS data. (c) Contour plot of $\overline{u'_{sw}(y,z,t)}$ with a shorter time-average (10% of the one in (a)). All plots are for $R_w = 3000$ and have the same contour levels.

$\Delta t = 10,000\frac{h}{U_w}$. A contour plot of $\overline{u'_{sw}}$ with this shorter time average is pictured in Figure 5.6(c). An FFT of this data over the span (z direction) indicates that $\lambda_z \approx 2.5$. This makes sense because as the time average gets longer and longer we anticipate an increase in the spanwise z wavelength. We expect the spanwise variation to approach zero with a long enough time-average.

Surface plots of $\overline{u'_{sw}}$ from Case 1 and $u'_{x_{ave}}$ from the $R_w = 3000$ full-field DNS data are presented as Figures 5.7(a) and 5.7(b). These provide another view of the data and further evidence that the qualitative features of the Case 1 results are consistent with the full-field DNS data.

The plots of Figure 5.6(a), 5.6(c) and 5.7(a) show that persistent small-amplitude dis-

(a) $\frac{u'_{sw}}{U_w}$ from Case 1

(b) $\frac{u'_{x_{ave}}}{U_w}$ from DNS Data
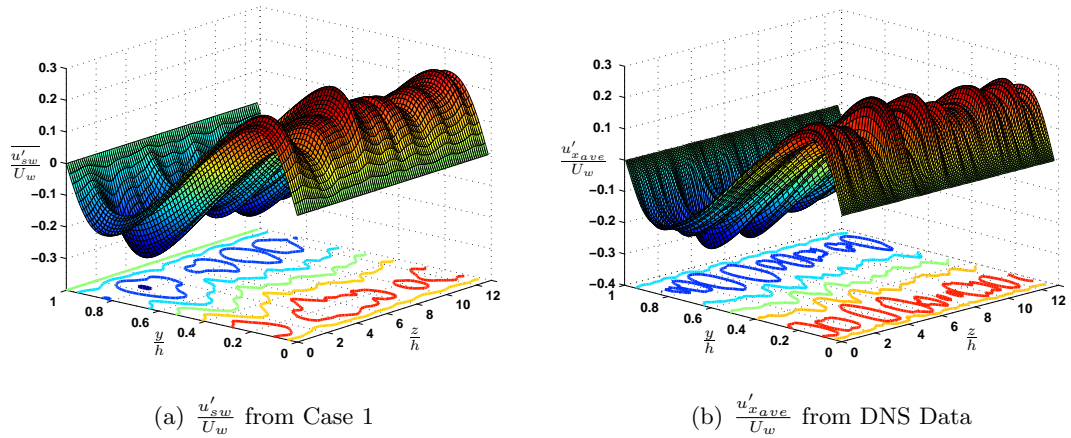
Figure 5.7: Surface plots of (a) of $\overline{u'_{sw}(y, z, t)}$ obtained from the $2D/3C$ model for Case 1 and (b) x-averaged DNS data. Both with $R_w = 3000$.

turbances (forcing) are sufficient to move the flow from the laminar state to one that has similar features to $3D$ fully developed turbulent flow. In the sequel we refer to this new state as the $2D/3C$ turbulence or a "turbulent-like state". We often refer to the corresponding time-averaged mean velocity profile $\overline{u'_{sw}}$ as the $2D/3C$ turbulent velocity profile.

5.4.2 Mean Velocity Profile

Figure 5.8(a) shows the mean velocity profile (i.e., $\overline{u_{sw}}$) from Case 1 in Table 5.2. It indicates reasonably good agreement with the statistics of the DNS data from [91] at the same R_w. The mean profile in inner units can also be compared to DNS if we use (5.2) to estimate the friction velocity u_τ. Figure 5.8(b) makes this comparison using $G = 0.1991$ from [91], which corresponds to both the simulation and DNS at $R_\tau = 52$. The overall agreement of the DNS and Case 1 is good despite the assumption of a friction velocity that corresponds to the full flow. However, it is clear that below $y^+ \approx 20$ the $2D/3C$ model underestimates the expected velocity profile (maximum error 7.4%), and above that it overshoots it (maximum error 2.4%). There are two obvious first-order interpretations of these discrepancies. First, for cases 1–6, the noise is modeled as being evenly distributed across the grid while in reality the noise is likely higher in the buffer region due to the proximity of the wall, and lower in the overlap layer. An improved noise model might improve the agreement. The second interpretation is that a streamwise constant approximation is a better model for

(a) Mean Velocity Profiles   (b) Mean Velocity Inner Units
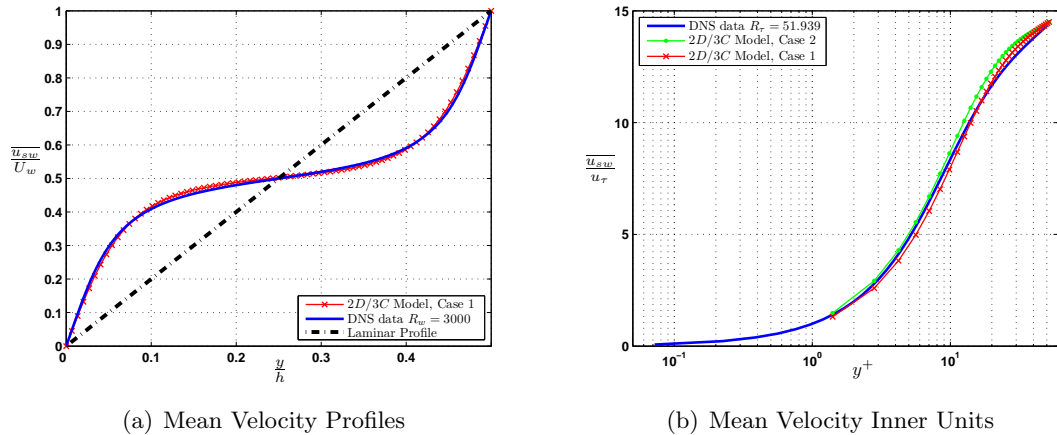
Figure 5.8: (a) Comparison of mean velocity profile from the $2D/3C$ model Case 1 in Table 5.2 with the turbulent mean profile from DNS data. (b) Inner scaled velocity profiles comparison of Case 1 and 2 to the DNS data with $R_\tau \approx 52$ for all data sets.

flow further from the walls, while streamwise variation is more important in the dynamics of the near-wall region (in agreement with the known variation of the spectral distribution of streamwise energy in the full flow).

To investigate whether a different noise amplitude improves the fit in the viscous sublayer a second (constant) noise amplitude at the same Reynolds number, Case 2, is also shown on Figure 5.8(b). The agreement with the DNS is certainly improved below $y^+ = 20$ (maximum error 6.19% at $y^+ = 19$), but at the expense of larger error further from the wall (~ 5–6% between $20 < y^+ < 30$). These results further support the idea that a non-uniform noise forcing with increased noise near the wall versus that at channel center may more accurately reflect the conditions in a real flow field. This idea is further explored in Section 5.4.4.

We note that u_τ can also be computed directly from the velocity gradient at the wall. In both cases R_τ was underestimated by around 10% compared to the estimate from (5.2). Because of the limited number of points near the wall, we opted to use the friction relationship from the full flow, with the understanding that this would only be correct if the $2D/3C$ model with σ_{noise} exactly reproduced the mean flow behavior.

5.4.3 Reynolds Number and Noise Amplitude Trends

In this section four additional Reynolds number and σ_{noise} amplitudes pairs are discussed. The details, along with the computational domain and spatial resolution, for each of the

(a) Mean Velocity in Outer Units

(b) Mean Velocity in Viscous Units
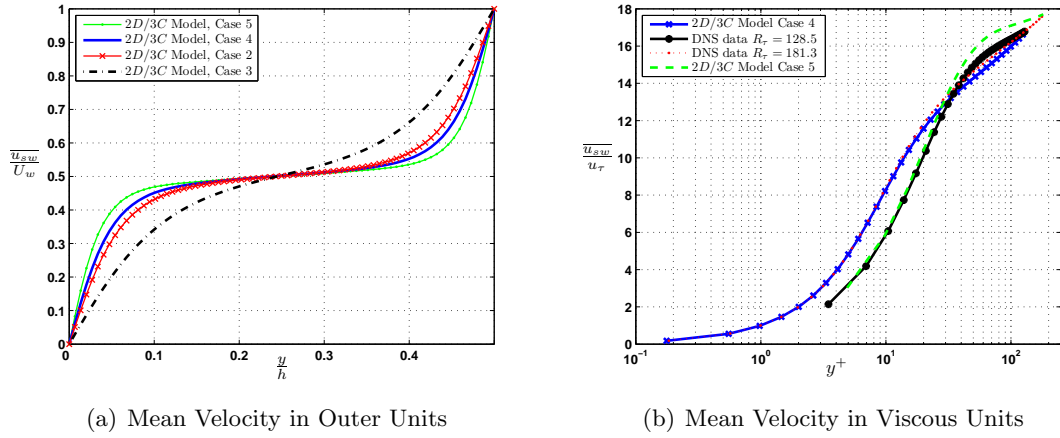
Figure 5.9: (a) $\overline{u_{sw}(y,z,t)}$ from $2D/3C$ Model for Case 2–5 in Table 5.2 and (b) a comparison of u^+ versus y^+ for Case 4 and 5 to DNS data with R_τ computed based on the values used in [91].

cases 3–6 are provided in Table 5.2. Respective values of the norm $\|\cdot\|^2$, as computed in Equation (5.3), of the noise input computed over the box are also reported, since this is a more appropriate measure of the forcing when the box size varies.

The normalized equations (4.16) indicated that the effective forcing was proportional to R^2. This means that an increase in noise produces a similar effect as an increase in Reynolds number (actually $\sqrt{R}$). This is especially clear when dealing with R_τ because an increase in noise amplitude directly corresponds to increased velocity gradients at the wall due to the no-slip boundary conditions.

Figure 5.9(a) shows $\overline{u_{sw}}$ for cases 2–5. Here the increased velocity gradient at the wall, or profile "blunting", with increasing σ_{noise} (noise input energy) is readily apparent. The profiles also become more blunted as the energy input (σ_{noise}) is held approximately constant and the Reynolds number is increased.

In order to quantify the agreement with DNS as the Reynolds number is increased we computed u_τ for Case 4 and 5 (respectively $R_w = 8600$ and $R_w = 12800$ both with $\sigma_{noise} = 0.004$) using (5.2) and the G values for $R_w = 8600$ and $R_w = 12800$, corresponding to $R_\tau = 128.5$ and $R_\tau = 181.3$ respectively, from [91]. Figure 5.9(b) shows the streamwise velocity plots for these cases in inner units compared to DNS data from [91] at the same Reynolds numbers. In Figure 5.9(b) the underestimation of the DNS below $y^+ \approx 30$ (in the buffer layer) is more pronounced than for the lower Reynolds number of Case 1. The agreement

between the simulation and the DNS data above $y^+ > 30$ is similar in magnitude to that of Case 1 (max error $\sim 4.94\%$ for $R_\tau = 128.5$ and 8.39% for $R_\tau = 181.3$, both averaged over $\Delta t = 100,000 \frac{h}{U_w}$). This means that although we are capturing the appropriate trends for the velocity gradients at the wall, the overall near-wall error increases with R_w.

We hypothesize that this worsened agreement may be representative of the increasing scale separation with increased Reynolds number. Near-wall motions that could be effectively considered to be streamwise constant at low Reynolds numbers have an increasingly short streamwise wavelength relative to the motions that scale with outer length scale δ. That the zero-error location consistently occurs around $y^+ = 20$–30, commonly thought to be the upper boundary of the buffer layer, is consistent with this scale separation argument. For the same reason, the lack of model resolution in the near-wall region will be exacerbated with increasing R_w. In robust control terms, this points once again to an increase in the model uncertainty near the wall versus the channel center. A better uncertainty model could be accomplished through the use of a "structured uncertainty", which would include an increase in σ_{noise}) in the near-wall region.

As previously discussed there is a strong relationship between the friction Reynolds number and σ_{noise}. As an illustration of this, Figure 5.10(a) shows that one can obtain similar mean velocity profiles at two different Reynolds numbers simply by adjusting the noise amplitude. A higher Reynolds number requires a smaller (uniform) noise amplitude to develop a mean velocity profile that is similar to that of a lower Reynolds number case with higher noise amplitude. The ability of an almost perfect experiment to maintain laminar flow until higher Reynolds numbers than are typical is a demonstration of the same effect. Disturbance amplification increases with increasing Reynolds number so less noise produces a larger response (more blunting) at higher R. This example makes it clear that the noise amplitude, R and the friction Reynolds number are tightly coupled, while giving further evidence that Reynolds number dependent wall-normal shaping of the noise would be required to get a better model representation of the turbulent mean velocity profiles.

5.4.4   Varying Noise Distribution

A preliminary effort to introduce a non-uniform distribution of noise was carried out through repeating the simulation using a pseudospectral scheme with a Chebyshev interpolant for the wall-normal direction. This scheme naturally produces increased noise near the walls.

(a) Profile Matching at different R_w's
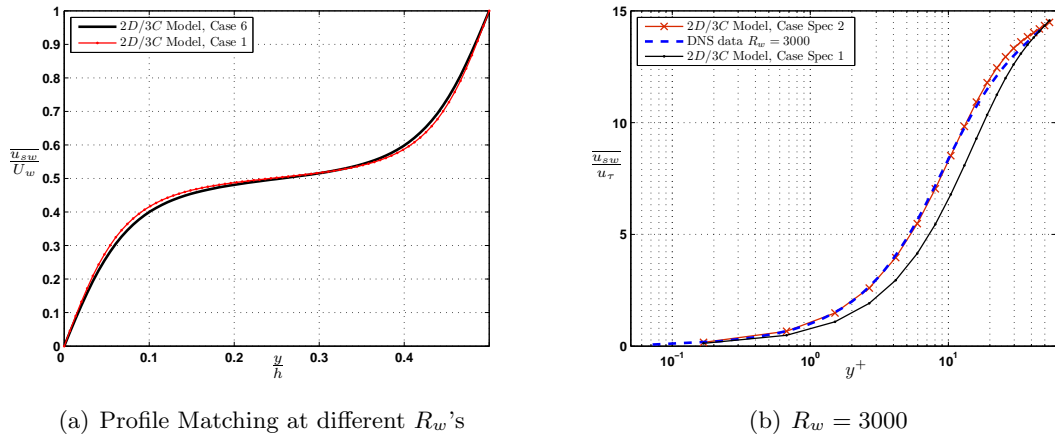
(b) $R_w = 3000$

Figure 5.10: (a) Comparison of $\overline{u_{sw}(y, z, t)}$ from $2D/3C$ Model at for Case 1 ($R_w = 3000$ with $\sigma_{noise} = 0.01$, $\|\sigma_{noise}\|^2 = 0.0882$), and Case 6 ($R_w = 12800$ with $\sigma_{noise} = 0.001$, $\|\sigma_{noise}\|^2 = 5.77e{-}04$) same grid and box size. (b) Comparison of u^+ versus y^+ from $2D/3C$ Model using Chebyshev spacing in y with DNS data at $R_w = 3000$ based on $G = 0.1991$ ($R_\tau \approx 52$).

Cases Spec 1 and Spec 2 in Table 5.2 are two such simulations, both at $R_w = 3000$, with $\sigma_{noise} = 0.001$ and $\sigma_{noise} = 0.002$ respectively. Figure 5.10(b) shows the resulting mean velocity profiles. Clearly the noise level is too low for Spec 1. However, for Spec 2 the maximum error occurs in the buffer layer and is of the order 5–6%. The results of the spectral simulations indicate that by further noise shaping one can improve the agreement throughout the profile and across a range of Reynolds numbers.

5.4.5 Linear versus Nonlinear Ψ Equation

In this section we compare our results from Spec 1 to those obtained using a nonlinear ψ evolution, in order to validate the linear ψ assumption.

Figure 5.11(a) and 5.11(b) show contour plots of ψ at a particular snapshot in time (at steady-state) obtained respectively using the linear (5.1b) and nonlinear (4.2b) evolution equations. They are plotted at the same contour levels. Both simulations were at $R_w = 3000$ with the forcing and computational conditions listed for Spec 1 in Table 5.2. Given the stochastic nature of the simulations these plots are qualitatively very similar. The differences are certainly comparable to what would be obtained through ψ snapshots from two different linear simulations, or the same simulation at two different points in time. An FFT across the span shows that they both have dominant wavelengths of $\lambda_z \approx 4.7$, which is similar the

(a) Linear ψ Equation

(b) Nonlinear ψ Equation

(c) Linear ψ Equation

(d) Nonlinear ψ Equation
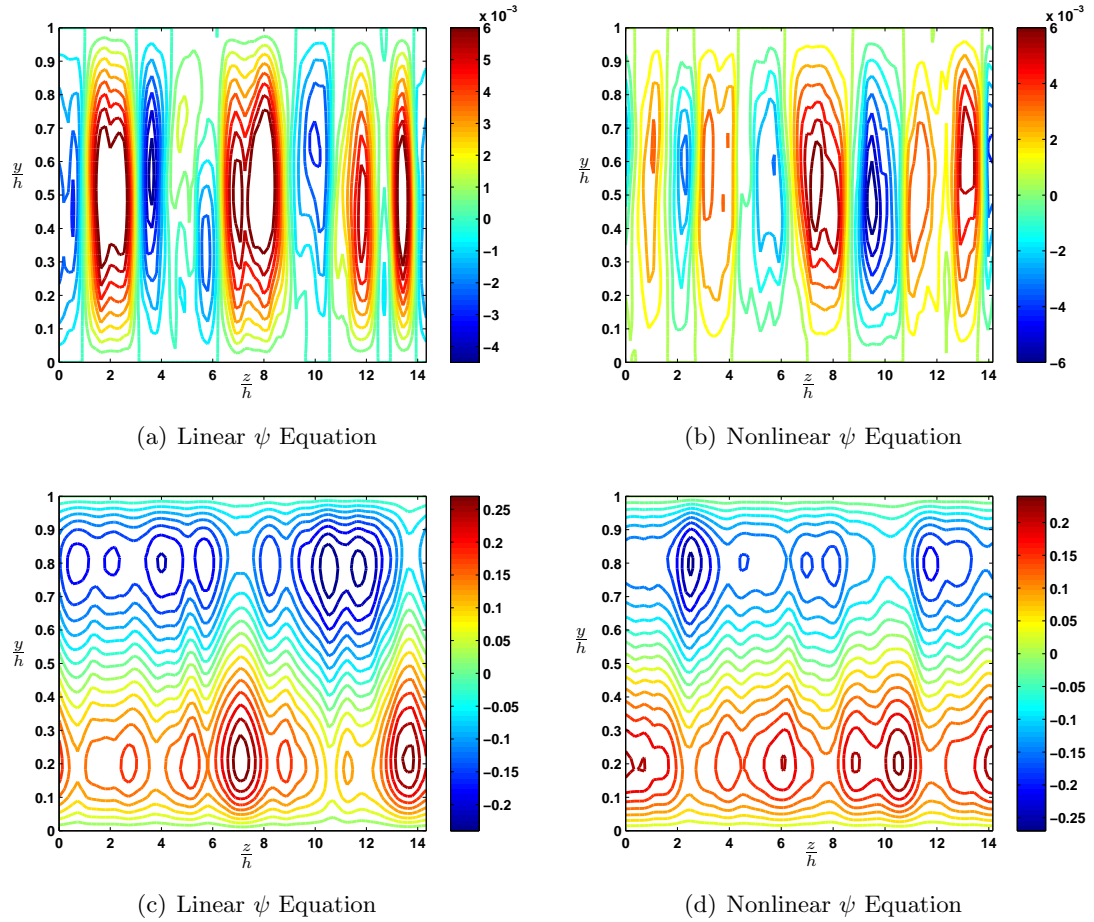
Figure 5.11: (a) Comparison of converged $\psi(y, z, t)$ snapshots from the $2D/3C$ model using the conditions of Spec 1 in Table 5.2 (b) computed using the linear ψ evolution equation (5.1b) (b) the nonlinear ψ evolution equation, (4.2b) with forcing d_ψ. (c), (d) Contour plots of the $\overline{u'_{sw}}$ from the same conditions as in (a) and (b) respectively.

results from Case 1.

Contour plots of $\overline{u'_{sw}}$ for the linear and nonlinear ψ for Spec 1, pictured in Figure 5.11(c) and 5.11(d), also show good qualitative agreement. These plots are plotted at the same contour levels, which are also consistent with Figures 5.6(a) and 5.6(b).

The corresponding mean velocity profiles $\overline{u_{sw}}$ are shown in Figure 5.12. These show almost perfect agreement with a maximum percent error of 0.76%. The corresponding absolute distance between the curves is the same order of magnitude as the numerical error of the simulation method. Based on this excellent agreement we concluded that the linear approximation for ψ is adequate for our investigation.
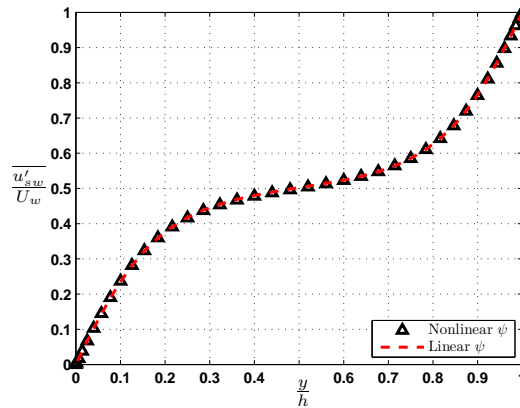
Figure 5.12: The time-averaged streamwise velocity $\overline{u_{sw}}$ arising from simulations with the conditions of Spec 1 in Table 5.2 with linear and nonlinear versions of the ψ evolution equation.

5.4.6 Large-Scale Coherence

Although there is a great deal of evidence to support the existence of these long "stripe-like" structures, the inability to separate them from small-scale turbulent motions that persist throughout the flow has made them difficult to characterize. In this section we review previous efforts to isolate VLSMs and then discuss the extent to which the $2D/3C$ model allows us to characterize these features.

Hamilton et al. [35] attempted to isolate near-wall streaky structures by performing DNS of a highly constrained or "minimal Couette flow", based on the similar work for channel flow [42]. They limited the box size to approximately the minimum value required to capture the average spanwise spacing of a streak and maintain turbulent activity. Their method was to start with a fully developed flow and then continue the simulation with this minimal box size. They were also able to capture long streaks in the core, however due to the limited streamwise box length they were unable to elucidate their full extent. Komminaho et al. [52] attempted to decouple the large streamwise structures from small-scale phenomenon through the application of a local Gaussian filter to the streamwise (u) velocity fluctuations at the centerline. Using this technique they were able to identify streamwise elongated vortex-streak structures that were not fixed in either space or time. Experiments aimed at recreating a type of "minimal Couette flow" were carried out by Kitoh and Umeki [50] through the use of Vortex Generators. This methodology enabled the authors to filter out some of the small-scale turbulent motions and study large-scale streaky structures at the

centerline.

While the $2D/3C$ model provides us with a y–z snapshot in space, in general it is unclear how to reconstruct the streamwise information. The model is designed to capture the mean features of the flow and we are particularly interested in understanding the spatial distribution of large-scale features associated with the model. The simplest way to reconstruct the streamwise information is to convect the flow at the local turbulent velocity using Taylor's hypothesis (i.e., let $x_1 = x_0 + \bar{u}_{turb}(t_1 - t_0)$. However, it is known that in general Taylor's hypothesis does not hold for large scales [14, 48]. Convecting at the local mean velocity is a particularly bad approximation in the near-wall region [14].

In Couette flow the laminar and turbulent velocity profiles always overlap at the centerline, so the centerline velocity (U_c) is not affected by any assumptions of the $2D/3C$ model. The centerline also represents the wall-normal location where the temporal fluctuations are small. For these reasons, it is the most natural location to study first. Kitoh and Umeki [50] compared their convected velocity to a spatial flow visualization and determined that the large scales do in fact convect at U_c at the centerline. Given their results we use the same relationship $x = x_0 - U_c t$ to transform our $2D/3C$ time series data into spatial data. In their work they define the Reynolds number $R_c = \frac{U_c \delta}{\nu} = 4R_w$ (see Figure 3.1) based on the channel half-height δ and the velocity at the centerline U_c, so the discussion in this section refers to both R_w and R_c.

Figure 5.13(a) shows the typical streak pattern on the central plane ($\frac{y}{\delta} = 1$) of Couette flow obtained using the $2D/3C$ model for Case 2, at $R_w = 12800$, with $\sigma_{noise} = 0.004$. For visualization purposes and for direct comparison with the results of Kitoh and Umeki [50] we similarly define a streak as a region where $|\frac{u'_{sw}}{U_c}| \geq 0.05$. Dark regions are low-speed streaks and open areas are high-speed streaks, the light gray regions indicate a neutral region. It is clear that Couette flow generated using the $2D/3C$ model has significantly long streaks in the core region that are qualitatively similar to large-scale features that have been identified through full three-dimensional simulations and experiments.

Previous results [52,87,91] have estimated streaks with streamwise wavelength of $\approx 40\delta$–64δ with spanwise spacing of $\approx 2\delta$–5δ. Figure 5.13(a) shows that the spanwise length scale of our data is similar to these results. The streamwise extent of the structures produced by our model is much longer than reported in other works. This is not surprising as one would expect the results from the $2D/3C$ model to be more coherent than experimental
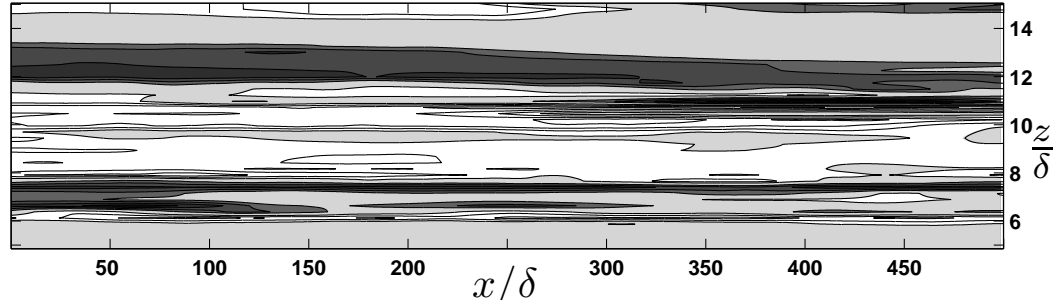
(a) $2D/3C$ Centerline Streak Pattern
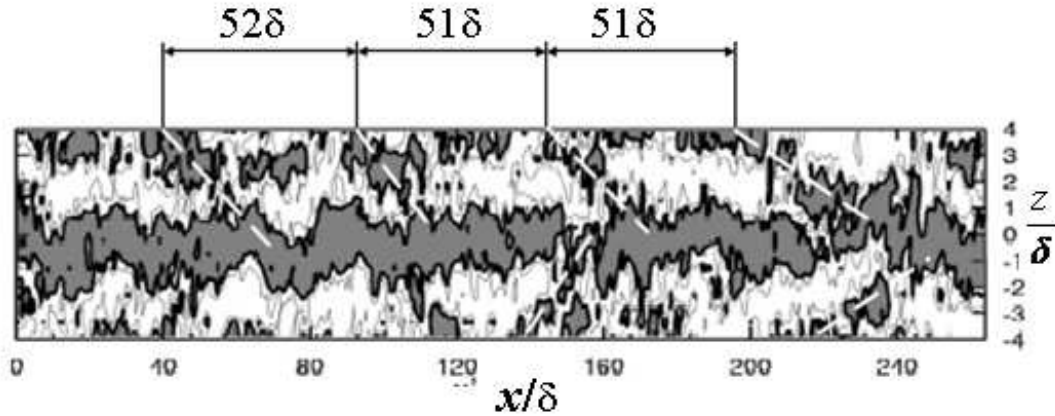
(b) Centerline Streak Pattern from Kitoh and Umeki Experiment [50]

Figure 5.13: (a) Typical streak pattern on the central plane of fully developed turbulent plane Couette flow from the $2D/3C$ model at $R_w = 12800$ ($R_c = 3200$). Dark regions are low-speed streaks, $\frac{|u'_{sw}|}{|U_c|} \leq -0.05$, and the white regions are high speed streaks, $\frac{|u'_{sw}|}{|U_c|} \geq 0.05$, light gray regions are regions without streaks.
(b) Figure 15 from [50] relabeled to match flow variables from the present work. Typical streak pattern on the central plane of Couette flow with vortex generators at $R_w = 15000$, ($R_c = 3750$). Dark regions $\frac{|u'_{sw}|}{|U_c|} \leq -0.05$; open regions, $\frac{|u'_{sw}|}{|U_c|} \geq 0.05$.

data since we are only modeling large-scale behavior.

In the vortex generator case in [50] the streamwise length scale of the structures was approximately 51δ–60δ. However, when they attempted to isolate the large-scale structures using a wavelet analysis they found that the $\sim 60\delta$ streaks form weakly wavy patterns that come together to form larger spatial structures with an average spacing of 300δ–400δ. Figure 15 from this work is shown here as Figure 5.13(b). Here, it is clear that these wavy patterns visually appear as one long streak with an extent $> 250\delta$.

Our model essentially averages out the small-scale effects so it is not possible to distinguish between the long wavy structures reported in [50] and the smaller length scale

structures that comprise them. The low-fidelity simulation methods we employed may also be affecting our ability to pick out the individual streaks. The first DNS of Couette flow [57] also found structures extending about 1000δ. Those conformations were stationary in both space and time and it has been suggested in the literature that insufficient resolution was the cause of the extra coherence in their results. It is also possible that since we are only modeling the mean (large-scale) behavior, we may be missing effects from the temporal fluctuations. Further work is needed to determine the true cause of the increased coherence in our results.

5.5 Disturbance Amplification

All of the results presented in this chapter indicate that a very small amount of stochastic noise forcing limited to the cross-stream components produces a very large response. These small perturbations also create flow behavior that is not a solution of the unforced equations. The ability of this model (4.2), which has a unique solution in the unforced case, to produce a new flow condition due to such a forcing underlies the notion that the model is not robust to small disturbances/uncertainty. The potential for disturbance amplification is not new, in fact it comes directly from the features of the LNS previously discussed, however the creation and maintenance of the new flow state is different and cannot come through the use of a linear model. We now propose a simple characterization of the amplification maintained through the forced response of (5.1).

As detailed in Section 5.1, the idea of modeling the flow as in Figure 5.2(b) relies on small-amplitude input (or Δ) relative to the model states. The lack of robustness comes from large amplification of these disturbances over the course of the simulation. Considering the squared 2-norm of the streamwise component of (5.1) (i.e., $\|\overline{u'_{sw}}\|^2$) to be the increase in energy from the base (laminar) flow, we define a so-called amplification factor

$$\Gamma_u = \frac{\|\overline{u'_{sw}}\|^2}{\|\sigma_{noise}\|^2}, \tag{5.4}$$

which gives us a measure of the output energy for a given input (noise forcing amplitude).

Γ_u is a nonlinear analog of the *ensemble energy density* described in previous studies of the input-output response of the OSS operator, e.g., [2, 46]. That work shows that the cou-

pling between the Orr-Sommerfeld and Squire modes enables very large (i.e., beyond what can be accounted for through the superposition of normal modes), Reynolds number dependent disturbance amplification. The dependence is roughly linear at low Reynolds numbers and cubic at higher Reynolds numbers. The amplification factor for cases 3–5, which all have approximately the same input energy, are respectively $\Gamma_u \approx 680$, $\Gamma_u \approx 2200$, and $\Gamma_u \approx 2920$. These are consistent with the low Reynolds number scaling relationship based on the OSS equations. This makes sense both because the streamwise constant assumption restricts the linear amplification to the $k_x = 0$ modes and because the amplification in the $2D/3C$ model arises from the coupling in (4.3) that is similar to the one in the OSS equations (3.5). In this way computing Γ_u from the simulation of (5.1) represents studying the steady-state nonlinear response to the most amplified $3D$ mode, i.e., the $k_x = 0$ mode. As discussed in Section 3.3.4, the $k_x = 0$ modes provide the most energy growth (in an input-output sense) and represent the dominant mode shapes.

One can similarly investigate an equivalent amplification relationship between the cross-stream velocity components and σ_{noise}, i.e., the output of the ψ equation and compare these to the linear analysis results discussed in Section 3.3.

5.6   Summary

In this chapter, we described the simulation of a $2D/3C$ model (with a linearized ψ evolution equation) under small-amplitude Gaussian forcing of the cross-stream components. We compared both the $2D/3C$ assumptions and the simulation results to a time snapshot of a full spatial field (u, v, w, p) of fully developed turbulent DNS data at $R_w = 3000$.

We reported the results of simulations at three Reynolds numbers and different forcing amplitudes. They demonstrate the ability of this model to capture some aspects of the flow statistics that have been observed in both experiments and numerical studies. In particular, it is demonstrated that (1) the addition of nonlinear terms in the $2D/3C$ model allows us to capture the momentum redistribution involved in creating the shape of the turbulent velocity profile, (2) a stochastically forced $2D/3C$ model can reproduce the appropriate $2D/3C$ turbulent mean velocity profile and Reynolds number trends, and (3) this model produces amplification of small disturbances that is consistent with input-output studies of the LNS. Global stability of the laminar flow in the unforced model points to lack of

robustness as the underlying factor in the transition to a $2D/3C$ "turbulent-like" state.

We explored the refinement of our noise model through the use of two different discretiza-tion schemes. The finite difference method models equal distribution across the wall-normal extent of the flow. A Chebyshev interpolant provided a natural means of introducing more noise at the wall, which, as expected, our results showed to be a more accurate model. In general, the agreement of the model was much better in the center of the channel (the core). This is because the $2D/3C$ model is meant to capture the mean behavior, which means by assumption we filter out some of the small-scale activity. Therefore, the $2D/3C$ assumption is less accurate for the small-scale activity that dominates in the near-wall region.

Chapter 6

Steady-State Equations

In this chapter, we study a steady-state version of the $2D/3C$ model

$$\frac{\partial u'_{sw}}{\partial t} = -\frac{\partial \psi}{\partial z}\frac{\partial u'_{sw}}{\partial y} - \frac{\partial \psi}{\partial z}\frac{\partial U}{\partial y} + \frac{\partial \psi}{\partial y}\frac{\partial u'_{sw}}{\partial z} + \frac{1}{R}\Delta u'_{sw} \tag{6.1a}$$

$$\frac{\partial \Delta \psi}{\partial t} = -\frac{\partial \psi}{\partial z}\frac{\partial \Delta \psi}{\partial y} + \frac{\partial \psi}{\partial y}\frac{\partial \Delta \psi}{\partial z} + \frac{1}{R}\Delta^2 \psi, \tag{6.1b}$$

which was described in Chapter 4. We are interested in forced solutions of the streamwise velocity evolution equation (6.1a) arising through the use of a steady-state stream function $\psi_{ss}(y, z)$ as an input. The resulting fixed point is then the forced solution, i.e., the time-independent (steady-state) streamwise deviation from laminar, which we denote $u'_{sw_{ss}}(y, z)$. This is of interest for two reasons. First, it allows us to determine whether or not this equation filters an appropriately constructed $\psi_{ss}(y, z)$ towards the expected shape of the turbulent velocity profile. It also gives us some insight to the mathematical mechanisms that create the momentum (energy) transfer which generates this "blunted" profile.

We begin by introducing a steady-state stream function model ψ_{ss} model, which is meant to approximate large-scale streamwise elongated structures. The model also represents the first-order term ψ_{ss_1} of a weakly nonlinear expansion, $\psi_{ss} = \psi_{ss_0} + \varepsilon\psi_{ss_1} + \ldots$, where $\psi_{ss_0} = 0$, represents the case of no coupling. In Section 6.2 we numerically solve for $u'_{sw_{ss}}$ and compare the results to the full stochastic simulation discussed in Chapter 5. Then, we look at input-output energy amplification, where the input is the forcing (in the linearized ψ evolution equation (5.1b)) that would generate such a steady-state ψ_{ss} model, and the output is the forced solution, $u'_{sw_{ss}}$. We investigate Reynolds number and amplitude scaling relationships for the steady-state $u'_{sw_{ss}}$ equation. The input-output amplification factor is used to determine the energy optimal spanwise wave number $(k_z = \frac{2\pi}{\lambda_z})$. Reynolds

number and amplitude scaling of this energy amplification are compared with energy growth results in the literature. As in Chapter 5, we compare our results to a full spatial field $(u, v, w, p)(x, y, z)$ of DNS data at $R_w = 3000$ obtained from the Kawamura group [91]. A brief characterization of this data is provided in Section 5.3.

In the final section, we look at a method to determine analytical solutions to a nominal U equation, i.e., the streamwise constant equation (4.1a) for the streamwise velocity u prior to the decomposition into the nominal (laminar) plus the deviation from laminar $u = U_{laminar} + u'_{sw}$, rather than just the deviation from laminar u'_{sw} shown in (6.1b). As before, we are interested in determining the streamwise velocity arising from a stream function representing the large-scale streamwise elongated structures at channel center. In particular, we want to isolate the role of each of the nonlinear terms in creating a "blunted" turbulent velocity profile. We use a (weakly nonlinear) perturbation technique to determine analytical expressions for the first four terms of the nominal streamwise velocity $U = U_0 + \varepsilon U_1 + \varepsilon^2 U_2 + \dots$ arising from a nominal stream function $\Phi = \varepsilon \Phi_1$. We constrain the zeroth-order term to have only wall-normal dependence , i.e., $U_0(y, z) = U_0(y)$, so that it corresponds to the traditional nominal solution of the $2D/3C$ equations. We then use it to verify that the U_0 we obtain is the expected linear profile. The nominal streamwise velocity $U(y, z)$ that we are computing does not represent the time-averaged turbulent velocity profile but rather the steady-state response to a nonzero cross-stream profile, i.e., some nominal wall-normal velocity $V(y, z)$ and spanwise velocity $W(y, z)$. It can be thought of as an instantaneous spatial y–z plane of the flow.

6.1   Stream Function Model

For ease of computation and analysis we were interested in using a simple analytic model for the steady-state stream function $\psi_{ss}(y, z)$, both because this leads to computational tractability and because a simple model better lends itself to analytical studies. In Barkley and Tuckerman [5] it was shown that laminar-turbulent flow patterns in plane Couette flow could be reproduced using a stream function of the form $\psi(y, z) = \psi_0(y) + \psi_1(y) \cos(k_z z) + \psi_2(y) \sin(k_z z)$. We use this study as guidance but set the zeroth-order term ψ_0 to zero because a nonzero ψ_0 produces a nonzero-mean spanwise flow w'_{ss}, which is not representative of the velocity field we are interested in studying. Our primary interest concerns the effect

of large-scale streamwise elongated features in the core of a fully turbulent flow. The DNS field discussed in Section 5.3 was also used as a guide to ensure that the first-order term ψ_{ss_1} as well as the corresponding wall-normal and spanwise velocities, respectively v'_{ss_1} and w'_{ss_1}, have the correct features, see Figure 6.1. A harmonic function $\psi_1(y)$ that satisfies the wall-normal no-slip boundary conditions on v'_{ss_1} and w'_{ss_1} was selected. The full model is

$$\psi_{ss} = \varepsilon \psi_{ss_1}(y,z) = \varepsilon \sin^2(q\pi y) \cos\left(\frac{2\pi}{\lambda_z}z\right). \tag{6.2}$$

The ψ_{ss_1} term corresponds to wall-normal and spanwise velocities, respectively $v'_{ss_1} = \frac{\partial \psi_{ss_1}}{\partial z}$ $w'_{ss_1} = -\frac{\partial \psi_{ss_1}}{\partial y}$, defined as

$$v'_{ss_1}(y,z) = -\frac{2\pi}{\lambda_z} \sin^2(q\pi y) \sin\left(\frac{2\pi}{\lambda_z}z\right), \text{ and } w'_{ss_1}(y,z) = -q\pi \sin(2q\pi y) \cos\left(\frac{2\pi}{\lambda_z}z\right).$$

We treat ε (the size of the perturbation) as a free variable. For our initial studies we set $q = 1$ and fix the spanwise wavelength, λ_z, to a value determined using the DNS data. Later in Section 6.3, we search for the energy optimal λ_z. We examine other q values (wall-normal harmonics) as well as summations over q in Section 6.4.

Figure 6.1(c) and 6.1(e) show x-averages of $v(x,y,z)$ and $w(x,y,z)$ from the DNS data beside the corresponding v'_{ss_1} and w'_{ss_1} estimates from the stream function model ψ_{ss} (in Figure 6.1(d) and 6.1(f) respectively). Integration of $v'_{x_{ave}}(x,y,z)$ and $w'_{x_{ave}}(x,y,z)$ permits an estimate of $\psi_{ss}(y,z)$ (to within some constant) for that particular field. A contour plot of the approximation based on $w'_{x_{ave}}(y,z)$ is shown in Figure 6.1(a).

We selected an initial perturbation amplitude of $\varepsilon = 0.00675$ for our model (6.2) based on the approximate values obtained by integrating $v'_{ave}(y,z)$ and $w'_{ave}(y,z)$. This estimated amplitude is very small compared to the magnitude of the streamwise velocity deviation from laminar u'_{sw} computed through the simulation of Chapter 5. This supports the notion that a nominal model plus an uncertainty is amplified through the coupling from ψ to u'_{sw} in the $2D/3C$ linear operator (4.3). The mechanism of this amplification is described and quantified in studies such as [2,90] and [46]. An initial wavelength of $\lambda_z \approx 1.8$ was chosen to match the results from an FFT of the DNS data (across the z direction) while maintaining the DNS box size ($12.8h$). A contour plot reflecting both these parameter values is provided in Figure 6.1(b). It shows good qualitative agreement with the integrated DNS data, in

(a) $\psi_{x_{ave}}$ estimated from $w'_{x_{ave}}$

(b) $\psi_{ss}(y,z) = 0.00675 \sin^2(\pi y) \cos\left(\frac{2\pi}{1.8}z\right)$

(c) $v'_{x_{ave}}$ from DNS

(d) $v'_{ss}(y,z)$

(e) $w'_{x_{ave}}$ from DNS

(f) $w'_{ss}(y,z)$
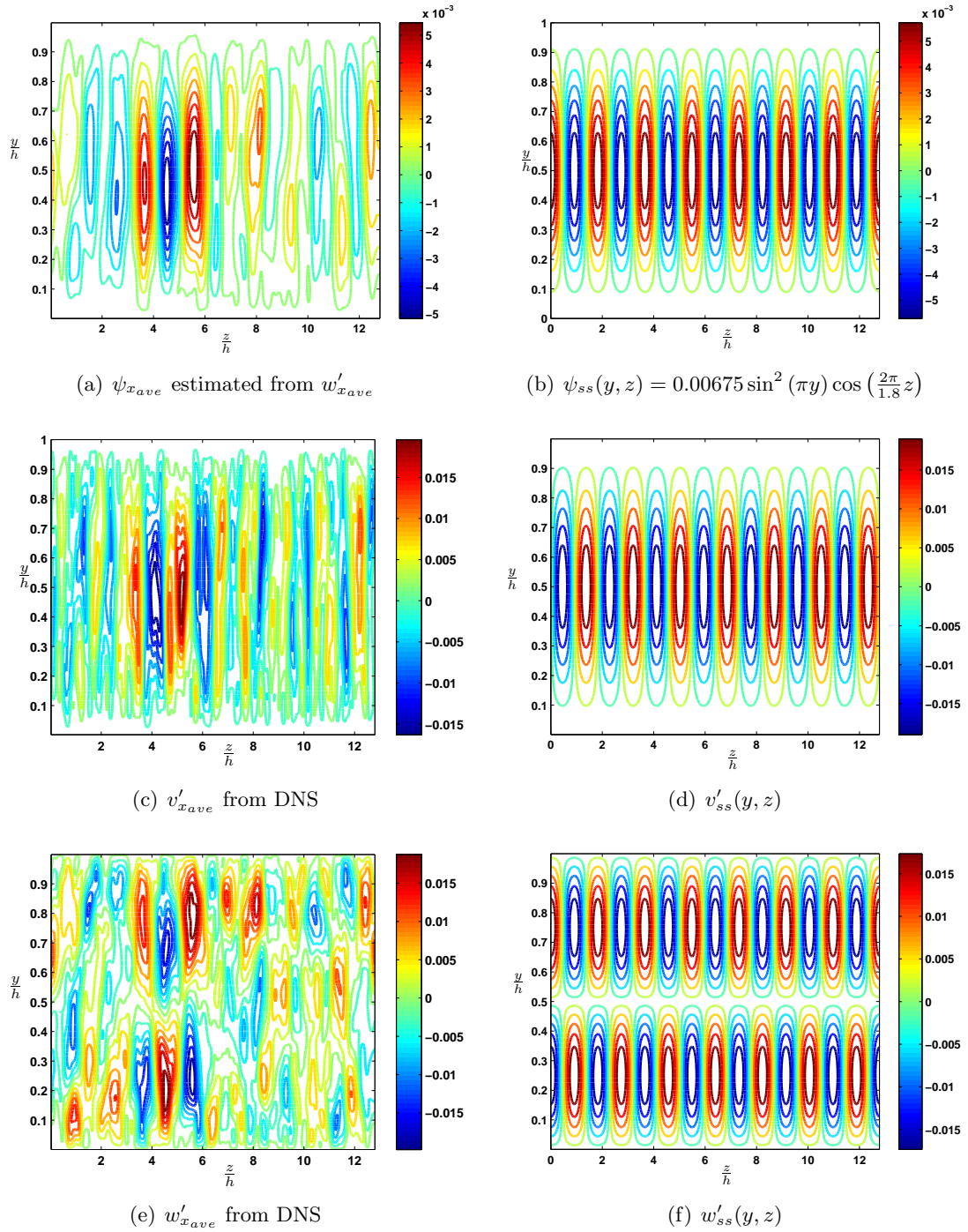
Figure 6.1: (a) Contour plots of $\psi_{x_{ave}}(y,z)$ based on the x-averaged spanwise DNS velocity field, which was integrated to obtain the stream function, i.e., $\psi_{x_{ave}}(y,z) = -\frac{\partial w'_{x_{ave}}}{\partial y}$. (b) The simple harmonic model for $\psi_{ss}(y,z) = 0.00675 \sin^2(\pi y) \cos\left(\frac{2\pi}{1.8}z\right)$ with amplitude and wavelengths that approximate DNS data. Panels (c)–(e) are the x-averaged wall-normal and spanwise velocities from DNS (respectively $v'_{x_{ave}}$ and $w'_{x_{ave}}$). Panels (d)–(f) are the steady-state estimate for $v'_{ss}(y,z)$ and $w'_{ss}(y,z)$ based on ψ_{ss} with the same parameter values as in (b). All data corresponds to $R_w = 3000$.

particular with the region of strongest signal in Figure 6.1(a). It is also consistent with the ψ snapshots from the full pseudospectral stochastic simulations in Figure 5.11, although the wavelength is different as discussed in Section 5.4.1. The vector field corresponding to ψ_{ss} in (6.2) is consistent with low-speed fluid being lifted up from the stationary wall and higher speed fluid being pushed down from the moving wall. Although in reality, the wall-normal variation is complicated (and Reynolds number dependent), Figure 6.1 shows that a simple harmonic variation gives a reasonable representation. The agreement of the ψ_{ss} model with the DNS fields and the instantaneous snapshots from the full stochastic simulation indicate that it may be possible to capture the mechanisms of interest (particularly the momentum transfer) using a single harmonic in both y and z.

6.2 Forced Streamwise Velocity

In this section we use the stream function model in (6.2) as input to a steady-state streamwise velocity equation and discuss the resulting forced solution, $u'_{sw_{ss}}(y, z)$. We describe how both this output velocity, $u'_{sw_{ss}}$, as well as the forcing required to produce ψ_{ss} scale with Reynolds number R and ψ_{ss} amplitude ε. Although scaling relationships are developed for general R, we use the form $R_w = \frac{U_w h}{\nu}$ as defined in Figure 5.1 for all computations.

The steady-state version of the streamwise velocity evolution equation (6.1a) is

$$\left(-\frac{\partial \psi_{ss}}{\partial z} \frac{\partial}{\partial y} + \frac{\partial \psi_{ss}}{\partial y} \frac{\partial}{\partial z} + \frac{1}{R_w} \Delta \right) u'_{sw_{ss}} = \frac{\partial \psi_{ss}}{\partial z} \frac{\partial U}{\partial y}. \tag{6.3}$$

For the results presented in this section we first solved (6.3) for $u'_{sw_{ss}}(y, z)$ using both a least-squares solution and iteratively using the same resolution as the DNS described in Section 5.3, which has a 96×512 grid on the y–z plane. We also tried a smaller grid of 48×100 and found negligible differences in the results. In the sequel, we only report the results for the 48×100 grid.

A contour plot of the $u'_{sw_{ss}}(y, z)$ resulting from our computations at $R_w = 3000$, with the stream function ψ_{ss} model (6.2) parameters set to $\varepsilon = 0.00675$ and $\lambda_z = 1.8$, is depicted in Figure 6.2(a). This figure shows that the steady-state streamwise velocity deviation from laminar $u'_{sw_{ss}}(y, z)$ has near-wall rolls that are out of spanwise phase with one another similar to those seen in both $u'_{x_{ave}}$ from the x-averaged DNS data and $\overline{u'_{sw}}$ from the
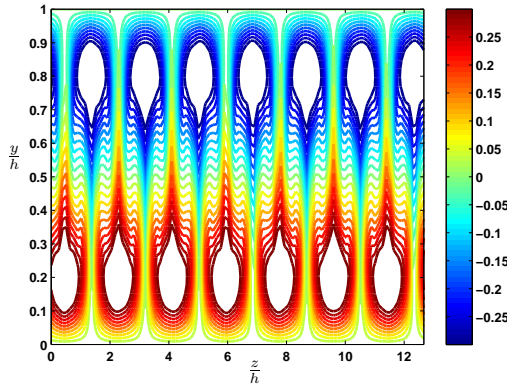
(a) $u'_{sw_{ss}}$ from ψ_{ss} in Equation (6.3)
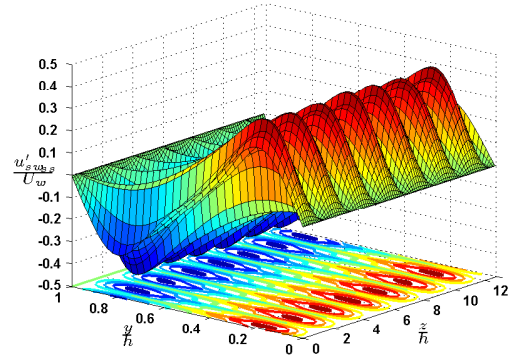
(b) $u'_{sw_{ss}}$ from ψ_{ss} in Equation. (6.3)
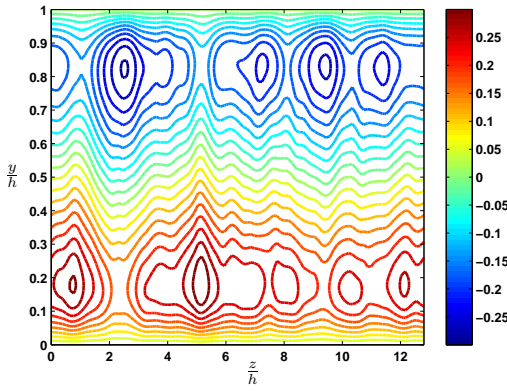
(c) $\overline{\dfrac{u'_{sw}}{U_w}}$ from Case 1 in Table 5.2
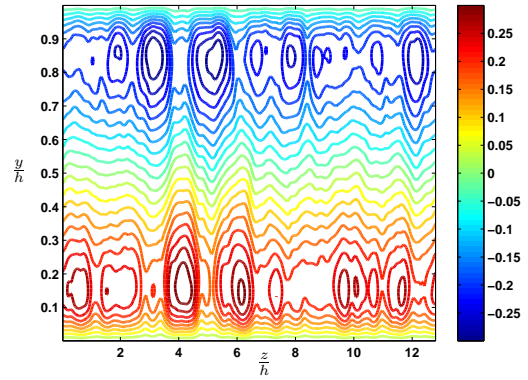
(d) $\dfrac{u'_{x_{ave}}}{U_w}$ from DNS Data
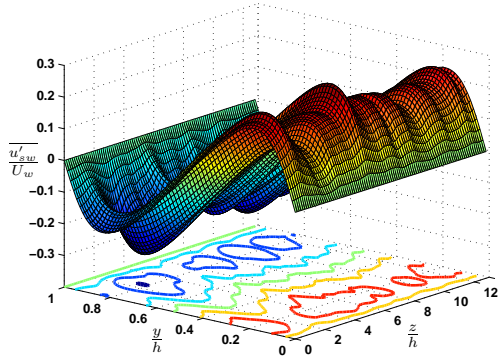
(e) $\dfrac{u'_{sw}}{U_w}$ from Case 1 in Table 5.2
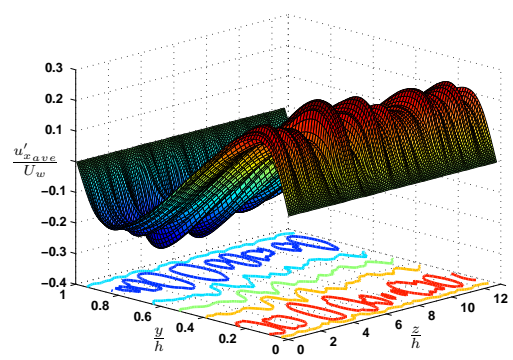
(f) $\dfrac{u'_{x_{ave}}}{U_w}$ from DNS Data

Figure 6.2: (a) Contour and (b) surface plots of $u'_{sw_{ss}}$, from $\psi_{ss}(y,z) = 0.00675\sin^2(\pi y)\cos\left(\frac{2\pi}{1.82}z\right)$. Panels (c)–(e) are Figures 5.6(a) and 5.6(b) from Chapter 5. Panels (e) and (f) are Figure 5.7 from Chapter 5. Note the z–scale difference between (b) and those from the simulation in Chapter 5 (e) and DNS data (f). All plots correspond to $R_w = 3000$ and all contour plots have the same contour levels.

stochastically forced simulation discussed in Chapter 5 (and shown in Figure 6.2(d) and 6.2(c) respectively with the same contour levels as 6.2(a)). There is more variation in the deviation from laminar (amplitude of the surface) across the span as compared to the DNS data and the full stochastic simulation. This is especially clear in comparing the surface plot of Figure 6.2(b) with those of Figure 6.2(e) and 6.2(f) particularly in the center of the channel. There is also a difference in the amplitude of this $u'_{sw_{ss}}$ versus $u'_{x_{ave}}$, which is readily apparent in the different z-axis scales of the plots (respectively in Figure 6.2(b) and 6.2(e)). In general, the surface plot of $\overline{u'_{sw}}$ in Figure 6.2(e) from the full simulation shows much better agreement with the x-averaged DNS data, Figure 6.2(f). This is partly due to the fact that the stochastic forcing excites all modes and creates stochastic (i.e., less coherent) ψ and u'_{sw} functions. It is also a result of looking at the time-dependent evolution of the flow state rather than the steady-state solution considered here. A steady-state model with only one wall-normal and spanwise mode cannot be expected to capture all of the interactions involved in determining the exact shape or all of the features of the turbulent velocity profile. Clearly the full turbulent field is neither streamwise constant nor steady-state.

The results in Figure 6.2(a) and 6.2(b) obtained using this simple stream function model ψ_{ss} indicate that the nonlinear interaction between cross-stream flow features plays an important role in redistributing energy in the flow field. It is interesting to see that we are getting an increase in the streamwise velocity gradient at the wall using input forcing that represents structures that do not model any of the features in the near-wall cycle. This supports the idea that large-scale structures modulate near-wall activity.

We further investigate the effective energy redistribution through the forced streamwise velocity deviations by comparing the mean deviation from laminar from DNS to the $u'_{sw_{ss}}$ resulting from the ψ_{ss} model (6.2). We make the comparison for five perturbation amplitudes ($0.000675 \leq \varepsilon \leq 0.02$), all at $R_w = 3000$. Averages across the span of $u'_{sw_{ss}}(y, z)$ for these five ε values are compared to a similar average of $u'_{x_{ave}}$ from the DNS in Figure 6.3(a). This figure shows that using ψ_{ss} from (6.2) as an input to (6.3) produces streamwise velocity profiles whose shapes are consistent with $u'_{x_{ave}} \approx \overline{u - U}$ from the DNS. However, the peaks are located at different wall-normal positions. An amplitude that exactly matched both the magnitude and location of the DNS peaks was not found even when different values of wavelengths λ_z were studied. This is not unexpected because of the simplicity of the

(a) Perturbation Amplitude Variation

(b) Velocity Gradient at the Wall
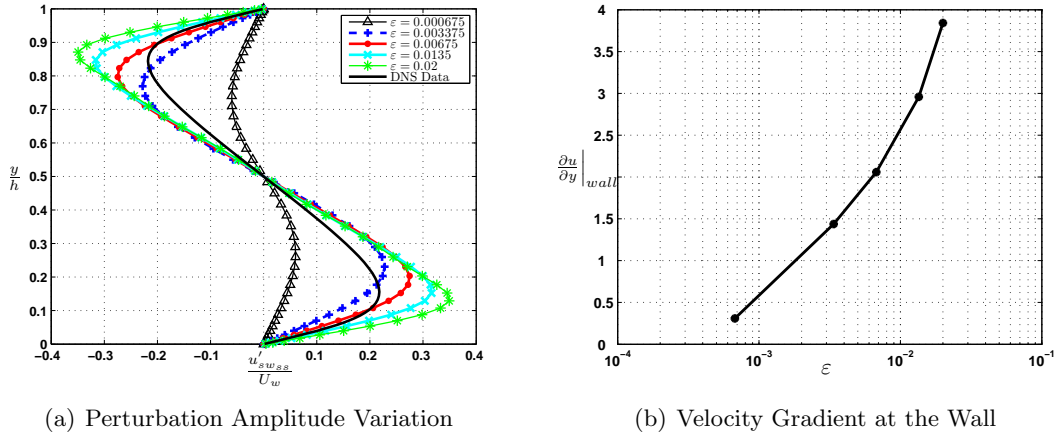
Figure 6.3: (a) Variation of the $2D/3C$ (streamwise constant) velocity deviations, $u'_{sw_{ss}}$ with perturbation amplitude (ε); estimates are obtained using $\psi_{ss}(y,z) = \varepsilon \sin^2(\pi y) \cos\left(\frac{2\pi}{1.82}z\right)$ (b) Variation in the velocity gradient at the wall $\left.\frac{\partial u}{\partial y}\right|_{wall}$ with perturbation amplitude, ε.

wall-normal variation in the steady-state model, as well as the streamwise constant and steady-state assumptions. In Section 6.4 we will discuss how adding more y modes can be used to improve agreement between the forced solutions of the ψ_{ss} model (6.2) and the DNS data.

The magnitude of forcing applied to the system is reflected in the amplitude of $\psi_{ss}(y, z)$, which in turn affects velocity gradient at the wall (i.e., the amount of blunting in $u_{sw_{ss}}$). Figure 5.9 from the simulation studies discussed in Chapter 5 showed that increasing Reynolds number (while noise forcing is held constant) also causes increased velocity gradients at the wall and a more "blunted" profile. A higher amplitude (ε) in (6.2) corresponds to higher amplitude forcing of the ψ evolution equation. This is analogous to increasing the magnitude of the model uncertainty. It would have an effect similar to that of a "noisier" experiment and thus corresponds to an increase in the shear stress at the wall (i.e., a larger friction Reynolds number R_τ) and a larger peak value for $u'_{sw_{ss}}$. These effects are seen in Figure 6.3(a) (recall that the variables are normalized by h and U_w rather than u_τ). The trend is even more clear in Figure 6.3(b), which provides a plot of ε versus the velocity gradient at the wall, $\left.\frac{\partial u}{\partial y}\right|_{wall}$.

The simple steady-state model (6.14) forced by ψ_{ss} reasonably predicts the essence of the mean behavior at the expense of losing some of the smaller scale details. For example, the spanwise variation, exact characterization of the wall-normal variation activity and,

of course, the small-scale turbulent velocity fluctuations are not captured in this analysis. These results suggest that the phenomenon that is responsible for blunting of the velocity profile in the mean sense is a direct consequence of the interaction between rolling motions caused by the y–z stream function and the laminar profile. In other words, this study provides strong evidence that the nonlinearity needed to generate the turbulent velocity profile comes from the nonlinear terms that are present in the $u'_{sw}(y, z, t)$ evolution equation (6.1a).

6.2.1 Scaling Relationships

In this subsection we investigate both Reynolds number R_w and amplitude ε scaling of the steady-state streamwise velocity equation (6.3). We first investigate the relationship between R_w and ε and then focus on determining an R_w-independent steady-state streamwise velocity equation.

In order to illustrate the effect of the amplitude ε, we rewrite (6.3) with ψ_{ss} replaced by $\varepsilon\psi_{ss_1}$ in the form

$$\left(-\frac{\partial \psi_{ss_1}}{\partial z} \frac{\partial}{\partial y} + \frac{\partial \psi_{ss_1}}{\partial y} \frac{\partial}{\partial z} + \frac{\Delta}{\varepsilon R_w} \right) u'_{sw_{ss}} = \frac{\partial \psi_{ss_1}}{\partial z} \frac{\partial U}{\partial y}. \tag{6.4}$$

Equation (6.4) indicates that R_w is closely related to ε. An increase in ε with a constant R_w has the same effect as increasing R_w at a single ε. More precisely, $u'_{sw_{ss}}$ does not vary if εR_w is constant. This close relationship between R_w and ε is consistent with Figure 6.3(a) and 6.3(b), which show that an increase in ε corresponds to an increase in the peak amplitude of $u'_{sw_{ss}}$ as well as larger velocity gradients at the wall, which is precisely the behavior we expect from an increase in R_w.

In order to relate our discussion to the type of input-output scaling previously described, it is useful to determine the forcing required to produce a steady-state ψ_{ss}. This is accomplished by solving a forced version of the steady-state ψ evolution equation (6.1b) to obtain

$$\Upsilon_{ss}(y, z) = \frac{\partial \psi_{ss}}{\partial z} \frac{\partial \Delta \psi_{ss}}{\partial y} - \frac{\partial \psi_{ss}}{\partial y} \frac{\partial \Delta \psi_{ss}}{\partial z} - \frac{1}{R_w} \Delta^2 \psi_{ss}. \tag{6.5}$$

The linearized version of this forcing equation, which by abuse of notation we also denote

$\Upsilon_{ss}(y, z)$, is

$$\Upsilon_{ss}(y, z) = -\frac{1}{R_w}\Delta^2\psi_{ss}. \tag{6.6}$$

Υ_{ss} is the deterministic forcing required to produce a particular ψ_{ss}.

To isolate the effect of R_w we introduce the change of variables

$$\Psi = R_w\psi_{ss}, \tag{6.7}$$

this results in the R_w independent steady-state streamwise velocity equation

$$\frac{\partial\Psi}{\partial z}\frac{\partial U}{\partial y} = \left[-\frac{\partial\Psi}{\partial z}\frac{\partial}{\partial y} + \frac{\partial\Psi}{\partial y}\frac{\partial}{\partial z} + \Delta\right]\tilde{u}'_{sw_{ss}}, \tag{6.8}$$

where we use $\tilde{u}'_{sw_{ss}}(y, z, \Psi)$ to indicate that the dependence on $\Psi = R_w\psi_{ss}$ rather than ψ_{ss}. The R_w independent $\tilde{u}'_{sw_{ss}}$ equation can also be written in terms of $\Psi_1 = \frac{\Psi}{\varepsilon}$ to explicitly show the amplitude dependence

$$\frac{\partial\Psi_1}{\partial z}\frac{\partial U}{\partial y} = \left[-\frac{\partial\Psi_1}{\partial z}\frac{\partial}{\partial y} + \frac{\partial\Psi_1}{\partial y}\frac{\partial}{\partial z} + \frac{1}{\varepsilon}\Delta\right]\tilde{u}'_{sw_{ss}}. \tag{6.9}$$

The linearized forcing in terms of Ψ_1 can be also be computed. Application of the change of variables (6.7) to the linear forcing equation (6.6) gives

$$\eta_{ss}(y, z) = -\frac{\varepsilon}{R_w^2}\Delta^2\Psi_1. \tag{6.10}$$

Although the streamwise velocity deviations can be normalized such that they are independent of R_w, the forcing cannot. The linearized forcing (η_{ss} or Υ_{ss}) is obviously proportional to ε. In the transformed coordinates (i.e., for Ψ_1), the forcing is inversely proportional to R_w^2. In the next section, we will use these scaling relationships to determine an input-output energy scaling analogous to the one discussed in Section 4.4. In the sequel, we use the linear Υ_{ss} of Equation (6.6) for all of the computations. For a complete discussion of the use of a linear ψ equation see [29] and Section 5.4.5.

(a) Energy Scaling (b) Reynolds Number Trends
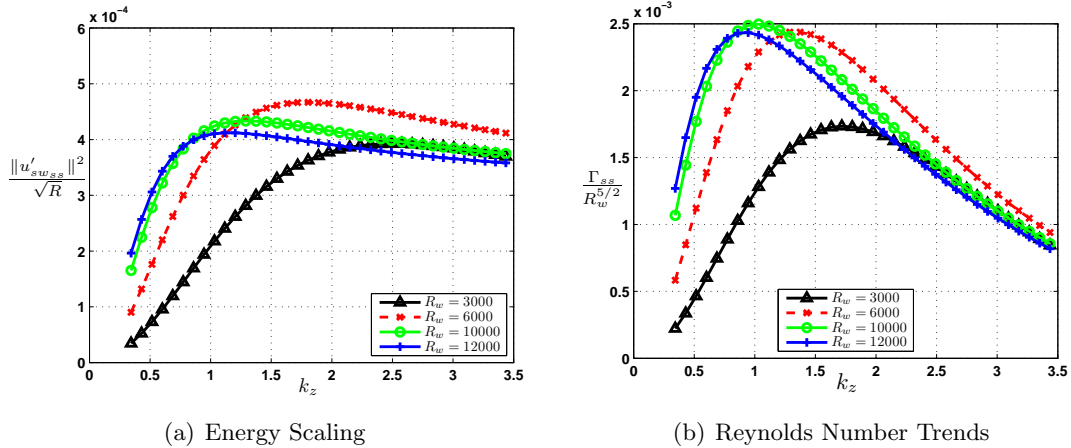
Figure 6.4: (a) The streamwise energy scales as $\sqrt{R_w}$. (b) The amplification factor Γ_{ss} scales as $R^{\frac{5}{2}}$. The optimal spanwise wave number occurs at the maximum Γ_{ss} for each R_w.

6.3 Energy Amplification

In this section we study an energy response of (6.3) as ε and R_w are varied. For ease of notation we perform this study in terms of the spanwise wave number $k_z = \frac{2\pi}{\lambda_z}$. As in Chapter 5, we use the Reynolds number defined by $R_w := \frac{U_w h}{\nu}$ described in Figure 5.1 for all computations. We also increase our y–z grid size to 48×128 and perform the calculations over a spanwise extent of $2\lambda_z$.

The input-output energy response can be studied through a steady-state amplification factor

$$\Gamma_{ss} = \frac{\left\| u'_{sw_{ss}} \right\|^2}{\left\| \Upsilon_{ss} \right\|^2}. \tag{6.11}$$

Γ_{ss} is an analog of the L_2–to–L_2 induced norm (defined in Chapter 2, Definition 2.4.3) that has been used to study the optimal response of the system to harmonic forcing, see for example [79]. In the frequency domain this again corresponds to an $\mathcal{H}_\infty$ type norm.

The scaling of $u'_{sw_{ss}}$ with R_w for a particular ε is unclear from Equation (6.4). In order to determine an empirical relationship we computed $\|u'_{sw_{ss}}\|^2$ using the stream function model (6.2) with $q = 1$ and $\varepsilon = 0.001$ for four different values of R_w: 3000, 6000, 10000 and 12000. Figure 6.4(a) shows that for the R_w values selected $\|u'_{sw_{ss}}\|^2$ scales as a function of $\sqrt{R}$. If we combine this $\sqrt{R}$ scaling of $\|u'_{sw_{ss}}\|^2$ with the $\frac{1}{R}$ scaling of $\Upsilon_{ss}(y, z)$, then Γ_{ss} should scale as a function of $R^{\frac{5}{2}}$. This is less than the function of R^3 energy scaling of the full $2D/3C$ model described in Section 4.4. The scaling of the input-output amplification

for streamwise constant disturbances of the linearized Navier Stokes (LNS) equations can be expressed as $f_1(k_z)R + f_2(k_z)R^3$, where the magnitude of the function $f_1(k_z)$ is O(0.1) for all parallel flows [2]. The magnitude of $f_2(k_z)$ for Couette flow is O(10^{-4}) [2]. Therefore, at lower Reynolds numbers the linear term would dominate. Another low Reynolds number linear study of Poiseuille flow showed energy amplification at $k_x = 0$ scales with $R^{\frac{3}{2}}$ for the range $800 \leq R \leq 5000$ and R^3 for larger Reynolds numbers [26]. In that study, R was normalized on half channel height δ, the equivalent normalization would make our Reynolds number range $750 \leq R_c \leq 3000$. Based on both of these earlier results the fact that our scaling is less than R^3 is not unreasonable due to the low Reynolds numbers we are employing.

Figure 6.4(b) shows $\frac{\Gamma_{ss}}{R^{5/2}}$ for $R_w = 12000, 10000, 6000$ and 3000 all with $\varepsilon = 0.001$. The data collapses well under the $R^{5/2}$ scaling, especially at the higher wave numbers. As previously discussed, at low Reynolds number the scaling relationship is dominated by the $f_1(k_z)R$ term. Thus, the lower Γ_{ss} peak value at $R_w = 3000$ (corresponding to $R_c = 750$) is plausible. Optimal amplification studies based on initial conditions also support R_w scaling at low Reynolds numbers [26].

Figure 6.4(a) indicates that $\|u'_{sw_{ss}}\|^2$ increases with k_z until it reaches a maximum value and then levels off. We can similarly find a relationship between k_z and Υ_{ss} by substituting the expression for ψ_{ss} from (6.2) into the linearized noise equation (6.6). This yields

$$\Upsilon_{ss}(y,z) = -\frac{\varepsilon}{R_w} \left\{ \left[\left(k_z^2 + 4q^2\pi^2 \right)^2 - 4q^2 k_z^2 \pi^2 \right] \sin^2(q\pi y) \cos(k_z z) \right. \\ \left. - \left(8q^4\pi^4 + 2q^2 k_z^2 \pi^2 \right) \cos(k_z z) \right\}, \tag{6.12}$$

which is proportional to both k_z^4 and q^4. So, the forcing energy $\|\Upsilon_{ss}\|^2$ is monotonically increasing with k_z while $\|u'_{sw_{ss}}\|^2$ peaks and then levels off. This means that even though larger k_z is associated with higher forcing the corresponding amplification factor does not continue to increase. There is some optimal k_z that generates the most amplification: This is the dominant wave number corresponding to optimal spanwise spacing.

6.3.1 Optimal Spanwise Spacing

In this section we determine the optimal spanwise wave number for a constant ε at different Reynolds numbers. We compare these results to the optimal very-large-scale motion

(VLSM) and streak spacings reported in the literature.

The optimal spanwise spacing occurs where Γ_{ss} is maximized. The peak values of Γ_{ss} for the Reynolds numbers considered in Figure 6.4(b) correspond to spanwise wave numbers of $k_z = 0.86$, 1.0, 1.4 and 1.7; for $R_w = 12000$, 10000, 6000 and 3000 respectively. This amounts to wavelengths of $7.3h$, $6.1h$, $4.6h$ and $3.7h$, which are related to the full channel height h. Much of the literature, e.g., $[10, 25, 33]$, related to optimal spanwise spacing has shown $k_z \in [2.8, 4]h$. The discrepancy is likely because their values correspond to the small-scale near-wall streamwise streaks whereas our stream function represents channel spanning structures associated with large-scale flow behavior.

Recent Poiseuille flow studies using the LNS linearized about a turbulent velocity profile, where an eddy viscosity is used to maintain the profile, found that at high Reynolds numbers there are two peaks in the optimal energy growth curves, one scaling in inner units and the other in outer units $[13, 71]$. The outer unit peak appears to correspond to the large-scale structures (VLSMs) that have a spanwise spacing of approximately $\lambda_z \in [2, 5.2]\delta$. Our structures are still slightly larger. However, they are in line with the only Couette flow study to look at both inner and outer unit scalings $[41]$. In this paper, the authors reported results at $R_w = 3000$ for different types of forcing and found that the optimal response to harmonic forcing occurs when $\lambda_z = 3.85h$. Harmonic forcing is more closely related to our analysis than the initial condition-based studies reported in most of the other work. For the Reynolds numbers considered here and in $[41]$ there is no scale separation between the peaks.

6.3.2 Amplitude Variation

In this section we study the variation of Γ_{ss} with amplitude ε while the Reynolds number is held constant at $R_w = 3000$. We consider smaller amplitudes than those employed in Section 6.2 based on Figure 6.3(a), which showed a peak amplitude significantly higher than that of the DNS data for $\varepsilon \geq 0.00675$.

Figure 6.5(a) shows Γ_{ss} for an amplitude range of $0.000675 \leq \varepsilon \leq 0.005$. Both Γ_{ss} and the optimal spanwise wave number monotonically decrease with ε. There appears to be a collapse at the minimal wavelengths. The optimal wavelengths for the lower amplitudes, $\varepsilon \in [0.0005, 0.003375]$, are between $\lambda_z = 3.2h$ and $\lambda_z 6.1h$. As previously discussed, this is in the range of the wavelengths associated with the Couette flow VLSMs in the literature,

(a) Forcing Amplitude Trends.

(b) Mean Velocity at Maximum Γ_{ss}
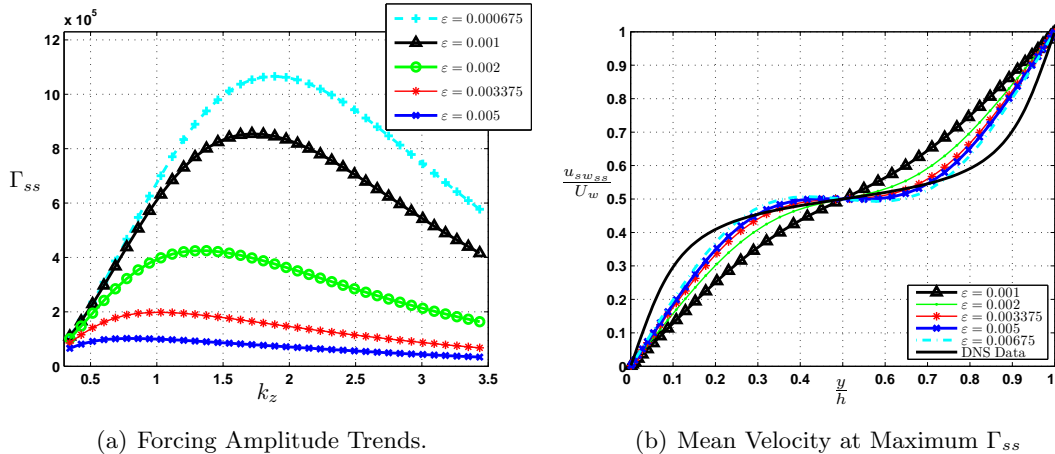
Figure 6.5: (a) Γ_{ss} for different values of ε all at $R_w = 3000$. Both Γ_{ss} and the optimal spanwise wave number monotonically decrease with ε. (b) Mean velocity profiles $u_{sw_{ss}}$ at the optimal k_z for each ε considered in (a). The velocity gradient at the wall increases with ε.

e.g. [50, 52]. On the other hand, the highest amplitude cases, $\varepsilon = 0.005$ and $\varepsilon = 0.00675$ respectively, correspond to $\lambda_z = 8$ and $\lambda_z = 9.1$, which are longer wavelengths than one would expect. They are also much higher than the DNS spanwise wavelength ($\lambda_z = 1.8$) that we used for testing the ψ_{ss} model (6.2) in Section 6.2. However, since the peak Γ_{ss} over all the amplitudes occurs at the lowest ε the optimal wavelength for our $R_w = 3000$ study is the λ_z at the smallest amplitude. If we continue to reduce ε to 0.00001 the optimal wavelength converges to $\lambda_z = 3$ for $R_w = 3000$, 6000, 10000 and 12000. This value is well within the range of optimal wavelengths reported in the literature [41].

For each amplitude, we are interested in connecting ψ_{ss} at its optimal wave number to its accompanying mean velocity profile, $u_{sw_{ss}}$. Figure 6.5(b) shows the steady-state mean velocity profile computed from (6.3) for ψ_{ss} with an amplitude range of $0.001 \leq \varepsilon \leq 0.00675$ at their corresponding optimal values of k_z along with the $R_w = 3000$ DNS data. While the amplitude of Γ_{ss} is much larger for the minimum amplitude, $\varepsilon = 0.0005$, the resulting velocity profile has larger velocity gradients at the wall for the higher amplitude ψ_{ss} models. As before there is no amplitude that exactly matches the DNS data. The fit is especially bad in the near-wall region, but much better in the center of the channel. As previously discussed, this is because the assumptions inherent in the $2D/3C$ model neglect the smaller scale activity that dominates in the near-wall region. At the highest amplitudes, $\varepsilon = 0.005$ and $\varepsilon = 0.00675$, the velocity profiles are both undershooting the DNS curve at the walls and

(a) Mean Profile for Various k_z

(b) Wall Shear Stress versus Energy
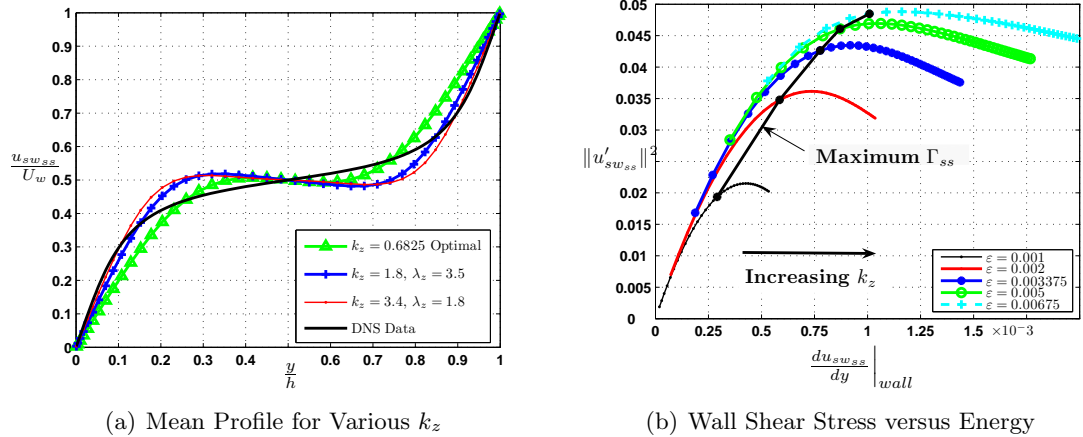
Figure 6.6: (a) The mean velocity profile for $\varepsilon = 0.00675$ at a number of different k_z values compared with DNS data all at $R_w = 3000$. (b) The velocity gradient at the wall continues to increase while both Γ_{ss} and the energy $\|u'_{sw_{ss}}\|^2$ peak and then drop off. The solid black line represents the peak Γ_{ss} for each ε.

overshooting it at channel center. At the optimal k_z, $u_{sw_{ss}}$ from $\varepsilon = 0.005$ and $\varepsilon = 0.00675$ respectively cross the DNS curve at a $y^+ \approx 30$ and $y^+ \approx 27$, based on the DNS viscous units. The maximum overshoot in the core (defined by $y^+ > 30$ in DNS viscous units) is 3.6% and 6.2%, respectively for $\varepsilon = 0.005$ and $\varepsilon = 0.00675$. This is a very good prediction for such a simplified steady-state model. In the next section we look at refining the model to improve the agreement.

Figure 6.6(a) shows the mean velocity profile of the DNS along with mean velocities for $\varepsilon = 0.005$ and $\varepsilon = 0.00675$ at the maximum Γ_{ss} (optimal wave number $k_z = \frac{2\pi}{\lambda_z} = 0.69$), at $k_z = 1.8$ and at $k_z = 3.4$. This last value coincides with $\lambda_z = 1.8$, i.e., the value corresponding to the DNS data [91] and the results discussed in Section 6.2. The larger wave numbers vastly overshoot the DNS curve in the center of the channel but have better agreement near the walls. The continued increase in shear stress at the wall as both k_z and ε increase is better seen in Figure 6.6(b). For all amplitudes $\varepsilon \geq 0.002$ the mean velocity curves overshoot the DNS near the centerline for k_z values above the optimal. This overshoot may indicate that some of the energy is going into pushing the response too high or "over blunting" the profile at the channel center. This is clearly not optimal in creating a $u_{sw_{ss}}$ that corresponds to a "turbulent-like" state. This may indicate that when the forcing amplitude gets too high, the model no longer accurately represents the system behavior.

(a) Low Amplitudes (b) Higher Amplitudes
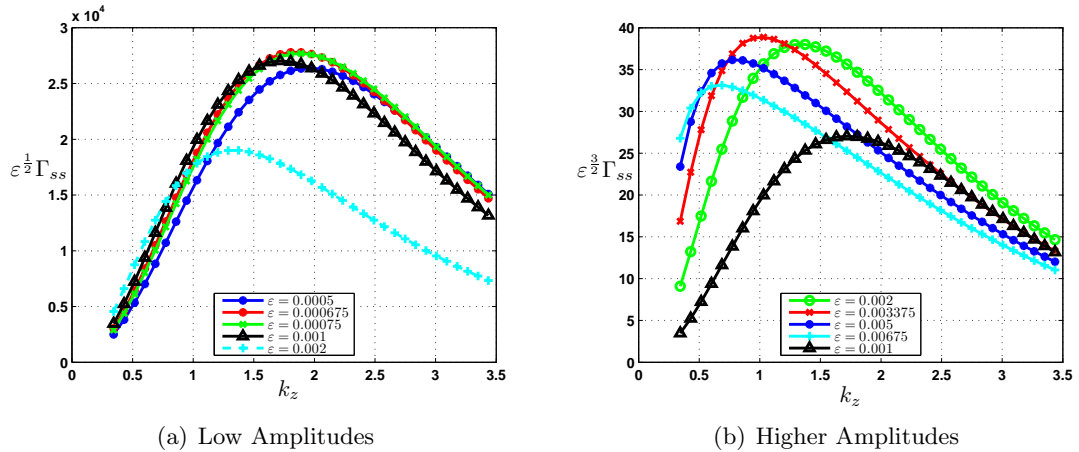
Figure 6.7: (a) For low ε the amplification Γ_{ss} scales with $\frac{1}{\sqrt{\varepsilon}}$ whereas (b) for higher ε, it scales with $\frac{1}{\varepsilon^{\frac{3}{2}}}$.

Finally, we are interested in determining amplitude scaling relationships for Γ_{ss}. Figure 6.7(a) shows that the low-amplitude data $\varepsilon \in [0.0005, 0.001]$ collapses very well with an $\varepsilon^{\frac{1}{2}}$ scaling, especially at low wave numbers. At higher k_z's this scaling does not work for $\varepsilon \geq 0.002$, as indicated by the $\varepsilon = 0.002$ curve in Figure 6.7(a). The higher amplitude data $\varepsilon \in [0.002, 0.00675]$, shown in Figure 6.7(b), collapses with $\varepsilon^{\frac{3}{2}}$. This scaling is best at the higher wave numbers.

If we look again at the scaling relationships in Equation (6.4), $\|u'_{sw_{ss}}\|^2$ should scale with $\varepsilon^{\frac{1}{2}}$, i.e., follow the same scaling as the Reynolds number. The forcing energy $\|\Upsilon_{ss}\|^2$ on the other hand has an inverse scaling between R_w and ε. Therefore, the fact that Γ_{ss} scales with $\frac{1}{\varepsilon^{\frac{1}{2}}}$ is equivalent to it scaling with R_w. Similarly, the $\frac{1}{\varepsilon^{\frac{3}{2}}}$ corresponds to $R_w^{\frac{5}{2}}$ scaling. Again, this is consistent with studies that show that at low Reynolds numbers the energy scales linearly and then as Reynolds number increases the R^3 scaling begins to dominate.

6.4 Model Refinement

The use of a single harmonic in both y and z did not allow us to match the turbulent velocity profile from the DNS data. In this section we look at refining the ψ_{ss} model to see if we can better fit this data. In particular, we study the effect of additional wall-normal harmonics in the stream function model, ψ_{ss} in (6.2). This should also enable us to better evaluate the contribution of near-wall streaks and vortices to the overall amplification.

Figures 6.8(a) and 6.8(b) respectively show the ψ_{ss} model (6.2) for $q = 2$ and $q = 3$. The $q = 2$ case represents two small structures closer to the walls as opposed to the channel spanning feature for $q = 1$, pictured in Figure 6.1(b). At low amplitudes this should be a better model for the near-wall streamwise streaks and vortices that play a key role in determining the velocity gradients and corresponding shear stress at the wall. The $q = 3$ case corresponds to three peaks, two near the walls and one at channel center. In reality the peak at the channel center should be broader and wider than the peaks at the wall and the near-wall peaks should be even closer to the wall. However, as a first estimate this simplified model can be used to understand the effect of a third y harmonic.

Figure 6.8(c) shows Γ_{ss} for $q = 2$ with $\varepsilon \in [0.001, 0.005]$. The overall amplification for a ψ_{ss} (6.2) with $q = 2$ is roughly 3 orders of magnitude smaller than the amplification for $q = 1$. In fact, because $\Upsilon(y, z)$ is proportional to q^4 (as seen in Equation (6.12)), the magnitude of the forcing increases with q. Figure 6.8(e) shows that the streamwise energy that arises from the larger forcing is of similar order of magnitude to the $q = 1$ energy, seen in Figure 6.6(b). So, at each k_z we are getting similar energy for much larger input. This points to reduced energy production for the $q = 2$ case. It is consistent with experimental observations, which indicate that the large-scale structures (in the core) contribute most of the flow energy [39, 65].

At the two lowest amplitudes considered, the optimal wavelength was reduced under the $q = 2$ model. The optimal wavelengths for $\varepsilon = 0.001$ and $\varepsilon = 0.002$ were respectively at $\lambda_z = 2.9h$ and $\lambda_z = 4.1h$ versus the $q = 1$ values of $\lambda_z = 3.7h$ and $4.6h$. This is still higher than the 100 viscous unit spacing typical for the near-wall streaks but the lowest amplitude case is much closer to optimal values $1.9h \leq \lambda_z \leq 2.4h$, (for $k_z \in [2.8, 4]h$) reported in linear studies, e.g. [10, 25]. The Γ_{ss} peak location did not change for the $\varepsilon = 0.003375$ and $\varepsilon = 0.005$ cases. This supports the idea that the lower amplitude models are more representative of the near-wall structures.

Figure 6.8(d) shows that for $q = 3$ with $\varepsilon = 0.003375$ and $\varepsilon = 0.005$, Γ_{ss} is even lower than for the $q = 2$ case. Again, the streamwise energy is significantly smaller even though the q^4 term indicates that $\Upsilon(y, z)$ is larger than that of either the $q = 1$ or $q = 2$ case. Figure 6.8(f) shows that the streamwise energy that arises from the larger forcing is of similar order of magnitude to the $q = 2$ energy in Figure 6.8(e). Again, less energy is produced per unit of forcing.

(a) ψ_{ss} Model for $q = 2$

(b) ψ_{ss} Model for $q = 3$

(c) Γ_{ss} with for ψ_{ss} from (6.2) with $q = 2$

(d) Γ_{ss} with for ψ_{ss} from (6.2) with $q = 3$

(e) $\|u'_{sw_{ss}}\|^2$ for $q = 2$

(f) $\|u'_{sw_{ss}}\|^2$ for $q = 3$
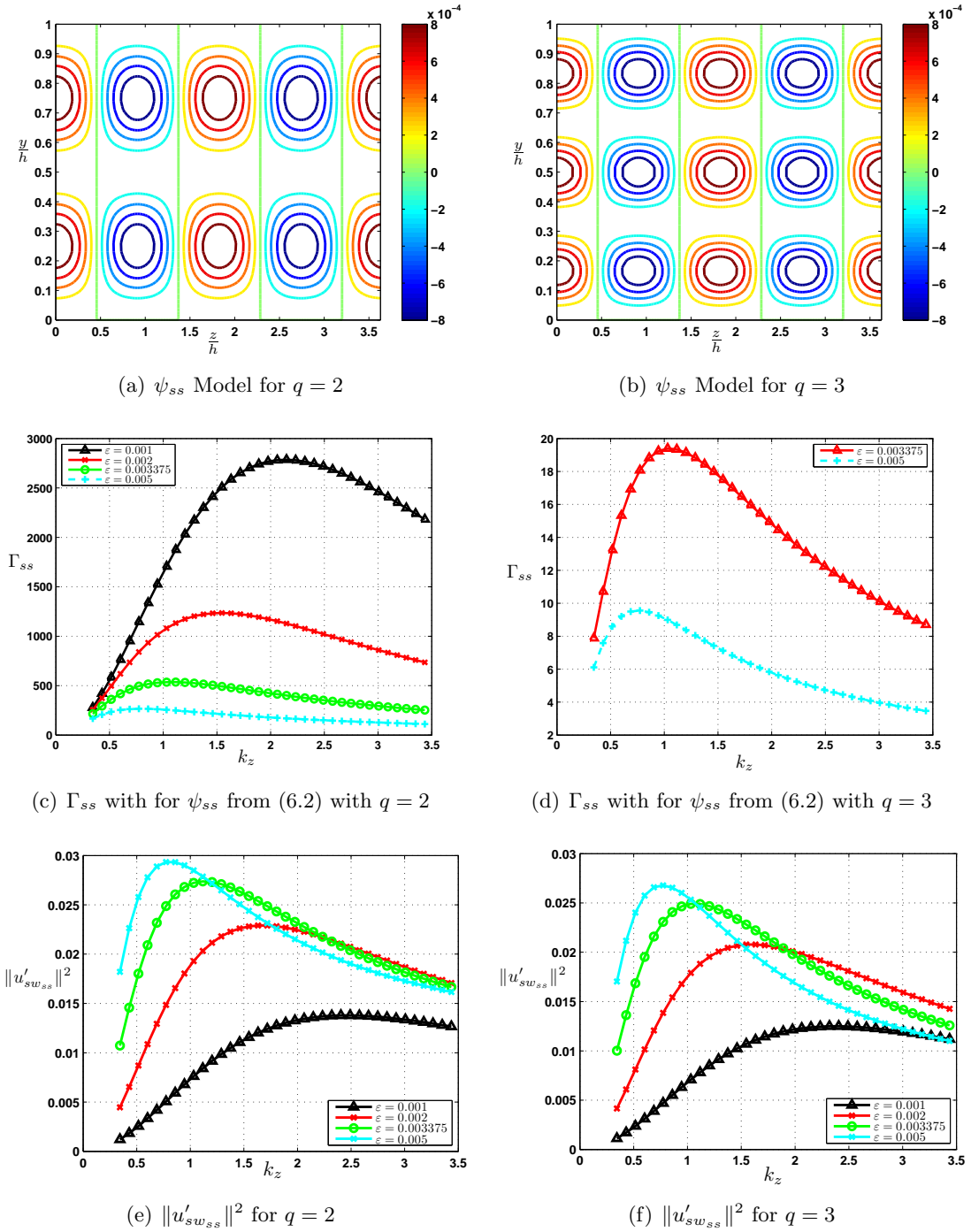
Figure 6.8: Panels (a) and (b) are contour plots of $\psi_{\mathbf{ss}}(y,z) = 0.001 \sin^2(q\pi y)\cos(\frac{2\pi}{1.8}z)$ with $q = 2$ in (a) and $q = 3$ in the second and third y harmonics for the stream function model (6.2). Panels (c) and (d) are the corresponding Γ_{ss} for the ψ_{ss} model in (a) and (b) respectively for different values of ε. The amplification is much smaller for the higher harmonics $q > 1$ even though the forcing is larger by a factor q^4. Panels (d) and (e) are the streamwise energy $\|u'_{sw_{ss}}\|^2$ for the second and third y harmonics $q = 2$ and 3.

The mean velocity profiles corresponding to the ψ_{ss} model (6.2) with $q = 2$ for amplitudes $\varepsilon \in [0.001, 0.005]$ are shown in Figure 6.9(a). In contrast to the $q = 1$ case and the typical turbulent mean velocity, the profiles have double peaks in each half of the channel. In order to better compare the mean velocity profiles corresponding to the ψ_{ss} with the different parameter values for q, the curves for $q = 1$, $q = 2$ and $q = 3$ for $\varepsilon = 0.003375$ and $\varepsilon = 0.005$ are all plotted together in Figure 6.9(b). It appears that the locations where the streamwise velocity $u_{sw_{ss}}$ arising from the stream function model ψ_{ss} (6.2) with $q = 1$ are deviating from the DNS data are the same locations where the velocity $u_{sw_{ss}}$ from (6.2) with $q = 2$ have excursions of the opposite sign. Therefore, a superposition of $u_{sw_{ss}}$ obtained using the first two harmonics may provide a correction for the overshoot in the center of the channel. In the near-wall region the $q = 2$ will also contribute to an increased velocity gradient (shear) at the wall. These changes are exactly what would be prescribed to make the curves better resemble turbulent velocity profiles from the DNS or experimental data.

Figure 6.9(c) provides a comparison of $u_{sw_{ss}}$ obtained from the model with $q = 1$ at the optimal k_z to one obtained by adding the $q = 1$ and $q = 2$ profiles. This clearly improves the fit near the walls but leads to a larger (but of opposite sign) error in the channel center. The mean profile from the third harmonic $q = 3$, also shown in Figure 6.9(b), sits somewhere between the $q = 1$ and $q = 2$ curves. The red curve in Figure 6.9(c) shows that adding this harmonic (at the same, optimal, k_z) to the first two makes the fit near the walls almost perfect and mitigates the undershoot at the channel center. The maximum percentage error in the near-wall region is now 11%, while the maximum percentage error in the channel center is 5.1%. Although we have vastly improved the fit in the near-wall region, the error at the center of the channel is larger than the 3.6% we had with the simple $q = 1$ model.

In reality one would likely use models that have different amplitudes or wave numbers for each of the harmonics. A simple experiment changing the k_z of the third harmonic, shown in Figure 6.9(d), shows that one can improve the fit further by modifying the wave number for the stream function model (6.2) with $q = 3$. The cases where we add a streamwise velocity curve obtained using a model (6.2) with $q = 3$ and $k_z = 0.4295$ or $k_z = 0.5154$ reduce the maximum error in the center of the channel to 2.6%. The maximum near-wall error is 19%. This error is significantly lower than for the $q = 1$ case and Figure 6.9(d) illustrates that 19% error in this region corresponds to a very small absolute distance between curves.
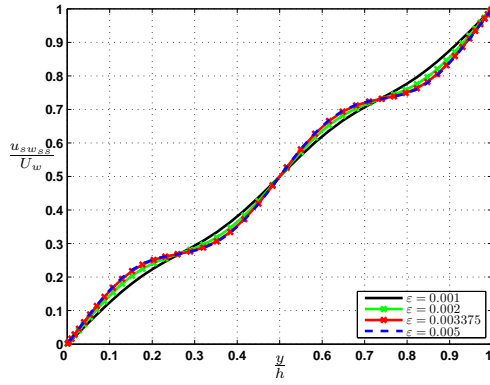
(a) Mean Velocity Profiles for $q = 2$
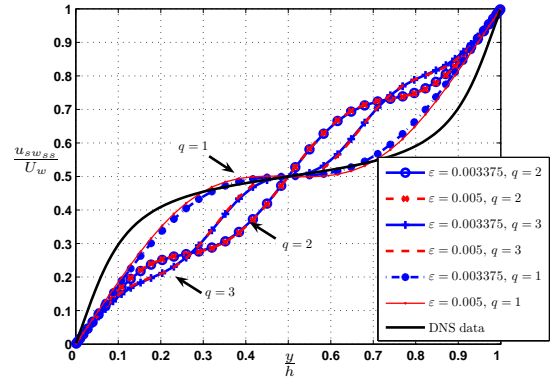
(b) Mean Velocity Profiles for $q = 1, 2$ and 3
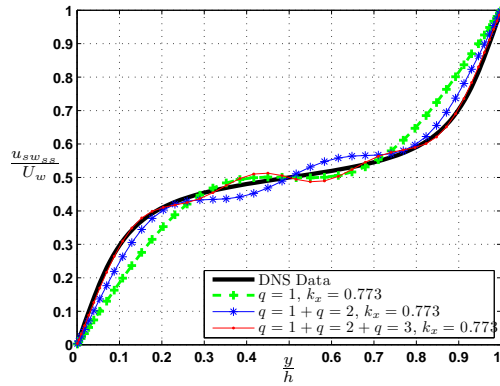
(c) All Harmonics with same $k_z = 0.773$
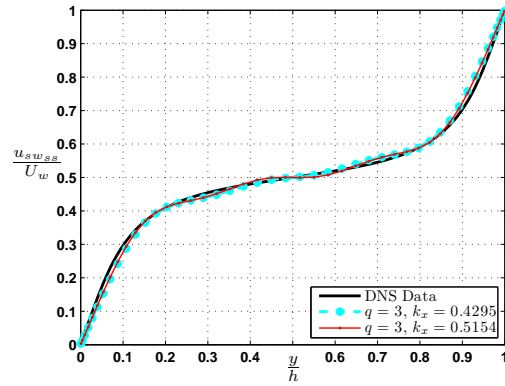
(d) $k_z = 0.773$ for $q = 1$ and $q = 2$ and two different k_z for $q = 3$

Figure 6.9: (a) Mean velocity profiles at the maximum Γ_{ss} for $q = 2$, $\varepsilon \in [0.001, 0.005]$ (b) Mean velocity profiles at the maximum Γ_{ss} for $q = 1, 2$ and 3 for $\varepsilon = 0.003375$ and $\varepsilon = 0.005$. (c)Adding the $q = 1$, $q = 2$ and $q = 3$ wall-normal harmonics at the optimal $k_z = 0.773$ for $\varepsilon = 0.005$. (d) Using a different k_z for $q = 3$, this improves the fit to DNS data.

Further refinement of the models could improve the data fit throughout the channel.

The results of this section indicate that while the streamwise energy amplification associated with the $q = 2$ and $q = 3$ wall-normal harmonics are more than 3 orders of magnitude smaller than that of $q = 1$, their dynamic behavior serves as a sort of correction factor for the mean velocity profile. The turbulent mean profile at this Reynolds number can be well approximated using steady-state solutions of the $2D/3C$ model with the stream function in (6.2) as input. This does not however suggest that all aspects of the turbulent behavior can be captured by such a model, but rather that our model reproduces the mechanisms involved in transforming a spanwise/wall-normal large-scale "streaky" structure into

a "turbulent-like" streamwise velocity profile.

6.5   Analytical Solutions

In this section we investigate spanwise varying nominal streamwise velocities $U(y, z)$ obtained through applying steady-state stream functions $\Phi(y, z)$ to a nominal streamwise velocity evolution equation

$$\cancel{\frac{\partial U}{\partial t}}^{0} = \left(-\frac{\partial \Phi}{\partial z} \frac{\partial}{\partial y} + \frac{\partial \Phi}{\partial y} \frac{\partial}{\partial z} + \frac{1}{R} \left(\frac{\partial^2}{\partial y^2} + \frac{\partial^2}{\partial z^2} \right) \right) U(y, z). \tag{6.13}$$

This $U(y, z)$ is not meant to represent the time-averaged turbulent mean velocity profile, which is not spanwise varying. It is a purely spatial representation of the streamwise velocity in the y–z plane. One can think of this as representing a cut of this plane in a fully developed turbulent Couette flow. In order to have high- and low-speed excursions from the local mean at a particular wall-normal location, any given spatial y–z plane would necessarily vary in the spanwise direction, as would a snapshot in time.

The goal of this section is to gain insight into the mathematical mechanisms involved in turning cross-stream "roll-like" structures into a "blunted" streamwise velocity profile. Since we are not comparing the results to the DNS data from [91], for mathematical convenience we go back to the configuration $y \in [-1, 1]$, as in Figure 3.1. The velocity is scaled such that $U_{top} = 1$ and $U_{bottom} = -1$.

Computation of $U(y, z)$ from a given $\Phi(y, z)$ can be obtained from the nominal $U(y, z)$ evolution equation (6.13), with boundary conditions $U(-1, z) = -1$, $U(1, z) = 1$, and an infinite spanwise extent. If we employ the change of variables $\mathbf{\Psi} = R\Phi$, then we obtain a Reynolds-number-independent expression

$$-\frac{\partial \Psi}{\partial z} \frac{\partial U}{\partial y} + \frac{\partial \Psi}{\partial y} \frac{\partial U}{\partial z} + \Delta U = 0. \tag{6.14}$$

The solution to this equation can be estimated using a perturbation technique (weakly nonlinear analysis). In this case we assume expansions of both $U(y, z)$ and $\Psi(y, z)$, such

that

$$U(y, z) = U_0 + \varepsilon U_1 + \varepsilon^2 U_2 \ldots$$

$$\boldsymbol{\Psi}(y, z) = \boldsymbol{\Psi}_0 + \varepsilon \boldsymbol{\Psi}_1 + \varepsilon^2 \boldsymbol{\Psi}_2 \ldots$$

Filling these expressions into (6.14) yields

$$
\begin{aligned}
0 = & -\frac{\partial \boldsymbol{\Psi_0}}{\partial z}\frac{\partial U_0}{\partial y} - \varepsilon \left(\frac{\partial \boldsymbol{\Psi_0}}{\partial z}\frac{\partial U_1}{\partial y} + \frac{\partial \boldsymbol{\Psi_1}}{\partial z}\frac{\partial U_0}{\partial y} \right) \\
& - \varepsilon^2 \left(\frac{\partial \boldsymbol{\Psi_1}}{\partial z}\frac{\partial U_1}{\partial y} + \frac{\partial \boldsymbol{\Psi_0}}{\partial z}\frac{\partial U_2}{\partial y} + \frac{\partial \boldsymbol{\Psi_2}}{\partial z}\frac{\partial U_0}{\partial y} \right) + \frac{\partial \boldsymbol{\Psi_0}}{\partial y}\frac{\partial U_0}{\partial z} \\
& + \varepsilon \left(\frac{\partial \boldsymbol{\Psi_0}}{\partial y}\frac{\partial U_1}{\partial z} + \frac{\partial \boldsymbol{\Psi_1}}{\partial y}\frac{\partial U_0}{\partial z} \right) + \varepsilon^2 \left(\frac{\partial \boldsymbol{\Psi_1}}{\partial y}\frac{\partial U_1}{\partial z} + \frac{\partial \boldsymbol{\Psi_2}}{\partial y}\frac{\partial U_0}{\partial z} + \frac{\partial \boldsymbol{\Psi_0}}{\partial y}\frac{\partial U_2}{\partial z} \right) \\
& + \frac{\partial^2 U_0}{\partial y^2} + \frac{\partial^2 U_0}{\partial z^2} + \varepsilon \frac{\partial^2 U_1}{\partial y^2} + \varepsilon \frac{\partial^2 U_1}{\partial z^2} + \varepsilon^2 \frac{\partial^2 U_2}{\partial y^2} + \varepsilon^2 \frac{\partial^2 U_2}{\partial z^2} + \ldots .
\end{aligned}
\tag{6.15}
$$

Then, matching like powers of ε, leaves us with the following:

$$
\begin{aligned}
(\varepsilon^0 :) \quad & \frac{\partial \boldsymbol{\Psi_0}}{\partial z}\frac{\partial U_0}{\partial y} - \frac{\partial \boldsymbol{\Psi_0}}{\partial y}\frac{\partial U_0}{\partial z} = \frac{\partial^2 U_0}{\partial y^2} + \frac{\partial^2 U_0}{\partial z^2}, \\
(\varepsilon :) \quad & \frac{\partial \boldsymbol{\Psi_0}}{\partial z}\frac{\partial U_1}{\partial y} + \frac{\partial \boldsymbol{\Psi_1}}{\partial z}\frac{\partial U_0}{\partial y} - \left(\frac{\partial \boldsymbol{\Psi_0}}{\partial y}\frac{\partial U_1}{\partial z} + \frac{\partial \boldsymbol{\Psi_1}}{\partial y}\frac{\partial U_0}{\partial z} \right) = \frac{\partial^2 U_1}{\partial y^2} + \frac{\partial^2 U_1}{\partial z^2}, \\
(\varepsilon^2 :) \quad & \frac{\partial \boldsymbol{\Psi_1}}{\partial z}\frac{\partial U_1}{\partial y} + \frac{\partial \boldsymbol{\Psi_0}}{\partial z}\frac{\partial U_2}{\partial y} + \frac{\partial \boldsymbol{\Psi_2}}{\partial z}\frac{\partial U_0}{\partial y} \\
& \quad - \left(\frac{\partial \boldsymbol{\Psi_1}}{\partial y}\frac{\partial U_1}{\partial z} + \frac{\partial \boldsymbol{\Psi_2}}{\partial y}\frac{\partial U_0}{\partial z} + \frac{\partial \boldsymbol{\Psi_0}}{\partial y}\frac{\partial U_2}{\partial z} \right) = \frac{\partial^2 U_2}{\partial y^2} + \frac{\partial^2 U_2}{\partial z^2},
\end{aligned}
\tag{6.16}
$$

for the ε^0, ε^1 and ε^2 terms in the expansion.

In order to solve these expressions we assume that the zeroth-order streamwise velocity and stream functions are of the form $U_0(y, z) = U_0(y)$ (to reproduce a laminar flow condition) and $\boldsymbol{\Psi}_0 = 0$. Based on the results of the previous section we also assume that a spanwise periodic stream function that gives rise to a "blunted" nominal velocity can be captured using the first-order term, i.e.,

$$\boldsymbol{\Psi}(y, z) = \varepsilon \boldsymbol{\Psi}_1 = \varepsilon \alpha_1(y) \cos(k_z z). \tag{6.17}$$

Filling in the condition on U_0 and this $\boldsymbol{\Psi}$ (6.17), into the expressions in (6.16) yields

$$\frac{\partial^2 U_0}{\partial y^2} = 0 \tag{6.18a}$$

$$-k_z \alpha(y) \frac{\partial U_0}{\partial y} \sin(k_z z) = \frac{\partial^2 U_1}{\partial y^2} + \frac{\partial^2 U_1}{\partial z^2} \tag{6.18b}$$

$$-\left(k_z \alpha(y) \frac{\partial U_1}{\partial y} \sin(k_z z) + \frac{\partial \alpha(y)}{\partial y} \frac{\partial U_1}{\partial z} \cos(k_z z) \right) = \frac{\partial^2 U_2}{\partial y^2} + \frac{\partial^2 U_2}{\partial z^2}. \tag{6.18c}$$

The ε^n equations for $n \geq 3$ are the same as Equation (6.18c) for ε^2, with U_1 and U_2 respectively replaced by U_{n-1} and U_n.

The boundary conditions $U(-1, z) = -1$ and $U(1, z) = 1$ can be broken down such that $U_0(-1, z) = -1$, $U_0(1, z) = 1$ and $U_n(\pm 1, z) = 0 \ \forall n \geq 1$. Using these conditions,

$$U_0(y) = y. \tag{6.19}$$

This is exactly the laminar solution for Couette flow. In order to solve for the remaining terms in the expansion we need to assume a form for $\alpha(y)$.

6.5.1 Solution Method

In this section we illustrate a method to solve for the first- and second-order terms in the U expansion, i.e., solutions of Equation (6.18b) and (6.18c) for $U_1(y, z)$ and $U_2(y, z)$, for two different $\alpha(y)$ functions.

We are interested in stream functions of the form, $\mathbf{Psi} = \varepsilon \alpha(y) \cos(k_z z)$, that represent large streamwise elongated structures such as the ψ_{ss} model (6.2) discussed in sections 6.2–6.4. In the $y \in [-1, 1]$ coordinate frame that stream function would correspond to $\alpha(y) = \cos^2\left(q \frac{\pi}{2} y\right)$. This would therefore be the natural function to start with. However, in order to better demonstrate the method and obtain closed form solutions we are going to start with $\alpha(y) = \cos\left(\frac{\pi}{2} y\right)$ instead. Figures 6.10(a) and 6.10(b) show that this form of $\alpha(y)$ also produces very similar structures to the ψ_{ss} model described by (6.2) (in the new $y \in [-1, 1]$ coordinate frame). The mean velocity profiles $U - y$ (deviation from laminar) generated using $\Phi = 0.002\alpha(y) \cos(k_z z)$ and Equation (6.13) with the two different $\alpha(y)$ models at $R_c = 750$ (which is equivalent to $R_w = 3000$) with $\lambda_z = 1.8\delta$ also have similar features. Both illustrate the velocity deficit near the top wall and the velocity increase near

(a) $0.002\cos(\frac{\pi}{2}y)\cos(k_z z)$

(b) $0.002\cos(\frac{\pi}{2}y)^2\cos(k_z z)$

(c) Velocity Profile Comparison

(d)
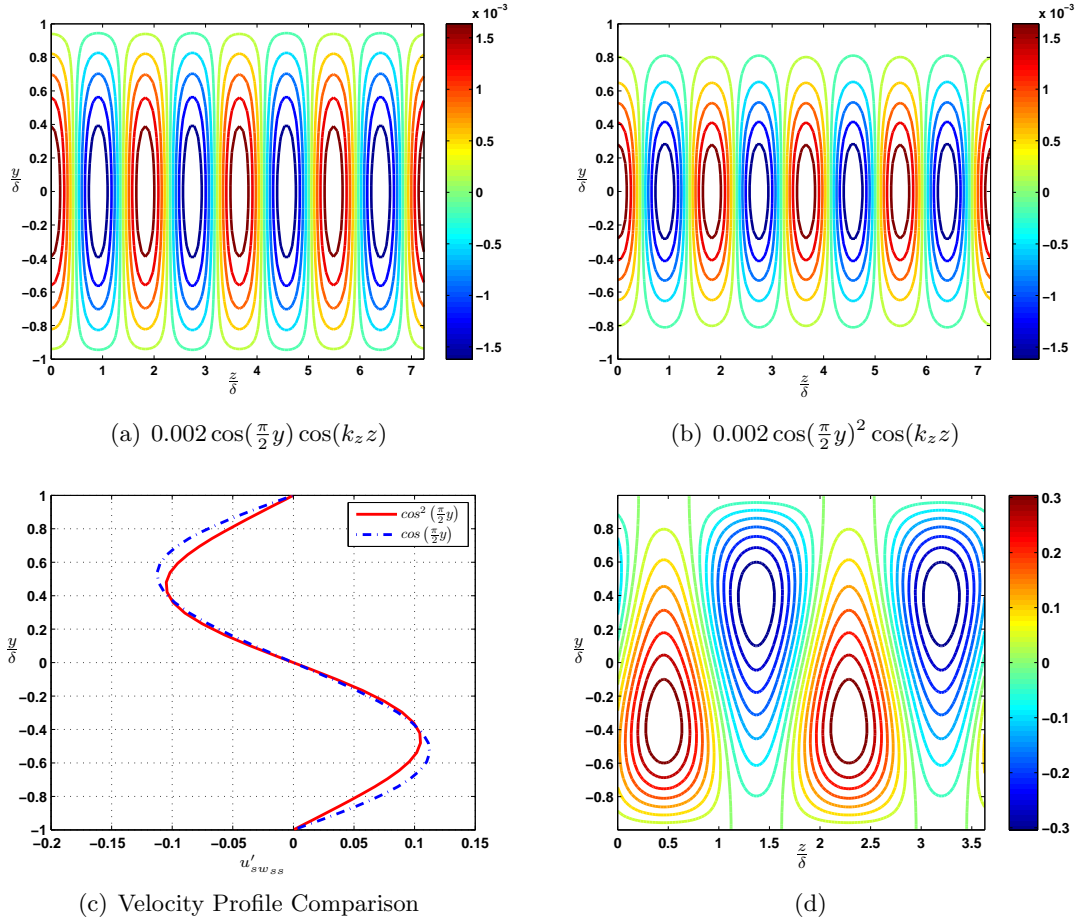
Figure 6.10: Panels (a) and (b) are contour plots of $\Phi = 0.002\cos(\frac{\pi}{2}y)\cos(k_z z)$ and $\Phi = 0.002\cos^2(\frac{\pi}{2}y)\cos(k_z z)$ respectively; both with $\frac{2\pi}{k_z} = \lambda_z = 1.8\delta$ (c) Comparison of velocity profiles $U - y$ (deviation from laminar) computed from Equation (6.13) with $\Phi = \cos(\frac{\pi}{2}y)\cos(k_z z)$ and $\Phi = \cos^2(\frac{\pi}{2}y)\cos(k_z z)$ both with $R_c = 750$ ($R_w = 3000$) and $\lambda_z = 1.8\delta$. (d) Contour plot of $U(y, z) - y$ (deviation from laminar) computed from Equation (6.13) $\Phi = 0.002\cos(\frac{\pi}{2}y)\cos(k_z z)$.

the bottom wall that lead to the "S" shaped or "blunted" velocity profile. Therefore, the $\alpha(y) = \cos\left(q\frac{\pi}{2}y\right)$ generates the desired behavior and can reasonably be used to illustrate the method for solving Equation (6.14) as well as the general properties of the solution.

Given $\alpha(y) = \cos(\frac{\pi}{2}y)$, Equation (6.18b) becomes

$$-k_z \cos\left(\frac{\pi}{2}y\right)\sin(k_z z) = \frac{\partial^2 U_1}{\partial y^2} + \frac{\partial^2 U_1}{\partial z^2} = \mathcal{A}U_1, \tag{6.20}$$

with $U_1(\pm 1, z) = 0$ and an infinite spanwise extent.

We want to write U_1 in terms of basis functions ($\xi_n(y)$ and $\beta_l(z)$) that satisfy its bound-

ary conditions. An appropriate choice is

$$\xi_n(y) = \sin\left(\frac{\pi}{2}n(y+1)\right) \tag{6.21a}$$

$$\beta_l(z) = e^{-jlz}. \tag{6.21b}$$

Then

$$U_1(y,z) = \sum_{n\geq 1,l} \vartheta_{n,l}^1 \sin\left(\frac{\pi}{2}n(y+1)\right) e^{-jlz}. \tag{6.22}$$

Note that $\sin\left(\frac{\pi}{2}(y+1)\right) = \cos\left(\frac{\pi}{2}y\right)$.

Using (6.22) the equation for the coefficients of U_1 equation (6.20) can be written as

$$-\frac{k_z}{2j}\left[\delta(l-k_z) - \delta(l+k_z)\right]\delta(n-1) = -\vartheta_{n,l}\left(\frac{\pi^2 n^2}{4} + l^2\right).$$

From this it is clear that $l = \pm k_z$ and $n = 1$, which means

$$\begin{aligned}
U_1(y,z) &= \frac{k_z}{2j\left(\frac{\pi^2}{4} + k_z^2\right)} \sin\left(\frac{\pi}{2}(y+1)\right)\left[e^{-jk_z z} - e^{-jk_z z}\right] \\
&= \frac{k_z}{\left(\frac{\pi^2}{4} + k_z^2\right)} \sin\left(\frac{\pi}{2}(y+1)\right)\sin(k_z z).
\end{aligned} \tag{6.23}$$

We can solve the U_2 expression (6.18c) in a similar manner. We assume that $U_2(y,z)$ can be written in terms of the same basis functions as U_1, i.e.,

$$U_2(y,z) = \sum_{n\geq 1,l} \vartheta_{n,l}^2 \sin\left(\frac{\pi}{2}n(y+1)\right) e^{-jlz}. \tag{6.24}$$

The U_2 expression (6.18c) with $\alpha(y) = \cos\left(\frac{\pi}{2}y\right)$ is given by

$$-\left(k_z \sin\left(\frac{\pi}{2}(y+1)\right)\frac{\partial U_1}{\partial y}\sin(k_z z) + \frac{\pi}{2}\cos\left(\frac{\pi}{2}(y+1)\right)\frac{\partial U_1}{\partial z}\cos(k_z z)\right) = \frac{\partial^2 U_2}{\partial y^2} + \frac{\partial^2 U_2}{\partial z^2}.$$

Filling in the U_1 solution (6.23) this becomes

$$-\frac{\pi k_z^2}{2\left(\frac{\pi^2}{4} + k_z^2\right)}\sin\left(\frac{\pi}{2}(y+1)\right)\cos\left(\frac{\pi}{2}(y+1)\right)\left[\sin^2(k_z z) + \cos^2(k_z z)\right] = \Delta U_2 \tag{6.25a}$$

$$-\frac{\pi k_z^2}{4\left(\frac{\pi^2}{4} + k_z^2\right)}\sin\left(\pi(y+1)\right) = \frac{\partial^2 U_2}{\partial y^2} + \frac{\partial^2 U_2}{\partial z^2}. \tag{6.25b}$$

Then the coefficients of U_2 satisfy

$$-\frac{\pi k_z^2}{4\left(\frac{\pi^2}{4} + k_z^2\right)}\delta(l)\delta(n-2) = -\left(\frac{\pi^2 n^2}{4} - l^2\right)\vartheta_{n,l}^2.$$

This implies $l = 0$ and $n = 2$ and therefore

$$U_2(y,z) = \frac{k_z^2}{4\pi\left(\frac{\pi^2}{4} + k_z^2\right)}\sin(\pi(y+1)). \tag{6.26}$$

So, U_2 is only a function of y. One can similarly obtain

$$U_3 = \frac{k_z^3}{8\left(\frac{\pi^2}{4} + k_z^2\right)}\left[\frac{1}{\left(\frac{9\pi^2}{4} + k_z^2\right)}\sin\left(\frac{3\pi}{2}(y+1)\right) - \frac{1}{\left(\frac{\pi^2}{4} + k_z^2\right)}\sin\left(\frac{\pi}{2}(y+1)\right)\right]\sin(k_z z).$$

These closed form solutions expressions for U_1, U_2 and U_3 tell us some interesting things about the mathematical mechanisms involved in developing the "blunted" profile seen in Figure 6.10(c) and 6.10(d). The spanwise mean of both $U_1(y,z)$ and $U_3(y,z) = 0$, therefore these expressions do not affect the mean velocity profile. The nonzero nonlinear terms on the left hand side of these equations are $\frac{\partial\Psi_1}{\partial z}\frac{\partial U_0}{\partial y}$ and $\frac{\partial\Psi_1}{\partial z}\frac{\partial U_2}{\partial y}$, respectively. When U_{n-1} is solely a function of y, then $U_n = g(y)\sin(k_z z)$, thus U_n has a spanwise mean of zero. So, the blunting cannot arise solely from the nonlinear coupling of the form $\frac{\partial\Psi_1}{\partial z}\frac{\partial U_{n-1}}{\partial y}$, with $U_{n-1}(y)$.

A spanwise average over $U_2(y)$ has a form that would lead to a "blunted" velocity profile. Figure 6.11 shows a plot of $U_2(y)$. It is clear from Equation (6.25a) that the blunting is an equal result of each of the two expressions $\frac{\partial\Psi_1}{\partial y}\frac{\partial U_1}{\partial z}$ and $\frac{\partial\Psi_1}{\partial z}\frac{\partial U_1}{\partial y}$. This can be seen by taking a spanwise average (or integral) over either $\sin^2(k_z z)$ or $\cos^2(k_z z)$. If U_1 did not depend on z then we would have $U_2(y,z) = C\sin(\pi(y+1))\sin(k_z z)$, which has a spanwise average of zero. This provides evidence that both of the nonlinear terms in the streamwise evolution equation of the $2D/3C$ model (6.1a) play an equal role in the momentum transfer required to produce a "turbulent-like" mean velocity profile. In addition a spanwise variation is required to generate a spanwise averaged velocity profile that deviates from the laminar U_0.

We will now briefly go through the solution of the $\tilde{U}_1$ equation (6.18b) for $\tilde{\alpha}(y) = \cos^2\left(\frac{\pi}{2}y\right)$. We use the $\tilde{(\cdot)}$ to avoid confusion between the two $\alpha(y)$ cases. Filling this into
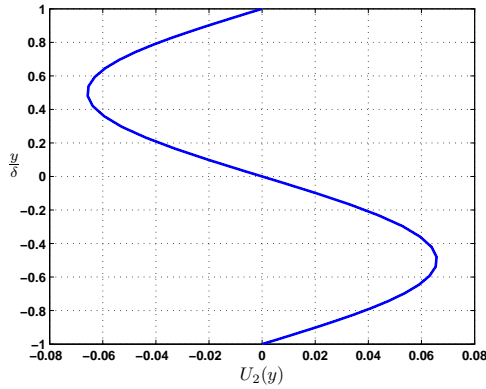
Figure 6.11: Plot of $U_2(y)$ with $k_z = 3.4$ ($\lambda_z = 1.8\delta$).

the $\tilde{U}_1$ expression (6.18b), it becomes

$$
\begin{aligned}
-\frac{\partial \mathbf{\Psi}}{\partial z}\frac{\partial U_0}{\partial y} &= \frac{\partial^2 \tilde{U}_1}{\partial y^2} + \frac{\partial^2 \tilde{U}_1}{\partial z^2} \\
-k_z \cos^2\left(\frac{\pi}{2}y\right)\sin(k_z z) &= \frac{\partial^2 \tilde{U}_1}{\partial y^2} + \frac{\partial^2 \tilde{U}_1}{\partial z^2}.
\end{aligned}
\tag{6.27}
$$

We assume this $\tilde{U}_1(y,z)$ can also written in terms of basis functions $\tilde{\eta}_n(y) = \sin\left(\frac{\pi}{2}n(y+1)\right)$ and $\tilde{\beta}_l(z) = e^{-jlz}$ i.e., $\tilde{U}_1(y,z) = \sum_{n\geq 1, l} \tilde{\vartheta}_{n,l}^1 \sin\left(\frac{\pi}{2}n(y+1)\right)e^{-jlz}$.

Then $\cos^2\left(\frac{\pi}{2}y\right)$ needs to be projected onto the basis function $\tilde{\eta}_n(y) = \sin\left(\frac{\pi}{2}n(y+1)\right)$.

$$
\begin{aligned}
&\int_{-1}^{1} \cos^2\left(\frac{\pi}{2}y\right)\sin\left(\frac{\pi}{2}n(y+1)\right) dy \\
&= \int_{-1}^{1} \sin^2\left(\frac{\pi}{2}(y+1)\right)\sin\left(\frac{\pi}{2}n(y+1)\right) dy \\
&= \frac{1}{2}\int_{-1}^{1}\left\{\sin\left(\frac{\pi}{2}n(y+1)\right) - \cos\left(\pi(y+1)\right)\sin\left(\frac{\pi}{2}n(y+1)\right)\right\} dy \\
&= -\frac{1}{n\pi}\left[\cos(\pi n) - 1\right] - \frac{1}{4}\int_{-1}^{1}\sin\left(\frac{\pi}{2}(n-2)(y+1)\right) dy - \frac{1}{4}\int_{-1}^{1}\sin\left(\frac{\pi}{2}(n+2)(y+1)\right) dy \\
&= -\frac{1}{n\pi}\left[\cos(\pi n) - 1\right] + \frac{1}{2\pi(n-2)}\left[\cos((n-2)\pi) - 1\right]\Big|_{n\neq 2} + \frac{1}{2\pi(n+2)}\left[\cos((n+2)\pi) - 1\right] \\
&= -\frac{n^2 - 4}{\pi n(n^2 - 4)}\left[\cos(\pi n) - 1\right] + \frac{n^2}{\pi n(n^2 - 4)}\left[\cos(n\pi) - 1\right] \\
&= \frac{4}{\pi n(n^2 - 4)}\left[(-1)^n - 1\right].
\end{aligned}
$$

For $n = 2$ the integral $\{\int_{-1}^{1} \sin\left(\frac{\pi}{2}(n-2)(y+1)\right) dy\}$ vanishes. The resulting expression is

$$\tilde{U}_1(y, z) = \sum_{\{n \geq 1 : n \text{ odd}\}} \frac{4\left[(-1)^n - 1\right]}{\pi n(n^2 - 4)\left(\frac{n^2\pi^2}{4} + k_z^2\right)} \sin\left(n\frac{\pi}{2}(y+1)\right) \sin(k_z z) \qquad (6.28)$$

U_1 is an infinite sum over odd n. Therefore, similar to the case with $\alpha(y) = \cos\left(\frac{\pi}{2}y\right)$, the $\tilde{U}_1$ terms will not lead to a "blunted" profile. This supports our earlier assessment that both nonlinear terms in (6.1a) and a spanwise varying U are required to create a "blunted" profile.

6.6 Summary

In this chapter we studied forced solutions of the $2D/3C$ streamwise velocity evolution equation (6.1a). The input we employed was a steady-state stream function ψ_{ss}, which was used as a model for large-scale channel-spanning streamwise elongated structures. The ψ_{ss} was expressed as weakly nonlinear expansion of the form $\psi_{ss} = \psi_{ss_0} + \varepsilon\psi_{ss_1} + \varepsilon^2\psi_{ss_2}$. The zeroth-order term corresponds to the linear case so we set $\psi_0 = 0$. We only considered the effect of the first-order term $\varepsilon\psi_{ss_1}$. The spanwise/wall-normal $(y\text{–}z)$ plane forcing (Υ) required to generate ψ_{ss} was determined using the $2D/3C$ ψ evolution equation (6.1b).

We selected a doubly harmonic (in y and z) model for ψ_{ss_1} that produced the same qualitative features of a full spatial field $(u, v, w, p)(x, y, z)$ of DNS data we obtained from the Kawamura group [91]. The initial parameters for the model, i.e., ε and k_z (the spanwise wave number), were also selected to be consistent with the DNS.

The forced solutions, $u'_{sw_{ss}}$, that we obtained using the ψ_{ss} model had qualitative features similar to those of the DNS and the results of the full stochastic simulation of Chapter 5. Varying the stream function model's amplitude, ε, created trends consistent with an increase in model uncertainty (forcing). The model with a single harmonic in y could not reproduce the exact shape of the turbulent velocity profile. In Section 6.4 we showed that by increasing the number of wall-normal harmonics we can vastly improve the agreement of the mean velocity profile. These results provide evidence that the nonlinear terms in the $2D/3C$ streamwise velocity equation are responsible for the momentum transfer associated with the change in profile from the nominal laminar to the turbulent state. Very little forcing was necessary to develop the features consistent with the turbulent velocity profile.

This indicates that the globally stable laminar solution is not robust to small disturbances.

In Section 6.3 an input-output energy amplification factor Γ_{ss} analogous to an induced norm from the forcing Υ to the forced solution $u'_{sw_{ss}}$ was introduced. We used this to determine the energy optimal spanwise wave number over a range of Reynolds numbers ($3000 \leq R_w \leq 12000$) and compared our results to previous studies of the LNS. Our results at $R_w = 3000$ were similar to the outer unit scaled optimal energy peaks in a similar study of Couette flow at the same Reynolds numbers. The larger Reynolds number optimal energy occurred at wavelengths somewhat longer than those from similar studies of Poiseuille flow. Reynolds number scaling of the amplification factor was consistent with previous parallel flow studies.

The mean velocity profiles associated with optimal energy (maximum Γ_{ss}) were computed for different ψ_{ss} model (i.e., forcing) amplitudes. We demonstrated that the profiles become more "blunted" with increasing amplitude and increasing wave number k_z. However, the profiles overshoot the mean velocity at the centerline when either k_z or the forcing amplitude exceed a threshold value. The amplification factor ceases to increase even though the velocity gradient at the wall continues to increase with both k_z and ε. In fact Γ_{ss} monotonically decreases with ε.

In Section 6.5 we developed a method for analytically computing the few terms in a weakly nonlinear expansion of the nominal streamwise velocity equation. Using a steady-state stream function meant to represent a steady-state large-scale streamwise coherent y–z plane feature. Using this analysis we were able to recover the laminar profile as the zeroth-order term U_0 in the expansion. The blunting of the profile came from the second-order term U_2. It required a spanwise varying U_1, which made use of both of the nonlinear terms in the $2D/3C$ streamwise velocity equation. This analysis confirmed the role of the nonlinear terms in the momentum transfer required to generate the turbulent mean velocity.

Chapter 7

Conclusions

This thesis presents a robust control view of turbulent plane Couette flow. The early chapters (2 and 3) introduce the preliminary mathematical and dynamical systems concepts necessary for our discussion of shear flow turbulence. They also explore the relationship between these flows and robust control related ideas.

Chapter 4 introduces a streamwise constant projection of the Navier Stokes (NS) equations, corresponding to a two-dimensional, three-velocity component ($2D/3C$) model. The assumption of homogeneity in the streamwise direction is based on the long-held belief that streamwise constant structures have a significant role in both transition and fully developed turbulent flows. We choose this particular $2D/3C$ model because it provides a reasonable amount of analytical tractability and is based on the physics of the problem. Such a physics-based model provides greater insight into the dynamics of the system than an empirical technique and thus may facilitate control design.

In Chapter 5, we demonstrate that simulations of this model under small-amplitude Gaussian forcing capture the salient features of fully developed turbulent flow. We highlight its ability to develop a turbulent mean velocity profile from a nominal laminar initial condition. Appropriate Reynolds number trends are also reproduced. Our simulations demonstrate that generation of a turbulent velocity profile consistent with Direct Numerical Simulations (DNS) and experiments requires a nonlinear streamwise velocity equation. However, linear spanwise/wall-normal (z–y plane) equations are sufficient.

The use of small-amplitude stochastic forcing as an input to the $2D/3C$ (nominal) model is based on ideas from robust control. Experimental observations are used to simplify the NS equations to form this nominal model. The noise forcing is used to capture both uncertain parameter values and unmodeled effects. The resulting forced $2D/3C$ model maintains a

sufficiently rich description of the physics that govern turbulent flow, while allowing one to isolate phenomena that cannot be decoupled from a full simulation of NS.

The linearized $2D/3C$ model (4.3) maintains the properties responsible for large disturbance amplification. These properties have been linked to subcritical transition. Maintenance of these linear mechanisms is critical to the success of our approach. It is the combination of these linear processes along with the momentum transfer from the two nonlinear terms in the streamwise velocity equation that enables the model to develop a "turbulent-like" velocity profile. This line of inquiry provides a complementary perspective to transient growth and structurally based models. In particular, the $2D/3C$ model offers some improvement in analytic tractability at the expense of streamwise detail. The results are especially promising because the computational and analytical tractability of this model makes it well-suited to higher Reynolds number studies.

The laminar flow solution of the $2D/3C$ model is globally stable for all Reynolds numbers (R). However, it has the same potential for R^3 energy growth as the linearized equations. This capacity for large disturbance amplification indicates that the laminar solution of $2D/3C$ model may not be robustly stable for large R. The results of Chapter 5 confirm that very little forcing is necessary to develop the mean features of turbulence. In other words, small perturbations around the stable laminar solution lead to the inability of the $2D/3C$ flow to maintain the nominal behavior. The $2D/3C$ model's ability to generate "turbulent-like" behavior under small-amplitude stochastic noise indicates that transition in this model is related to the large linear disturbance amplification, or the $2D/3C$ laminar flow solution's lack of robustness.

Streamwise convection of the simulation results at the centerline captures streamwise elongated coherent motions in the core. Further study of these features using the $2D/3C$ model may give us a new insight into their nature. In a full simulation, isolating these large-scale structures from the small-scale turbulent motions that surround them requires the scale separation associated with mid to high Reynolds numbers. DNS is generally only available at low to mid Reynolds numbers. The $2D/3C$ model eliminates these Reynolds number constraints because the small-scale motions are simply not present.

In Chapter 6 we use periodic spanwise/wall-normal stream functions to represent a steady-state idealized model of streamwise streaks and vortices. This stream function model is used as the input to the time-independent $2D/3C$ streamwise velocity equation. The

corresponding fixed points are the forced steady-state streamwise velocity solutions for each steady-state stream function. These solutions have qualitative features similar to those of a spatial field of DNS data as well as to the results of the full stochastic simulation of Chapter 5. The nature of the solutions provides evidence that the nonlinear coupling in the $2D/3C$ streamwise velocity equation, when combined with the appropriately shaped stream functions, produces features consistent with the mean characteristics of fully developed turbulence. The momentum transfer that produces the correct mean profile appears to require a nonlinear momentum equation for the streamwise velocity component.

In Section 6.3 we use a system theoretic approach to further examine the amplification mechanisms that develop through the nonlinear coupling in the $2D/3C$ streamwise velocity equation. We compute the spanwise/wall-normal (z–y) plane forcing required to produce a particular stream function. Then, an induced norm from this forcing input to the streamwise velocity is used to determine the input-output amplification. The spanwise wave number where the maximal amplification occurs provides an estimate of the spanwise preferential spacing. This analysis serves to augment the well-developed linear theory through the addition of the nonlinear coupling of the stream function. It provides additional insight similar to that which was gained (into the development of mean profile) through keeping the nonlinearity in the simulation of $2D/3C$ model.

Simulations of $2D/3C$ equations with a nominal (laminar) flow solution ($U(y)$, 0, 0) under cross-stream small stochastic forcing yield mean flow solutions ($\bar{u}(y, z)$, $\bar{v}(y, z)$, $\bar{w}(y, z)$). These solutions are roughly periodic in z. In Section 6.5, we use a perturbation technique (weakly nonlinear analysis) to analytically investigate the new nominal streamwise velocity solutions, $U(y, z)$, which arise through assuming that the flow has cross-stream velocities $V(y, z)$ and $W(y, z)$. We assume these cross-stream velocities correspond to streamwise elongated large-scale streaks and vortices. The analysis recovers the laminar profile as the zeroth-order term U_0 corresponding to no cross-stream components ($V = W = 0$). The blunting of the profile does not appear until the second-order term U_2. Creation of a "blunted" profile required a spanwise varying U_1, which made use of both of the nonlinear terms in the $2D/3C$ streamwise velocity equation. This may be interpreted as a confirmation of the necessity the $2D/3C$ nonlinear coupling in generating the momentum transfer required to produce the turbulent mean velocity. The fact that we were able to obtain closed form solutions (that are also spanwise periodic) for certain stream function inputs

indicates the potential for further analytical understanding of both this model as well as the physical mechanisms associated with blunting.

Future work along this direction would include both linear and nonlinear stability analysis. The theory of spatially distributed periodic systems [21, 22] can be used to perform linear stability and norm analysis for spanwise periodic stream function, streamwise velocity solution pairs. The norm analysis can be compared to the input-output analysis in Section 6.3. Previous studies have looked at linear stability of the time-averaged turbulent velocity profile but there are no studies of three-dimensional perturbations about a spanwise varying profile. Following the linear study, the development of a Lyapunov function to show stability of the forced nonlinear equations would provide a complete picture.

A natural extension of the simulation related work would be the development of a more appropriate model for the noise distribution. This would be equivalent to introducing a so-called structured uncertainty based on the physics and experimental conditions of a flow system. In this dissertation, the limitation of noise to only the cross-stream components (the $\Delta \psi$ equation) represents a first level of such an approach. Exploiting knowledge of the physics, for example that the near-wall region is under-resolved in the $2D/3C$ model, is the next logical course of action. Section 5.4.4 presented a step toward this type of noise model through the use of a Chebyshev wall-normal interpolant. Numerical or experimental studies aimed at characterizing true spatial noise forcing patterns would further help in determining the correct model for the noise distribution.

Other future work involves characterizing the robustness of the blunting mechanism. The fact that the steady-state $2D/3C$ model produces a "blunted", "turbulent-like" profile using very simple stream functions as inputs suggests a preference for a redistribution of momentum along the wall-normal direction. It would be interesting to see if this behavior, which appears to be robust to small changes in the stream function model, is due to the dominance of some particular set of dynamic modes. Previous studies have shown that the response of the full LNS can be reproduced using a very small number of modes [25]. Similarly, principle orthogonal decomposition has been used to create accurate low-order models from turbulent flow data, e.g. [82]. This suggests that there is a large separation between the largest singular values and the remaining ones [62]. So in some sense the dynamics behave similarly to those of a low rank operator. It would be of interest to mathematically demonstrate that the blunting mechanism is the result of a similar phenomena. In other

words, we are interested in showing that the nonlinear $2D/3C$ model behaves like a *high gain/low rank* operator. This would explain why the mean profile is repeatable under a variety of experimental conditions and numerical schemes. It may also provide further insight into the transition problem.

Bibliography

[1] B. Bamieh. *Spatially Distributed Systems Theory*. In Preparation, 2010.

[2] B. Bamieh and M. Dahleh. Energy amplification in channel flows with stochastic excitation. *Phys. of Fluids*, 13(11):3258–3269, 2001.

[3] B. Bamieh, F. Paganini, and M. A. Dahleh. Distributed control of spatially invariant systems. *IEEE Trans. on Automatic Control*, 47(7):1091–1107, July 2002.

[4] S. P. Banks. *State-Space and Frequency-Domain Methods in the Control of Distributed Parameter Systems*. IEE Topics in Control Series, Vol. 3, Peter Peregrinus Ltd., London, 1983.

[5] D. Barkley and L. S. Tuckerman. Mean flow of turbulent-laminar patterns in plane Couette flow. *J. Fluid Mech.*, 576:109–137, 2007.

[6] B. J. Bayly, S. A. Orszag, and T. Herbert. Instability mechanisms in shear-flow transition. *Annual Rev. of Fluid Mech.*, 20:359–391, 1988.

[7] K. H. Bech, N. Tillmark, P. H. Alfredsson, and H. I. Andersson. An investigation of turbulent plane Couette flow at low Reynolds numbers. *J. Fluid Mech.*, 286:291–325, 1995.

[8] K. M. Bobba. *Robust flow stability: Theory, computations and experiments in near wall turbulence*. PhD thesis, California Institute of Technology, Pasadena, USA, 2004.

[9] K. M. Bobba, B. Bamieh, J. C. Doyle, and A. Papachristodoulou. Global stability and transient growth of stream-wise constant perturbations in parallel flows. *In preparation*, 2010.

[10] K. M. Butler and B. F. Farrell. Three-dimensional optimal perturbations in viscous shear flow. *Phys. of Fluids A*, 4:1637–1650, 1992.

[11] R. F. Curtain and H. J. Zwart. *An Introduction to Infinite-Dimensional Linear Systems Theory*. Texts in Applied Mathematics, Vol. 21, Springer-Verlag, New York, 1995.

[12] J. Davies and C. M. White. An experimental study of the flow of water in pipes of rectangular section. *Proceedings of the Royal Society of London Ser. A*, 119:92, 1928.

[13] J. C. del Álamo and J. Jiménez. Linear energy amplification in turbulent channels. *J. Fluid Mech.*, 559:205–213, 2006.

[14] D. J. C. Dennis and T. B. Nickels. On the limitations of Taylor's hypothesis in constructing long structures in a turbulent boundary layer. *J. Fluid Mech.*, 614:197–206., 2008.

[15] J. C. Doyle, B. Francis, and A. Tannenbaum. *Feedback Control Theory*. MacMillan Company, New York, 1991.

[16] P. E. Drazin and W. H. Reid. *Hydrodynamic Stability*. Cambridge University Press, London, 1981.

[17] G. E. Dullerud and F. Paganini. *A Course in Robust Control Theory: A Convex Approach*. Texts in Applied Mathematics, Vol. 36, Springer-Verlag, New York, 2000.

[18] B. Eckhardt, H. Faisst, A. Schmiegel, and T. M. Schneider. Dynamical systems and the transition to turbulence in linearly stable shear flows. *Phil. Trans. of the Royal Society A*, 366(1868):1297–1315, 2008.

[19] M. M. M. El Telbany and A. J. Reynolds. The structure of turbulent plane Couette flow. *Trans. ASME: J. of Fluids Engineering*, 104:367–372, 1982.

[20] H. Faisst and B. Eckhardt. Sensitive dependence on initial conditions in transition to turbulence in pipe flow. *J. Fluid Mech.*, 504:343–352, 2004.

[21] M. Fardad and B. Bamieh. Perturbation methods in stability and norm analysis of spatially periodic systems. *SIAM J. of Control and Optimization*, 47:997–1021, 2008.

[22] M. Fardad, M. R. Jovanović, and Bamieh B. Frequency analysis and norms of distributed spatially periodic systems. *IEEE Trans. on Automatic Control*, 53(10):2266–2279, 2008.

[23] B. F. Farrell. Optimal excitation of perturbations in viscous shear flow. *Phys. of Fluids*, 31(8):2093–2102, 1988.

[24] B. F. Farrell and P. J. Ioannou. Optimal excitation of three-dimensional perturbations in viscous constant shear flow. *Phys. of Fluids A*, 5(6):1390–1400, June 1993.

[25] B. F. Farrell and P. J. Ioannou. Stochastic forcing of the linearized Navier-Stokes equations. *Phys. of Fluids A*, 5(11):2600–2609, November 1993.

[26] B. F. Farrell and P. J. Ioannou. Variance maintained by stochastic forcing of non-normal dynamical systems associated with linearly stable shear flows. *Phys. Rev. Letters*, 72(8):1188–1191, February 1994.

[27] B. F. Farrell and P. J. Ioannou. Perturbation structure and spectra in turbulent channel flow. *Theoretical and Computational Fluid Dynamics*, 11:237–250, 1998.

[28] A. J. Favre, J. J. Gaviglio, and R. Dumas. Structure of velocity space-time correlations in a boundary layer. *Phys. of Fluids*, 10:S138–145, 1967.

[29] D. F. Gayme, B. McKeon, A. Papachristodoulou, B. Bamieh, and J. C. Doyle. Stream-wise constant model of turbulence in plane Couette flow. *Submitted to J. Fluid Mech.*

[30] D. F. Gayme, B. McKeon, A. Papachristodoulou, and J. C. Doyle. $2D/3C$ model of large scale structures in turbulence in plane Couette flow. In *Proceedings of the 6th Int'l Symposium on Turbulence and Shear Flow Phenomenon*, Seoul, Korea, 2009.

[31] J. F. Gibson, J. Halcrow, and P. Cvitanović. Equilibrium and travelling-wave solutions of plane Couette flow. *J. Fluid Mech.*, 638:243–266, 2009.

[32] M. Guala, S. E. Hommema, and R. J. Adrian. Large-scale and very-large-scale motions in turbulent pipe flow. *J. Fluid Mech.*, 554:521–542, 2006.

[33] L. H. Gustavsson. Energy growth of three-dimensional disturbances in plane Poiseuille flow. *J. Fluid Mech.*, 224:241–260, 1991.

[34] J. K. Hale and E. F. Infante. Extended dynamical systems and stability theory. *PNAS*, 58(2):405–409, 1967.

[35] J. M. Hamilton, J. Kim, and F. Waleffe. Regeneration mechanisms of near-wall turbulence structures. *J. Fluid Mech.*, 287:317–348, 1995.

[36] D. S. Henningson and S. C. Reddy. On the role of linear mechanisms in transition to turbulence. *Phys. of Fluids*, 6(3):1396–1398, 1994.

[37] D. Henry. *Geometric Theory of Semilinear Parabolic Equations.* Lecture Notes in Mathematics, Vol. 840, Springer-Verlag, New York, 1981.

[38] I. H. Herron. Observations on the role of vorticity in the stability of wall bounded flows. *Studies in Applied Mathematics*, 85(3):269–286, 1991.

[39] N. Hutchins and I. Marusic. Evidence of very long meandering structures in the logarithmic region of turbulent boundary layers. *J. Fluid Mech.*, 579:1–28, 2007.

[40] N. Hutchins and I. Marusic. Large-scale influences in near-wall turbulence. *Phil. Trans. Royal Society of London A*, 365:647–664, 2007.

[41] Y. Hwang and C. Cossu. Amplification of coherent streaks in the turbulent Couette flow: an input-output analysis at low Reynolds number. *J. Fluid Mech.*, 643:333–348, 2010.

[42] J. Jiménez and P. Moin. The minimal flow unit in near-wall turbulence. *J. Fluid Mech.*, 225:213–240, 1991.

[43] J. Jiménez and A. Pinelli. The autonomous cycle of near-wall turbulence. *J. Fluid Mech.*, 389:335–359, 1999.

[44] M. R. Jovanović and B. Bamieh. The spatio-temporal impulse response of the linearized Navier-Stokes equations. In *Proceedings of the* 2001 *American Control Conference*, pages 1948–1953, Arlington, VA, 2001.

[45] M. R. Jovanović and B. Bamieh. Unstable modes versus non-normal modes in supercritical channel flows. In *Proceedings of the* 2004 *American Control Conference*, pages 2245–2250, Boston, MA, 2004.

[46] M. R. Jovanović and B. Bamieh. Componentwise energy amplification in channel flows. *J. Fluid Mech.*, 534:145–183, 2005.

[47] J. Kim and J. Lim. A linear process in wall-bounded turbulent shear flows. *Phys. of Fluids Letters*, 12(8):1885–1888, 2000.

[48] K. J. Kim and R. J Adrian. Very large scale motion in the outer layer. *Phys. of Fluids*, 11(2):417–422, 1999.

[49] O. Kitoh, K Nakabyashi, and F. Nishimura. Study on mean velocity and turbulence characteristics of plane Couette flow: Low-Reynolds-number effects and large longitudinal vortical structure. *J. Fluid Mech.*, 539:199–227, 2005.

[50] O. Kitoh and M. Umeki. Experimental study on large-scale streak structure in the core region of turbulent plane Couette flow. *Phys. of Fluids*, 20(2):025107–025111, 2008.

[51] S. J. Kline, W. C. Reynolds, F. A. Schraub, and P. W. Runstadler. The structure of turbulent boundary layers. *J. Fluid Mech.*, 30:741–773, 1967.

[52] J. Komminaho, A. Lundbladh, and A. V. Johansson. Very large structures in plane turbulent Couette flow. *J. Fluid Mech.*, 320:259–285, 1996.

[53] L. S. G. Kovasznay, V. Kibens, and R. F. Blackwelder. Large-scale motion in the intermittent region of a turbulent boundary layer. *J. Fluid Mech.*, 41, part 2:283–325, 1970.

[54] R. Krechetnikov and J. E. Marsden. On the origin and nature of finite-amplitude instabilities in physical systems. *J. of Phys. A: Mathematical and Theoretical*, 42:412004, 2009.

[55] E. Kreyszig. *Introductory Functional Analysis with Applications*. John Wiley & Sons, New York, 1989.

[56] M. T. Landahl. A note on an algebraic instability of inviscid parallel shear flows. *J. Fluid Mech.*, 92(2):243–251, 1980.

[57] M. J. Lee and J. Kim. The structure of turbulence in a simulated plane Couette flow. *Thin Solid Films*, 1:531–536, 1991.

[58] J. L. Lumley. The structure of inhomogeneous turbulence. In A. M. Yaglom and V. I. Tatarski, editors, *Atmospheric Turbulence and Wave Propagation*, pages 166–178, Moscow, 1967. Nauka.

[59] W. Luo. *Wiener chaos expansion and numerical solutions of stochastic partial differential equations.* PhD thesis, California Institute of Technology, Pasadena, USA, 2006.

[60] Z. H. Luo, B. Z. Guo, and O. Morgul. *Stability and Stabilization of Infinite Dimensional Systems with Applications.* Springer-Verlag, London, 1999.

[61] R. Mathis, N. Hutchins, and I. Marusic. Large-scale amplitude modulation of the small-scale structures of turbulent boundary layers. *J. Fluid Mech.*, 628:311–337, 2009.

[62] B. J. McKeon and A. S. Sharma. A critical-layer framework for turbulent pipe flow. *J. Fluid Mech.*, 2010. to appear.

[63] J. Moehlis, H. Faisst, and B. Eckhardt. Periodic orbits and chaotic sets in a low-dimensional model for shear flows. *SIAM Journal on Applied Dynamical Systems*, 4:352–376, 2005.

[64] Y. Morinishi. Conservative properties of finite difference schemes for incompressible flow. In *Center for Turbulence Research Annual Research Briefs*, volume Spring, pages 121–132, 1995. http://www.stanford.edu/group/ctr/publications.html.

[65] J. F. Morrison, B. J. McKeon, W. Jiang, and A. J. Smits. Scaling of the streamwise velocity component in turbulent pipe flow. *J. Fluid Mech.*, 1508:99–131, 2004.

[66] M. Nagata. Three-dimensional finite-amplitude solutions in plane Couette flow: bifurcation from infinity. *J. Fluid Mech.*, 217:519–527, 1990.

[67] P. Orlandi and J. Jiménez. On the generation of turbulent wall friction. *Phys. of Fluids*, 16(2):634–641, 1994.

[68] S A. Orszag and A. T. Patera. Secondary instability of wall-bounded shear flows. *J. Fluid Mech.*, 128:347–385, 1983.

[69] A. Papachristodoulou. *Scalable Analysis of Nonlinear Systems Using Convex Optimization.* PhD thesis, California Institute of Technology, Pasadena, USA, 2005.

[70] V. C. Patel and R. Head. Some observations on skin friction and velocity profiles in fully developed pipe and channel flows. *J. Fluid Mech*, 38:181–201, 1969.

[71] G. Pujals, M. García-Villalba, C. Cossu, and S. Depardon. A note on optimal transient growth in turbulent channel flows. *Phys. of Fluids*, 21(1):015109:1–015109:6, 2009.

[72] S. C. Reddy and D. S. Henningson. Energy growth in viscous channel flows. *J. Fluid Mech.*, 252:209–238, 1993.

[73] S. C. Reddy, P. J. Schmid, and D. S. Henningson. Pseudospectra of the Orr-Sommerfeld operator. *SIAM J. of Applied Mathematics*, 53(1):15–47, 1993.

[74] S.C. Reddy and P.J. Ioannou. *Laminar-Turbulent Transition IUTAM 99*, chapter Energy Transfer Analysis of Turbulent Plane Couette Flow, pages 211–216. Springer-Verlag, Berlin, 2000.

[75] W. C. Reynolds and S. C. Kassinos. One-point modelling of rapidly deformed homogeneous turbulence. *Proceedings: Mathematical and Physical Sciences*, 451:87–104, Oct 1995.

[76] J. M. Robertson. On turbulent plane Couette flow. In *Proceedings of the 6th Midwestern Conference on Fluid Mech.*, pages 169–182, 1959.

[77] J. M. Robertson and H. F. Johnson. Turbulence structure in plane Couette flow. *J. Engineering Mech. Division*, 96:1171–1181, 1970.

[78] V. A. Romanov. Stability of plane-parallel Couette flow. *Funktsional'nyi Analiz i Ego Prilozhaniya*, 7(2):62–73, 1973. Translation by Moscow Physicotechnological Inst.

[79] P. J. Schmid and D. S. Henninson. *Stability and Transition in Shear Flows*. Applied Mathematical Sciences, Vol. 142, Springer-Verlag - New York, 2001.

[80] W. Schoppa and F. Hussain. Coherent structure generation in near-wall turbulence. *J. Fluid Mech.*, 453:57–108, 2002.

[81] G. B. Schubauer and H. Skramstad. Laminar boundary-layer oscillations and stability of laminar flow. *J. Aero. Sci.*, 14(2):69–78, 1947.

[82] T. R. Smith, J. Moehlis, and P. Holmes. Low-dimensional modelling of turbulence using the proper orthogonal decomposition: A tutorial. *Nonlinear Dynamics*, 41:275–307, 2005.

[83] J. Swanson. Variations of the solution to a stochastic heat equation. *Annals of Probability*, 35:2122–2159, 2007.

[84] R. Temam. *Infinite Dimensional Dynamical Systems in Mechanics and Physics*. Applied Mathematical Sciences, Vol. 68, Springer-Verlag, New York, 1997.

[85] N. Tillmark. *Experiments on transition and turbulence in plane Couette flow*. PhD thesis, Royal Institute of Technology, Stockholm, Sweden, 1995.

[86] N. Tillmark and P. H. Alfredsson. Experiments on transition in plane Couette flow. *J. Fluid Mech.*, 235:89–102, 1992.

[87] N. Tillmark and P. H. Alfredsson. *Advances in Turbulence VII*, chapter Large Scale Structure in Turbulent Plane Couette Flow, pages 59–62. Proceedings of the 7th European Turbulence Conf. Kluwer, Dordrecht, Saint-Jean Cap Ferrat, France, 1998.

[88] L. N. Trefethen. Pseudospectra of linear operators. *SIAM Review*, 39(3):383–406, 1997.

[89] L. N. Trefethen and M. Embree. *Spectra and Pseudospectra, The Behavior of Nonnormal Matrices and Operators*. Princeton University Press, Princeton, NJ, 2005.

[90] L. N. Trefethen, A. E. Trefethen, S. C. Reddy, and T. A. Driscoll. Hydrodynamic stability without eigenvalues. *Science*, 261(5121):578–584, 1993.

[91] T. Tsukahara, H. Kawamura, and K. Shingai. DNS of turbulent Couette flow with emphasis on the large-scale structure in the core region. *J. Turbulence*, 7(019), 2006.

[92] S. Tullis and A. Pollard. Modeling the time-dependent flow over riblets in the viscous wall region. *Applied Scientific Research*, 50(3-4):299–314, 1993.

[93] F. Waleffe. Proposal for a self-sustaining mechanism in shear flows. Center for Turbulence Research, Stanford University/NASA Ames, Spring 1990. Unpublished.

[94] F. Waleffe. Hydrodynamic stability and turbulence: Beyond transients for a self-sustaining process. *Studies in Applied Mathematics*, 95:319–343, 1995.

[95] F. Waleffe. On a self-sustaining process in shear flows. *Phys. of Fluids*, 9(4):883–900, 1997.

[96] F. Waleffe. Three-dimensional coherent states in plane shear flows. *Phys. Rev. Letters*, 81(19):4140–4143, 1998.

[97] F. Waleffe, J. Kim, and J. Hamilton. On the origin of streaks in turbulent shear flows. In *Eighth Int'l Symposium on Turbulent Shear Flows*, Munich, Germany, Sept. 1991.

[98] J. A. C. Weideman and S. C. Reddy. A MATLAB differentiation matrix suite. *ACM Trans. on Mathematical Software*, 26(4):465–519, 2000.

[99] K. Zhou, J. C. Doyle, and K. Glover. *Robust and Optimal Control*. Prentice Hall, Upper Saddle River, NJ, 1996.